



The Influence of mesostructure on the microstructure and mechanical properties of Selective Laser Melted *Ti-6Al-4V* alloy lattices

*A thesis presented for the degree of Doctor of Philosophy
by*

Hazzaa Fayez Al-Qurashi

Supervisors:
Prof. Russell Goodall
Dr. Julian Dean

Department of Materials Science and Engineering
Faculty of Engineering

January 2023

Dedication

*To my late father,
who unfortunately passed away when I was kid, and
he did not see his little boy in what he aspires to.*

Abstract

Selective Laser Melting (SLM), an Additive Manufacturing (AM) process, has been used to manufacture Ti-6Al-4V lattice structures to investigate the influence of mesostructure on the microstructure and the mechanical properties. Different lattice structures with different features such as thin sections, curvature, and build angle were examined. The study results revealed that, while much of the material consists of columnar grains with similar alignment, there is an area near to the inner surface with anisotropic orientation. These results led to a further investigation into the connection between the lattice crystallography and the mechanical properties by designing lattice structure capturing this phenomenon. This study confirmed that the build orientation and post treatment have an effect on the elastic behaviour of the structure, though in the example tested here the strength is not affected to a significant extent. Numerical modelling was used to assess the impact of microstructural inhomogeneity on mechanical properties, and this goal has been achieved by changing the material orientations, which led to changes in the lattice stiffness.

Acknowledgments

“In the name of Allah, the Most Gracious and the Most Merciful”

All praises to Allah for His blessing to complete my thesis.

Firstly, I express my humble thanks to God. I would like to express my profound thankfulness to my supervisor, **Professor Russell Goodall** for his support, patience, and caring. I would have not been able to complete this journey without his support during the difficult times and his experience, thorough insight and scientific thinking. It has been a great honour for me to work under his supervision.

I would also like to convey my deep gratitude to my second supervisor **Dr. Julian Dean** for his academic suggestions throughout the PhD. The great deal of support, direction and insightful advice he offered to my study and experimentation were vital in the completion of this work. I was very blessed to have the opportunity to work with many brilliant individuals throughout this Journey.

Most of all, I would like to show my appreciation to the people who shared the happiness and the sadness with me in this tough years Fahad Alshammari, Meshari Alotaibi, and Fawaz Almutairi. My friends who are making my time enjoyable.

My lovely mother, Badriyah, My dear brothers, Ahmed and Emad. I would never have here without your prayer and encouragement. I owe everything I have and everything I have become to you.

أمي الغالية بدريه، إخوتي الأعزاء أحمد وعماد، لولا الله ثم دعواتكم الصادقة ودعمكم لم أصل إلى هنا. أدين لكم بكل شيء أصبحت أو سأصبح عليه .

Last but not the least, this journey would not have been possible without the support, encouragement, and the love of my wife, **Alaa**, my boy, **Ahmed**, the new bundle of joy **Naif** who are the source of happiness and smiles. I could not complete my PhD without your patience and support. Thanks for standing beside me through everything.

I would like to thank the Saudi Government, Umm AlQura University, the Royal Embassy, Saudi Cultural Bureau and Ministry of Education to give me this opportunity to complete my higher education.

**Thanks be to Allah Almighty
Hazaa Alqurashi**

Contents

Chapter 1 : Introduction	1
Chapter 2 : Literature Review	4
2.1. Titanium and its alloys	4
2.1.1. $\alpha + \beta$ alloys	6
2.1.2. Ti-6Al-4V	8
2.2. Additive Manufacturing (AM)	11
2.2.1. Additive Manufacturing Processes	12
2.2.2. Selective Laser Melting (SLM)	16
2.3. Lattices	25
2.3.1. The Geometry	28
2.4. Simulation Techniques	33
2.4.1. Finite Element Method (FEM)	36
2.4.2. Cellular Automata (CA)	38
2.4.3. CA-FE	39
Chapter 3 : Experimental Procedures	41
3.1. Specification of AM Samples	41
3.2. Renishaw Building	44
3.3. Aconity Building	44
3.4. Micropreparation	45
3.5. Post Processing (Heat Treatment)	45
3.6. Measurements	45
3.6.1. Optical Microscopy	45
3.6.2. Electron Backscatter Diffraction (EBSD)	46
3.6.3. Surface Roughness	46

3.7. Compression Test	46
3.8. Finite Elements Method (FEM)	47
3.8.1. Setup Boundary Conditions and Validation	48
Chapter 4 : The Effect of Component Shape on AM Ti6Al4V Microstructure	51
4.1. The Effect of Build Geometry on AM Ti6Al4V Microstructure	51
4.1.1. The cylindrical Hole Samples (Shape-C1)	52
4.1.2. Elliptic Cylindrical Hole Samples (Shape-E1 and Shape-E2)	55
4.2. The Effect of Build Angle on AM Ti6Al4V Microstructure	65
4.3. The Textures of different AM Ti6Al4V Samples	71
4.3.1. The Effect of Curvature (Cylinder, Elliptical Cylinder)	71
4.3.2. The Effect of Build Angle on the Texture	75
4.4. Chapter Summary	77
Chapter 5 : Effect of Degree of Microstructural Order on Elastic Behaviour in Ti-6Al-4V	80
5.1. Setup Boundary Conditions and Validation	80
5.2. Comparing between α and β as Ti6Al4V Phases	82
5.3. Simulation of Ti6Al4V with α and β Phases together	86
5.4. Simulation of Block with Cylindrical Hole (Shape-C1)	92
5.5. Chapter Summary	98
Chapter 6 : Mechanical Properties of Lattices	99
6.1. Structure Definition	99
6.2. Compression Tests Results	101
6.2.1. Compressive Response	101
6.2.2. Elastic Properties	107
6.3. Discussion	109
6.4. Chapter Summary	112

Chapter 7 : Conclusions and Future Work	114
7.1. Conclusions	114
7.1.1. The effect of component shape on the microstructure	114
7.1.2. The mechanical properties of lattices	115
7.1.3. The effect of degree of microstructural order on the elastic behaviour.	115
7.2. Future Work	116
REFERENCES	117

List of Figures

Figure 1.1 A diagram shows of the project objectives.	2
Figure 2.1 Unit cells of a hexagonal closed packed (hcp) structure with α phase (left), and a body centred cubic (bcc) structure with β phase [1].	5
Figure 2.2 A 3D Phase diagram of Ti alloys with α and β phases and their common stabilisers [1].	6
Figure 2.3 Transforming microstructures of $\alpha + \beta$ alloy with different cooling rate [9]. a) Cooled to room temperature in a furnace (slow cooling), b) Water quenched (fast cooling).	8
Figure 2.4 The main microstructures of Ti-6Al-4V, a) lamellar (top), b) equiaxed (middle), and c) bimodal (bottom) [12].	9
Figure 2.5 An image illustrating basic AM design or a component (layer by layer) [28].	13
<i>Figure 2.6 A diagram showing the NIST artefact to test machine capability and accuracy [30]</i>	14
Figure 2.7 A schematic description of a selective laser melting process [34].	16
Figure 2.8 A schematic of thermal stresses formation between powder layers during SLM [36].	18
Figure 2.9 A SEM image showing the balling formation with different scanning speeds [42].	18
Figure 2.10 The Staircase effects in AM parts [46].	20
Figure 2.11 The two microstructures of Ti-6Al-4V via SLM, a) α' martensite, and b) $\alpha + \beta$ phases [57].	22
Figure 2.12 Optical micrographs (OM) of Ti-6Al-4V produced by SLM (left) and EBM (right) [60].	23
Figure 2.13 Bar graph of mechanical properties of Ti-6Al-4V produced by AM. Data from	24
Figure 2.14 A Stress- Strain curve comparing between single meta-grain and eight meta grains of architected structures [63].	24
Figure 2.15 A flow chart shows the factors that have influence the properties of lattice [64].	25
Figure 2.16 The two deformation mechanisms in cellular materials, a) Bending, b) Stretching [64].	26
Figure 2.17 The stress-strain curves of cellular materials where the microstructures are dominated by bending deformation (left) and stretching deformation (right) [64].	26
Figure 2.18 The different lattices fabricated by SLM (left), the sample during bend test (right) [76].	28
Figure 2.19 The comparison between the different lattices and the solid [76].	29
Figure 2.20 The mechanical properties of Ti-6Al-4V lattices that made by SLM and SEBM [75].	30
Figure 2.21 A unit cell of rhombic dodecahedron structure with different relative densities [72].	31
Figure 2.22 A comparison between simulation and experiment of four different samples [73].	31
Figure 2.23 A model of iBCC lattice for finite element method [77].	32

Figure 2.24 A set of designed lattices [77].	32
Figure 2.25 Multiscale modelling techniques scale representation [81].	33
Figure 2.26 A finite elements representation [114].	37
Figure 2.27 Moore and von Neumann neighbourhoods.	38
Figure 2.28 A schematic representation of a couple between CA and FE grids [98].	40
Figure 3.1 A front view of different sizes of square holes within a cube.	42
Figure 3.2 A front view of a cylinder and elliptical holes within a cube.	42
Figure 3.3 A front view of different sizes of cuboid holes within a cube with 45° angle.	42
Figure 3.4 A front view of different cuboid holes within a cube with 20° angle.	42
Figure 3.5 A finite element model of a solid cube unit cell showing the boundary conditions that are applied on the cube.	49
Figure 3.6 The von Mises stress results of the cube unit cell under compression to a strain of -1.5×10^{-3} , the blue colour represents the even stress inside the cube.	50
Figure 4.1 An SEM EBSD micrograph showing part of an as built AM Ti6Al4V component created to explore the variation in microstructure with component geometry, consisting of a cube with a cylindrical hole, with the image taken from the area indicated.	53
Figure 4.2 An SEM EBSD micrograph showing part of an as built AM Ti6Al4V component created to explore the variation in microstructure with component geometry, consisting of a cube with a cylindrical hole, with the image taken from the area indicated.	54
Figure 4.3 An SEM EBSD micrograph showing part of an as built AM Ti6Al4V component created to explore the variation in microstructure with component geometry, consisting of a cube with a cylindrical hole, with the image taken from the area indicated.	54
Figure 4.4 An optical micrograph showing part of an as built AM Ti6Al4V component created to explore the variation in microstructure with component geometry, consisting of a cube with a cylindrical hole.	55
Figure 4.5 An SEM EBSD micrograph showing part of an as built AM Ti6Al4V component created to explore the variation in microstructure with component geometry, consisting of a cube with an elliptical cylindrical hole, with the image taken from the area indicated.	57
Figure 4.6 An SEM EBSD micrograph showing part of an as built AM Ti6Al4V component created to explore the variation in microstructure with component geometry, consisting of a cube with an elliptical cylindrical hole, with the image taken from the area indicated.	58
Figure 4.7 An SEM EBSD micrograph showing part of an as built AM Ti6Al4V component created to explore the variation in microstructure with component geometry, consisting of a cube with an elliptical cylindrical hole, with the image taken from the area indicated.	59
Figure 4.8 An optical micrograph showing part of an as built AM Ti6Al4V component created to explore the variation in microstructure with component geometry, consisting of a cube with an elliptical cylindrical hole.	59

Figure 4.9 An SEM EBSD micrograph showing part of an as built AM Ti6Al4V component created to explore the variation in microstructure with component geometry, consisting of a cube with an elliptical cylindrical hole, with the image taken from the area indicated.	61
Figure 4.10 An SEM EBSD micrograph showing part of an as built AM Ti6Al4V component created to explore the variation in microstructure with component geometry, consisting of a cube with an elliptical cylindrical hole, with the image taken from the area indicated.	62
Figure 4.11 An SEM EBSD micrograph showing part of an as built AM Ti6Al4V component created to explore the variation in microstructure with component geometry, consisting of a cube with an elliptical cylindrical hole, with the image taken from the area indicated.	63
Figure 4.12 An SEM EBSD micrograph showing part of an as built AM Ti6Al4V component created to explore the variation in microstructure with component geometry, consisting of a cube with an elliptical cylindrical hole, with the image taken from the area indicated.	64
Figure 4.13 An SEM EBSD micrograph showing part of an as built AM Ti6Al4V component created to explore the variation in microstructure with component geometry, consisting of a cube with a square hole, with the image taken from the area indicated.	66
Figure 4.14 An SEM EBSD micrograph showing part of an as built AM Ti6Al4V component created to explore the variation in microstructure with component geometry, consisting of a cube with a square hole, with the image taken from the area indicated.	67
Figure 4.15 An SEM EBSD micrograph showing part of an as built AM Ti6Al4V component created to explore the variation in microstructure with component geometry, consisting of a cube with a square hole, with the image taken from the area indicated.	68
Figure 4.16 An SEM EBSD micrograph showing part of an as built AM Ti6Al4V component created to explore the variation in microstructure with component geometry, consisting of a cube with a square hole, with the image taken from the area indicated.	68
Figure 4.17 An SEM EBSD micrograph showing part of an as built AM Ti6Al4V component created to explore the variation in microstructure with component geometry, consisting of a cube with a square hole, with the image taken from the area indicated.	69
Figure 4.18 An SEM EBSD micrograph showing part of an as built AM Ti6Al4V component created to explore the variation in microstructure with component geometry, consisting of a cube with a square hole, with the image taken from the area indicated.	70
Figure 4.19 An SEM EBSD micrograph showing part of an as built AM Ti6Al4V component created to explore the variation in microstructure with component geometry, consisting of a cube with a square hole, with the image taken from the area indicated.	70
Figure 4.20 Pole figures depicting reconstructed β textures measured by EBSD; a) from the left inner edge of the cylindrical hole, and b) from the upper inner edge of the cylindrical hole.	72
Figure 4.21 Pole figures depicting α -phase textures measured by EBSD; a) from the left inner edge of the cylindrical, and b) from the upper inner edge of the cylindrical.	73
Figure 4.22 Pole figures depicting reconstructed β textures measured by EBSD; a) from the upper inner edge of the horizontal elliptical cylindrical, and b) from the left inner edge of the horizontal elliptical cylindrical.	74
Figure 4.23 Pole figures depicting α -phase textures measured by EBSD; a) from the upper inner edge of the horizontal elliptical cylindrical, and b) from the left inner edge of the horizontal elliptical cylindrical.	74

Figure 4.24 Pole figures depicting textures measured by EBSD from the bottom inner edge of the vertical elliptical cylindrical: a) β -phase, and b) α -phase.	75
Figure 4.25 Pole figures depicting textures measured by EBSD from the middle inner edge of the cubic hole: a) β -phase, and b) α -phase.	76
Figure 4.26 A sketch showing different areas in a sample with different features that using to illustrate the summary of the results.	79
Figure 5.1 A finite element model of a solid cube unit cell showing the boundary conditions that are applied on the cube.	81
Figure 5.2 The von Mises stress results of the cube unit cell under compression to a strain of -1.5×10^{-3} , the blue colour represents the even stress inside the cube.	82
Figure 5.3 A diagram illustrates the model structure and different coordinate systems. a) The black cube represents the model that using in FEM, the blue cube represents the material of the model. b) A diagram shows the coordinate system X,Y,Z as Pitch, Yaw, Roll their angles θ, ψ, ϕ .	83
Figure 5.4 Four images of the coordinates system that used in ANSYS showing different rotations. a) Global coordinates system without rotation. b) Global coordinates system with rotation around Yaw (green). a) Global coordinates system with rotation around Pitch (red). a) Global coordinates system with rotation around Roll (blue).	83
Figure 5.5 showed three different relationships of the structure's stiffness (E) of Ti6Al4V α , with angle of different axes, the orange line represents E while the crystal structure of the material is rotated around roll axis. the blue line represents E while the crystal structure of the material is rotated around pitch axis. the grey line represents E while the crystal structure of the material is rotated around yaw axis.	85
Figure 5.6 showed three different relationships of the structure's stiffness (E) of Ti6Al4V β , with angle of different axes, the orange line represents E while the crystal structure of the material is rotated around roll axis. the grey line represents E while the crystal structure of the material is rotated around yaw axis.	86
Figure 5.7 A finite element model of 64 cubes ($4 \times 4 \times 4$) and each cube will represent a single grain.	88
Figure 5.8 Illustrates the relationship between Young's Modulus (E) and α phase concentration in α and β structure. The yellow line represents the columnar structure (axial loading), the blue line represents the row-by-row structure (transverse loading).	88
Figure 5.9 Two ANSYS models of Ti6Al4V α (blue) and β (red) phases together, a) columnar structure, b) row-by-row structure.	89
Figure 5.10 2D diagrams of solid cubes with cylinder hole, a) sketch with dimensions of the real sample produced by SLM, b and c) sketches with dimensions of FEM models showing the sleeve inside the cylinder hole (green circle).	93
Figure 5.11 showed the results of stiffness (E) of Ti6Al4V for the two different cubes while the cylindrical rotates around Pitch axis. The blue line represents E of the structure of $r = 4.25\text{mm}$ cylindrical hole, the grey line represents E of the structure of $r = 4\text{mm}$ cylindrical hole.	96
Figure 5.12 showed the results of stiffness (E) of Ti6Al4V for the two different cubes while the cylindrical rotates around Roll axis. The orange line represents E of the structure of $r = 4.25\text{mm}$ cylindrical hole, the yellow line represents E of the structure of $r = 4\text{mm}$ cylindrical hole.	96

Figure 5.13 A front view of the model shows the stress areas in the structure. The colours indicates the levels of the stresses.	97
Figure 5.14 The stiffness behaviour comparison of Ti-6Al-4V of solid cube (above) and the cubes with a cylindrical hole (below) with rotation around the pitch axis.	97
Figure 1.3 A conventional diamond lattice structure [126].	100
Figure 1.4 shows two different orientations of the stretched diamond lattices, vertical (left) and horizontal (right).	101
Figure 1.5 Illustrates stress/strain curve, showing ultimate compression strength (UCS) and 0.2% yield strength ($\sigma_{0.2}$) of the as-built vertical (AB-VER) sample no.1.	103
Figure 1.6 Illustrates stress/strain curve, showing ultimate compression strength (UCS) and 0.2% yield strength ($\sigma_{0.2}$) of the as-built horizontal (AB-HOR) sample no.1.	103
Figure 1.7 Illustrates stress/strain curve, showing ultimate compression strength (UCS) and 0.2% yield strength ($\sigma_{0.2}$) of the heat-treated vertical (HT-VER) sample no.5.	104
Figure 1.8 illustrates stress/strain curve, showing ultimate compression strength (UCS) and 0.2% yield strength ($\sigma_{0.2}$) of the heat-treated horizontal (HT-HOR) sample no.5.	104
Figure 1.9 Illustrates average of ultimate compression strength (UCS) and 0.2% yield strength ($\sigma_{0.2}$) of the as-built horizontal (AB-HOR), heat-treated horizontal (HT-HOR), as-built vertical (AB-VER) and heat-treated vertical (HT-VER).	105
Figure 1.10 Comparison of reported data in Table 1.1 with predictions of the Gibson-Ashby model.	106
Figure 1.11 Illustrates average of Elastic modulus (E) of the as-built horizontal (AB-HOR), heat-treated horizontal (HT-HOR), as-built vertical (AB-VER) and heat-treated vertical (HT-VER).	107
Figure 1.12 Comparison of reported data in Table 1.2 with predictions of the Gibson-Ashby model.	109
Figure 1.1 Two different orientations of the helix structure design, vertical (left) and horizontal (right).	110
Figure 1.2 A failed sample of the vertical helix design.	110
Figure 1.13 A picture of one the heat-treated samples show the oxidation (black on the right)	112

List of Tables

Table 2.1 The composition and transus temperature (T_{β}) of a number of $\alpha + \beta$ alloys [4].	7
Table 2.2 ASTM classification of AM processes [27, 31].	15
Table 2.3 Comparison of reported mechanical properties of Ti-6Al-4V via SLM and EBM.	23
Table 3.1 A summary of the specification and pictures of the samples	43
Table 3.2 The chemical composition (wt%) of Ti-6Al-4V powder provided by the manufacturer.	44
Table 3.3 The properties values of Ti-6Al-4V alloy that used in ANSYS [5].	48
Table 3.4 Stiffness coefficient of α and β phases of Ti-6Al-4V (GPa) [117, 118].	48
Table 5.1 The stresses results of axial loading and transverse loading on different strains to determine the elastic modulus E	90
Table 5.2 A comparison between FEM results and Theory calculations of Axial and Transverse loading.	91
Table 1.1 Comparison of the Yield Strength ($\sigma_{0.2}$) of Ti6Al4V lattices manufactured by AM processes.	106
Table 1.2 Comparison of the elastic modulus of Ti6Al4V lattices manufactured by AM processes.	108

Chapter 1 : Introduction

Additive Manufacturing (AM) has become one of the most important production technologies in the world. The approach is based on simplifying the complexity of 3D shapes to the machine during the production process by dividing the shape to a great number of layers positioned sequentially above each other. This revolutionary methodology opens the door to for scientists and engineers to explore new areas in most fields.

Additive manufacturing techniques such as Selective Laser Melting (SLM) are of great interest in efficient manufacture of metallic parts, and are highly suitable for materials such as lattices with interesting mechanical properties. Selective Laser Melting (SLM) is becoming one of the most useful techniques due the fine microstructure of the final product and this has direct impact on the improvement of the mechanical properties of the metallic parts.

However, the microstructure of the material produced is highly dependent on the structure complexity (especially for materials like Ti6Al4V), and cooling conditions are highly anisotropic and variable in SLM, also made more complex by the heat path through a lattice. Understanding the link between the microstructure formation and the mechanical properties, means that such materials can be processed with confidence, and even may permit the design of new structures to optimise performance or achieve particular behaviour, making use of the effect.

The project is aiming to investigate the effect of the mesostructures on the microstructure of lattices structures from Ti-6Al-4V fabricated by SLM, and the effect of both of these on the mechanical properties, and use Finite Element Modelling (FEM) to understand the roles of different features of the microstructure. In order to achieve this aim, the project has these objectives:

- Study the effect of different mesostructural characteristics (individually and together) on the microstructure of SLM processed Ti-6Al-4V, in shapes of relevance to lattices (e.g. overhangs, thin sections, changing angles and sections, etc.).
- Develop a simulation capability to assess the impact of the microstructural inhomogeneity on mechanical properties.
- Validation of this simulation capability for lattice-scale mechanical properties.
- Design of different lattice structures to achieve mechanically desirable microstructure distribution.

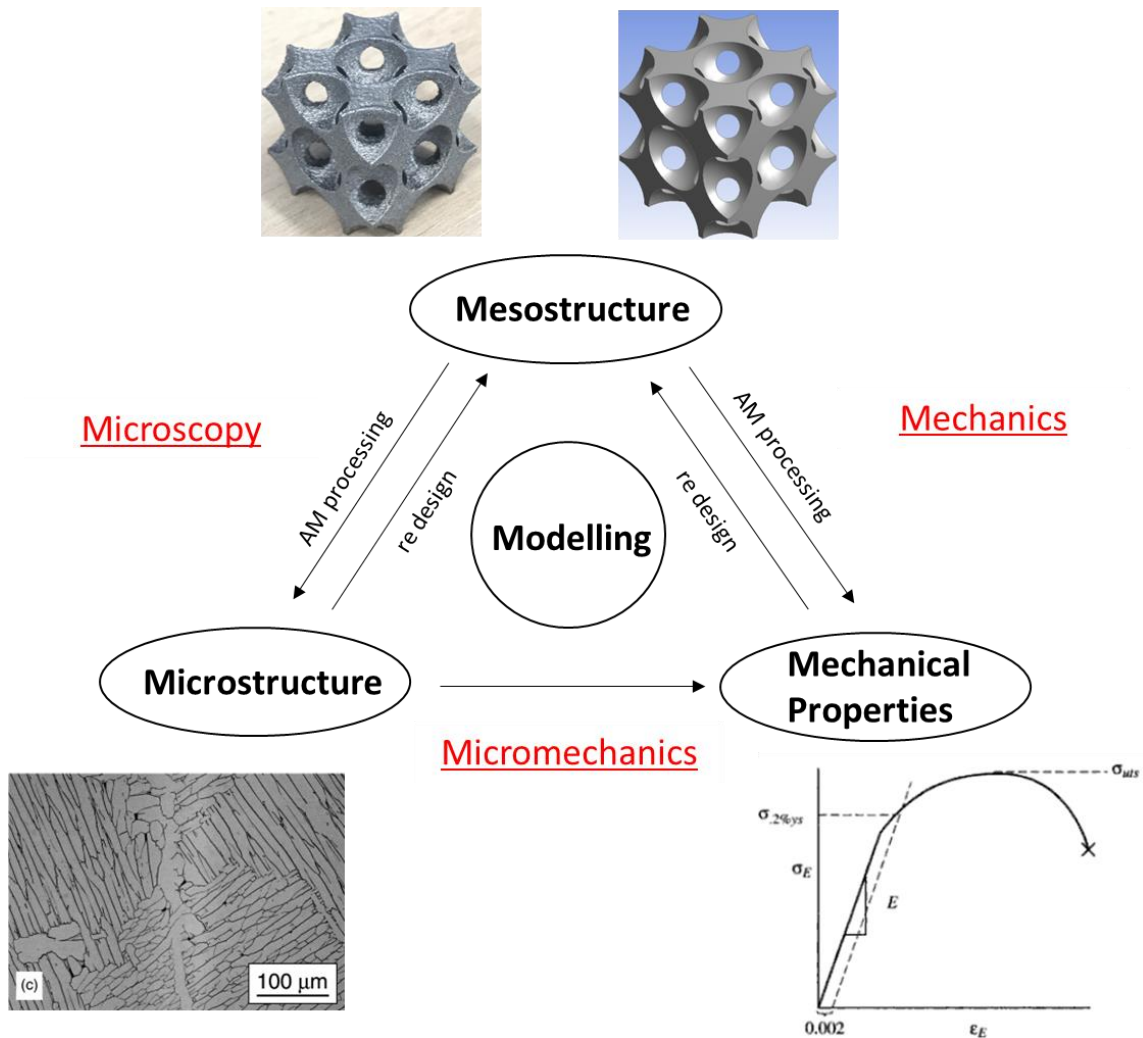


Figure 1.1 A diagram shows of the project objectives.

The thesis chapters are presented in the following order:

- Chapter 1** An introduction to the thesis aim and outline.
- Chapter 2** Literature review surrounding this work starting with exploring the titanium and its alloys with focus on Ti6Al4V and its microstructure and the mechanical properties. Then Additive Manufacturing (AM) techniques are discussed with particular emphasis on Selective Laser Melting (SLM). Finally, the microstructure and the mechanical properties of lattice structures are reviewed.
- Chapter 3** Presents the experimental procedures that have been used in this project, with detailed each technique, and illustrating the numerical methods.
- Chapter 4** The effect of build geometry with different features on SLM Ti6Al4V as-built microstructure is investigated. Then, the effect of build angle on SLM Ti6Al4V as-built microstructure is studied. Finally, the crystallographic textures of these factors (build geometry and build angle) are explored.
- Chapter 5** The capabilities of Finite Element Model (FEM) have been used to simplify to the basic in terms of structure or material. Then, the models are developed simulate the real structures to investigate the effect of microstructure of this mesostructure on the mechanical properties.
- Chapter 6** The mechanical properties of designed lattices and the result of the compressive response is presented. Following this, investigation of the effect of build orientation and post processing applied to a stretched diamond lattice, through mechanical properties acquired from compression testing. After this, the stiffness of the stretched diamond lattices developed and made here is used as the comparison factor between different build orientations.
- Chapter 7** Concludes the key findings of this work and suggests future work.

Chapter 2 : Literature Review

In this chapter, a general review of titanium and its alloys and their properties is provided, then a close look into Ti-6Al-4V and its properties and applications are given. The different processes of Additive Manufacturing (AM) are considered, with focus on the Selective Laser Melting (SLM) process, which is used in this thesis, especially the microstructure and the mechanical properties of products that made by SLM. Finally, the lattice designs that are fabricated by AM processes are studied, with a specific attention on using simulation as a tool to compare to experiment results.

2.1. Titanium and its alloys

Titanium is element number 22 in the periodic table, and it was discovered by William Gregor in 1791 [1, 2]. Titanium and its alloys are used in a great number of industries such as aerospace, medical, architecture, and automotive [1]. At present, the aerospace industry is considered as the biggest consumer market for titanium alloys due to the high strength to weight ratio; this property makes titanium an excellent substitute for steel and aluminium [2]. The resistance to corrosion and biocompatibility of titanium alloys also allow it to be useful as a biomaterial [3], and in addition, titanium alloys have good mechanical properties such as the creep resistance and fatigue [1]. Titanium is described as an allotropic metal with melting temperature at 1670 °C, which can transform between two crystal structures: 1) at ambient temperature, the structure is a hexagonal closed packed (hcp) phase alpha (α), 2) at high temperature, the structure is a body centred cubic (bcc) phase beta (β) as shown in Figure 2.1 [1]. The structural transformation occurs at high temperature (882 ± 5 °C) which is termed the β transus temperature (T_{β}) [4].

Titanium alloys can be categorised depending on the varying amounts of the added elements, and the phases that result at room temperature due these additions. These alloys mainly are alpha (α) alloys, beta (β) alloys, and alpha - beta ($\alpha+\beta$) alloys, while other alloys are further classified as “near alpha” alloys and “near beta” alloys [4]. The alloying elements

can affect the β transus temperature (T_β) are divided to three groups: 1) α phase stabiliser elements such as aluminium, oxygen, carbon and nitrogen that increase β transus temperature (T_β) and also strengthen the α phase [5], 2) β phase stabiliser elements such as vanadium, tantalum, iron and manganese that decrease β transus temperature (T_β), which generally leads to an increase in the strength to weight ratio of the alloy [4], 3) elements which have a minor or no influence and are called phase neutral elements such as zinc and tin, as shown in Figure 2.2 [1, 4].

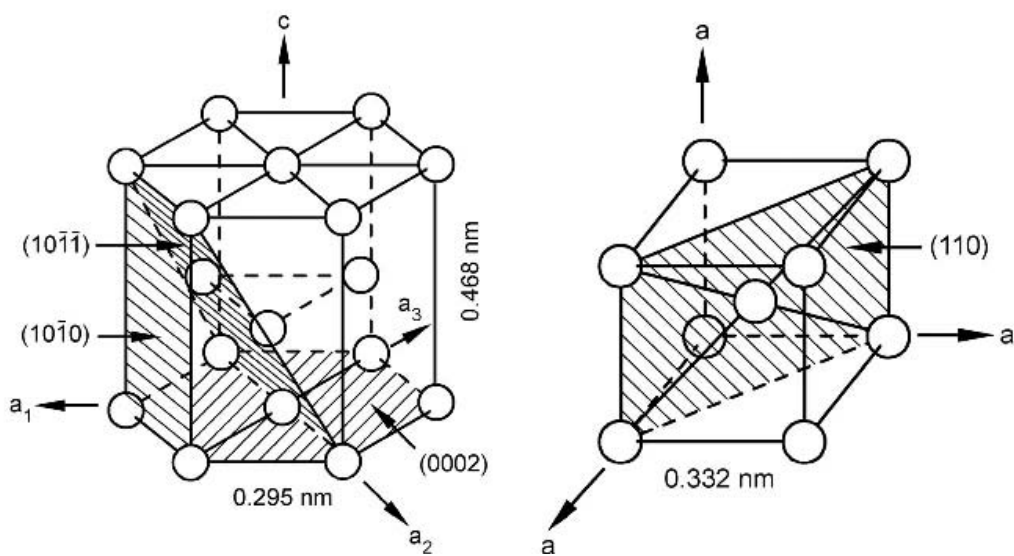


Figure 2.1 Unit cells of a hexagonal closed packed (hcp) structure with α phase (left), and a body centred cubic (bcc) structure with β phase [1].

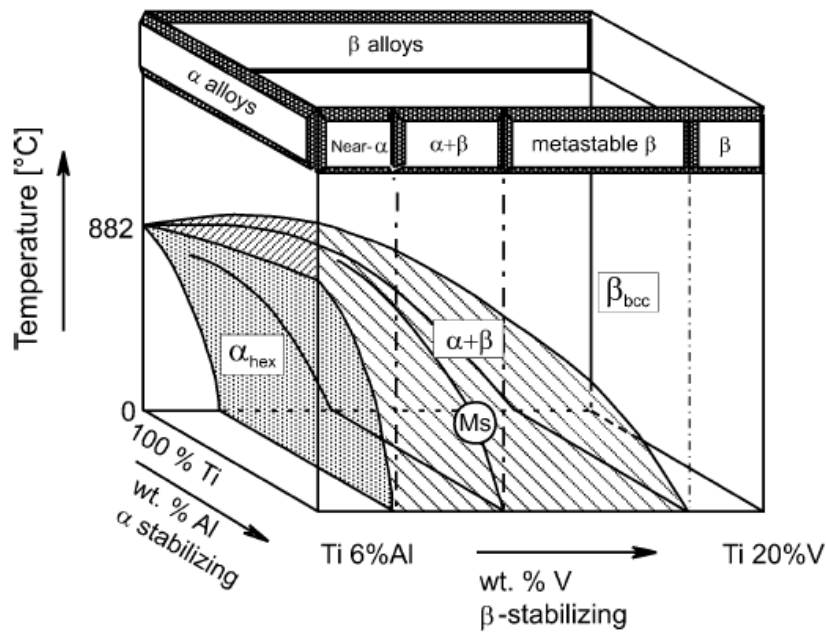


Figure 2.2 A 3D Phase diagram of Ti alloys with α and β phases and their common stabilisers [1].

2.1.1. $\alpha + \beta$ alloys

$\alpha + \beta$ alloys are produced when there is sufficient quantity of stabilising elements for β phase [6]. The addition of the stabilisers, which is usually from 4 to 6 wt%, allows β phase to be retained on cooling [6]. These alloys have excellent properties such as corrosion resistance, fatigue strength, high tensile strength, and high elastic modulus, and these properties have led these alloys to be used mainly in aircraft parts [4, 6]. In addition, ageing treatments and heat treatments can improve the properties of these alloys. The alloy composition and the cooling rate can influence the transformation between β and α phases in titanium alloys which can lead to controlled diffusion to form a hexagonal martensite phase (α') and an orthorhombic martensite phase (α''). Table 2.1 shows different compositions of $\alpha + \beta$ alloys and their transus temperature (T_β) [7] [8].

Table 2.1 The composition and transus temperature (T_{β}) of a number of $\alpha + \beta$ alloys [4].

$\alpha + \beta$ alloys	Alloy composition	T_{β} (°C)
Ti-11	Ti-6Al-2Sn-1.5Zr-1Mo-0.35Bi-0.1Si	1015
Ti-8-1-1	Ti-8Al-1V-1Mo	1040
IMI 679	Ti-2.5Al-11Sn-5Zr-1Mo-0.2Si	945
IMI 550	Ti-4Al-2Sn-4Mo-0.5Si	975
IMI 685	Ti-6Al-5Zr-0.5Mo-0.25Si	1020
IMI 829	Ti-5.5Al-3.5Sn-3Zr-1Nb-0.25Mo-0.3Si	1015
IMI 834	Ti-5.5Al-3.5Sn-3Zr-1Nb-0.25Mo-0.3Si-0.06C	1045
Ti-6-4	Ti-6Al-4V	995
Ti-6-6-2	Ti-6Al-6V-2Sn	945
Ti-17	Ti-5Al-2Sn-4Mo-4Cr	890

There are factors which could affect the $\alpha + \beta$ alloy microstructure such as the thermomechanical processes and treatments which are applied. In the slow cooling transformation, a continuous layer of α phase is nucleated along the grain boundary of β . Furthermore, the growth of α colonies is continuous and parallel with the β grain boundaries, which are retained to be a half β phase and coexist with α phase, as shown in Figure 2.3a [7]. On the other hand, when the cooling rate is increased, the colonies of laths of α phase become smaller and partially perpendicular to each other (basket weave), as shown in Figure 2.3b, which could reduce the residual elastic strains [9].

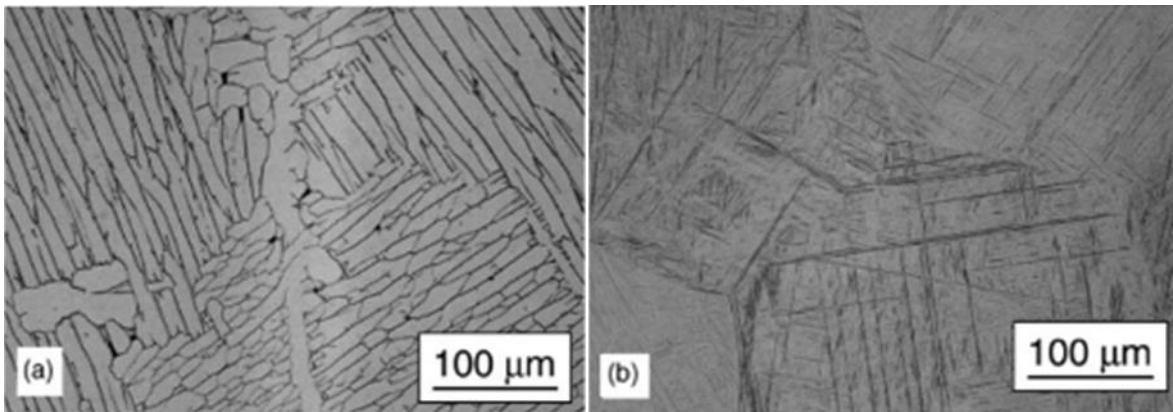


Figure 2.3 Transforming microstructures of $\alpha + \beta$ alloy with different cooling rate [9]. a) Cooled to room temperature in a furnace (slow cooling), b) Water quenched (fast cooling).

2.1.2. Ti-6Al-4V

Ti-6Al-4V is one of the best-known and most widely used titanium alloys. This alloy is an $\alpha + \beta$ alloy that uses aluminium as a stabiliser for α phase with an addition between 5.5 – 6.75 wt% and vanadium as a stabiliser for the β phase with addition between 3.5 – 4.5 wt% [9]. The addition of the stabilisers gives this alloy excellent properties such as high strength, high temperature capability, corrosion resistance, and biocompatibility [10, 11]. The interstitial elements and the cooling transformation have a key role to form different configurations of microstructure of Ti-6Al-4V, which are a) lamellar, b) equiaxed, and c) bimodal, as shown in Figure 2.4 [12].

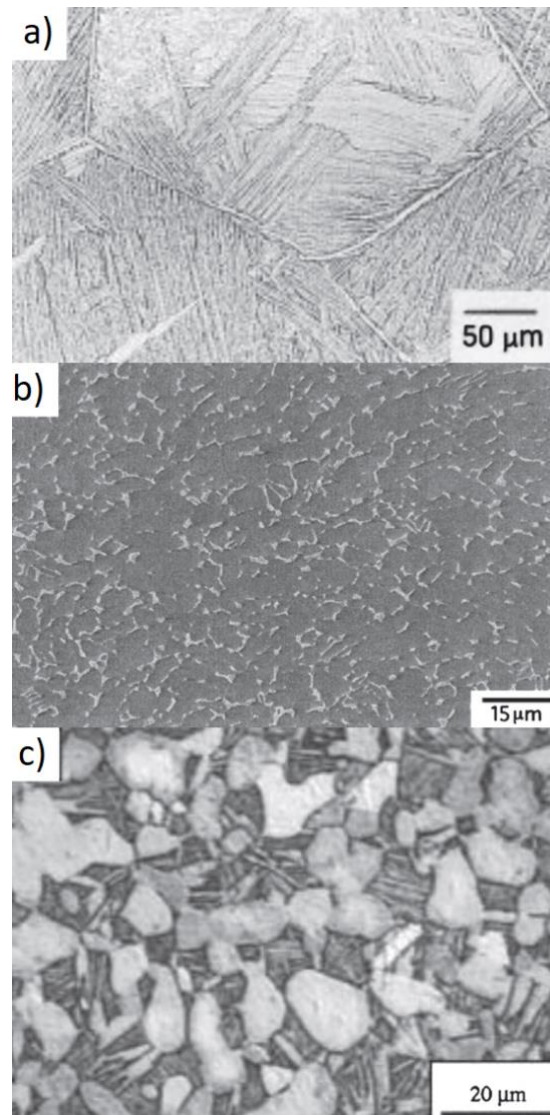


Figure 2.4 The main microstructures of Ti-6Al-4V, a) lamellar (top), b) equiaxed (middle), and c) bimodal (bottom) [12].

2.1.2.1. The Microstructure

Firstly, lamellar microstructure is formed as a result of a controlled cooling rate, which leads to different structures (basket weave, widmanstätten, or martensitic). A slow cooling rate for the alloy from a high to low temperature across the β transus temperature (T_{β}) leads to a nucleation of laths and colonies of α phase along the grain boundaries of β phase [13]. In addition, when the alloy is cooled at a faster rate i.e. in the air, fine laths of α phase will nucleate along the grain boundaries, but with different orientation (basket weave)

[13]. A faster cooling rate still (such as for water quenching) leads to the widmanstätten arrangement which is finer layers of orthorhombic martensite α'' aligned similarly with the β grains and finer layers of hexagonal martensite α' if the water quenching is carried out above 900 °C [14].

Secondly, an equiaxed microstructure can occur because of deformation and recrystallisation processes. This consists of equiaxed grains that form as a result of breaking lamellar layers by thermomechanical processes such as heat treatment, extensive deformation, and annealing [15]. Obtaining an equiaxed structure in the alloy may require 70% reduction in the section (the percentage deformation) followed by annealing and slow cooling from 925 °C [16].

Finally, the bimodal structure contains the two other structures at the same time, a lamellar matrix of ($\alpha + \beta$) and equiaxed α grains [17]. This structure can be achieved by the deformation and recrystallisation processes of $\alpha + \beta$ phase. When the annealing process happens at high temperature (below T_β), the equiaxed α grains nucleate within the colony lamellar matrix of ($\alpha + \beta$) with different sizes and volume. The α grains are called primary α (α_p) and the size of the grains is around 20 μm , though this can be controlled by the quenching and ageing processes and also the recrystallisation temperature [17].

2.1.2.2. The Mechanical Properties

Extensive research has found that the texture and crystalline orientation of the crystals have an impact on their mechanical properties [18]. Mechanical anisotropy in terms of texture is a result of the interaction with the crystallography of defects and deformation processes in the structure such as dislocations and twinning. The main reason for titanium alloys being anisotropic in terms of mechanical behaviour is the hexagonal unit cell structure of the α phase [19]. The hexagonal structure has in theory only four independent slip systems, which is lower than the cubic structure (6) or face centred cubic (12) [20], and indeed is lower the 6 slip systems required for compatibility between grains in a polycrystalline material. In practice, the c/a ratio of the hexagonal structure plays a key role in the slip systems that are active; for materials which have c/a ratio less than 1.633, (the

ideal ratio) Ti basal and prismatic slip systems can operate, while materials with the ideal c/a ratio have basal slip only [20].

The values of the mechanical properties of Ti-6Al-4V can only be expressed as ranges, due to phase changes in the alloy, and the variations in texture, impurities, and heat treatments. The main mechanical properties have been reported to usually lie in a range between 100 – 130 GPa for the Young's modulus (E), 890 – 930 MPa and 820 – 860 MPa for the ultimate tensile strength (σ_{ut}) and yield strength (σ_y) respectively [5]. Ti-6Al-4V alloy shows a slightly better performance under compression tests than tensile, also it has high fatigue strength and good corrosion resistance and biocompatibility [21]. These properties suggest Ti-6Al-4V as an excellent candidate for aerospace production, structural and biomedical applications as a lightweight material [21]. Nevertheless, Ti alloys are expensive, and so efficient manufacturing methods that form shapes allowing their properties to be fully exploited are desirable.

2.2. Additive Manufacturing (AM)

In 1986, Charles W Hull invented a revolutionary method that created a three-dimensional product by stereolithography [22]. The main concept of this method, which is now also called Additive Manufacturing (AM), is creating an object by adding cross-sectional layers from the beginning (the base) to form the required part [22]. This is the main advantage of additive manufacturing over conventional manufacturing methods such as casting and forging, which start with a block then employ machining to reach the final part. Additive manufacturing has rapidly developed and introduced many specific techniques, all based on the same theory, and which have the ability to produce items from a range of materials (such as metals, polymers, and ceramics) which provides many advantages that can be used in the industry [23]. Other advantages of additive manufacturing are producing complex shapes quickly and easily and reducing the machining processes due to the high quality of the process, which leads to reductions in the time and the cost [24].

2.2.1. Additive Manufacturing Processes

Additive Manufacturing (AM) processes, which are also termed 3D printing, have different classifications. In 1991, Jean-Pierre Kruth classified AM processes based on the creation of material from a) solid, b) liquid, c) gas, and d) powder based [25, 26]. Recently, the American Society for Testing and Materials (ASTM) categorised AM processes to 7 groups (Table 2.2); 1) sheet lamination, 2) material extrusion, 3) power bed fusion, 4) binder jetting, 5) material jetting, 6) directed energy deposition, and 7) vat photopolymerisation [27].

Despite the difference in the mechanisms and features, all AM processes use computer aided design (CAD) software such as AutoCAD, Netfabb, and Magics, as shown in Figure 2.5. In a common embodiment of the process, this is used to design the object and create a STL (stereolithography) file then convert it to a format that can be readable by the machine, and finally the build operation is ready to begin. When the build begins, the material is layered in the x-y plane and the heat source, which is usually an electron beam or a laser, is directed along the z axis [28].



Figure 2.5 An image illustrating basic AM design or a component (layer by layer) [28].

Each AM process has advantages and disadvantages and choosing the appropriate method depends on several factors such as the material, the complexity of the design, the number of products, and the properties of the final item [29]. The next section will focus on the AM process that is used in this project, Selective Laser Melting (SLM) and compare it with other Powder Bed Fusion (PBF) (the family it is part of) methods.

The machine capability is vital to determine the final properties of the product in Additive Manufacturing processes. Knowing the role of the machine parameters and its impact on the product properties will ease and help to choose the suitable settings before the build. Moylan et al. [30] developed a specific artefact design for the National Institute of Standards and Technology (NIST). This is a standard build, which can be used to calibrate and compare machines. The artefact, as shown in *Figure 2.6*, includes different features, to represent such forms as are typically found in products of complex shape, to explore (in a single build run) the machine and laser behaviour during the building process. The structure includes specific geometries such as vertical walls, holes with different diameters, and

interior cavities. The artefact is good as comparing tool between different AM machines; the different features produced still need to be investigated post build, for dimensional performance, defects and microstructure, for example, which can still be time consuming. It also does not explore all factors, for example the powder has a key role to determine the product properties and using different powder grade could give very different results.

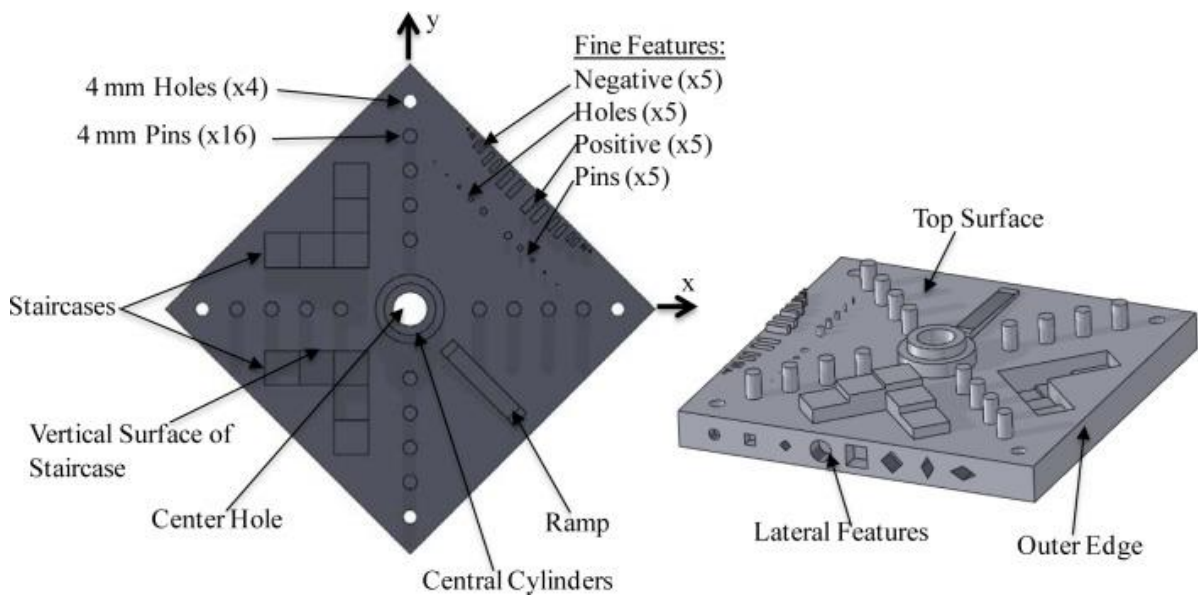


Figure 2.6 A diagram showing the NIST artefact to test machine capability and accuracy [30]

Table 2.2 ASTM classification of AM processes [27, 31].

Category	Methods	Material	Power Source	Strengths (•) / Weaknesses (-)
Sheet Lamination	Laminated Object Manufacturing (LOM)	Metallic sheet, ceramic Tape	Laser Beam	<ul style="list-style-type: none"> • High surface finish • Low cost - Decubing issues
Material Extrusion	Fused Deposition modelling (FDM)	Ceramics, Metals, Plastic	Thermal Energy	<ul style="list-style-type: none"> • Inexpensive machine • Multi material printing - Limited resolution - Poor surface finish
	Contour Crafting			
Power Bed Fusion	Selective laser sintering (SLS)	Polymers	High power laser beam	<ul style="list-style-type: none"> • Fully dense. • High Accuracy • High strength & stiffness - Needs for support parts - Treatment / recycling the powder
	Direct Metal Laser Sintering (DMLS)	Metal Powder (Stainless Steel, Ti-6Al-4V, Aluminium)		
	Selective Laser Melting (SLM)			
	Electron Beam Melting (EBM)		Electron beam	
Binder Jet	Indirect inkjet Printing	Powder (Metal, polymer, ceramic)	Thermal Energy	<ul style="list-style-type: none"> • Colours parts • Wide material selection - High porosities/ poor finishing
Material Jet	Polyjet / inkjet printing	Photopolymer, wax	Thermal energy/ photocuring	<ul style="list-style-type: none"> • Multi material printing • High surface finish - Low strength
Directed Energy Deposition	Laser Engineered Net Shaping (LENS)	Molten Metal powder	Laser Beam	<ul style="list-style-type: none"> • Repair damaged parts - Require post processing.
	Electronic Beam Welding (EBW)			

2.2.2. Selective Laser Melting (SLM)

In 1980s, Selective Laser Melting (SLM) appeared as a new method of additive manufacturing that uses a laser beam as energy source to melt selected parts of a powder bed to form a product [31]. As a new manufacturing process, Selective Laser Melting (SLM) has advantages over traditional manufacturing process such as casting and forging, mainly reducing the cost of production by dispensing with the expensive mould and post processes, a high level of dimensional accuracy, the capability to produce items with different geometry in the same build, and finally SLM has the ability to form complex shapes that cannot be produced by traditional manufacturing processes [32].

In SLM, the process to produce an object is direct by melting certain areas of the powder layers by a laser, as shown in

Figure 2.7 [33]. In detail, the laser (energy source) focuses on selected spots of a powder bed, which is spread on solid substrate, these areas will start melting to form a pool of liquid. Subsequently, the liquid pool solidifies quickly to form a slice of the product. Then, the build platform moves down by the thickness of the layer (depending on the CAD design) and the wiper spreads a new layer of the powder over the platform. The process repeats until the build is completed and the final product is finished. The unmelted powder remains in the chamber as a supporter for the product during the build and is sieved after the process is finished to reuse. The quality of the final product could be determined by many factors such as laser properties, build strategy, and powder particles used [34].

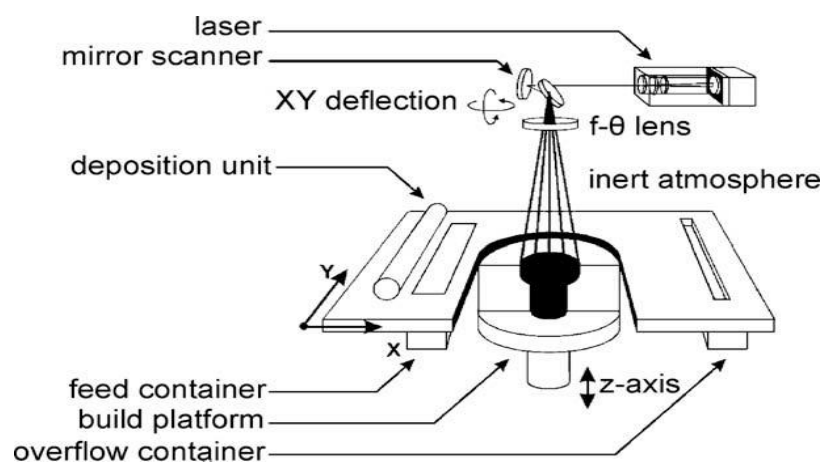


Figure 2.7 A schematic description of a selective laser melting process [34].

As any production process, Selective Laser Melting (SLM) has some challenges that could affect the final product and should be considered during and after the process. These include the thermal stresses, segregation, non-equilibrium phases, and the melt pool behaviour [35]. One of the main issues of SLM is the thermal stress, which is a result of the high difference in temperature between the layers; as shown in Figure 2.8, the upper layers that face the laser will expand as a reaction to the heat, while the lower layers which are rooted, will resist this expansion and the result of this will be that stresses between the layers could form cracks while partially solidified leading to segregation in the product [36]. This problem appears in all processes that use a laser as a heat source and to overcome this problem a pre-heated bed is used to reduce the difference in temperature between the layers of powder. The pre-heating bed could also have a positive impact on the product density [37].

Another important feature which should be considered is the melt pool behaviour and there are some factors relevant to this phenomenon, such as the laser parameters (the power, scanning speed, spot diameter, and scanning strategy) and the dimensions of the melt pool [38]. The high temperature gradients, which are caused by the high speed of laser scanning, convert the powder to molten material which affects the nucleation of the solid phase by two phenomena, a) wetting or b) capillarity. Wetting is the ability of maintaining contact between a solid surface and a liquid, whereas the capillarity is the ability of a liquid to move in narrow spaces without an external force [39], both can affect the shape and the size of the solid phase and induce non-equilibrium and non-stable phases which form small spherical shapes known as “balling” [40]. The size of the balling is relating to the scanning speed. When the speed is high (400-500 mm/s) the droplets are invisible, Figure 2.9 [41].

Other factors may have influence on the surface finish, such as the material absorption which plays a key role in the surface roughness as the absorption value of powder is higher than the values of bulk or flat surfaces in the SLM process [42]. The complexity of selective Laser Melting (SLM) may cause some defects and porosity in the product, which influence the microstructure and the mechanical properties of the item, so this requires a

better understanding to overcome these challenges and to estimate the achievable properties while at the design stage.

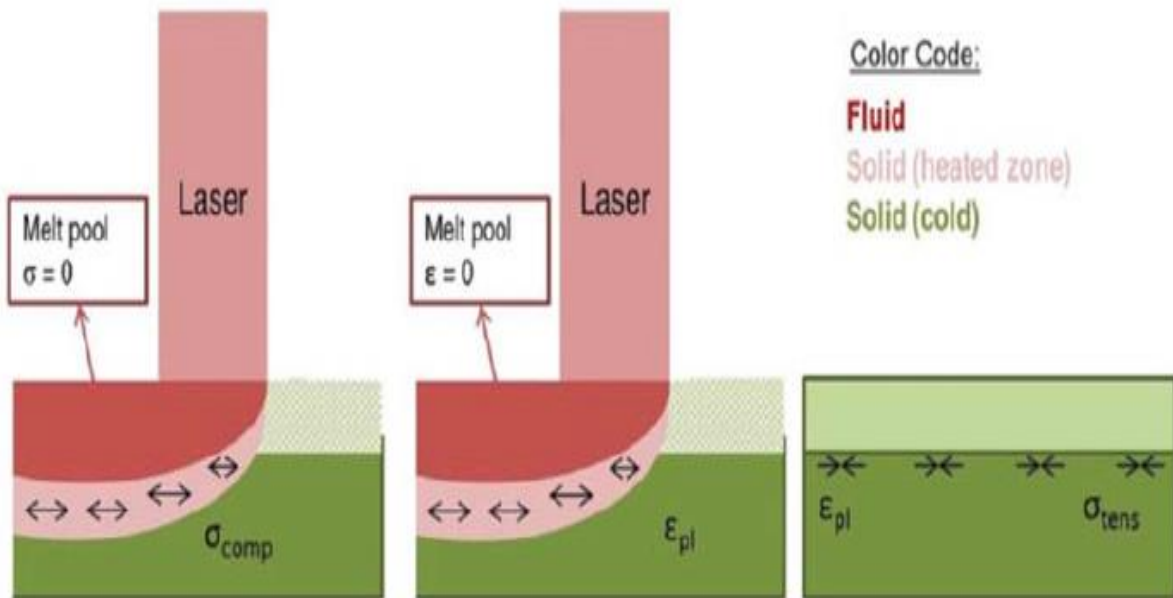


Figure 2.8 A schematic of thermal stresses formation between powder layers during SLM [36].

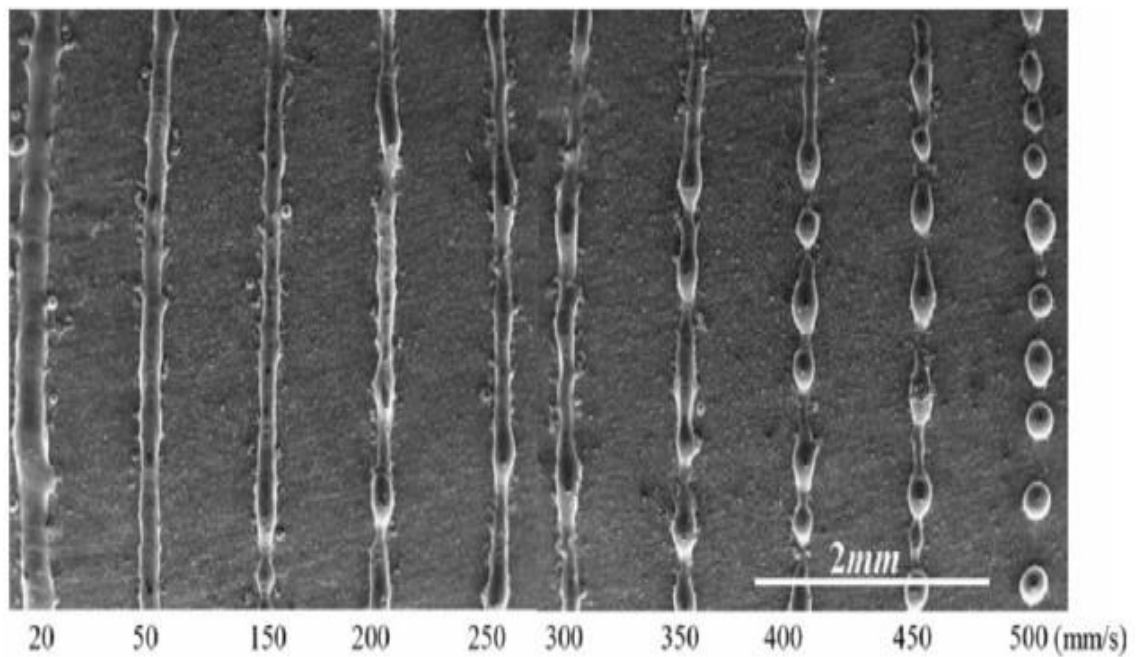


Figure 2.9 A SEM image showing the balling formation with different scanning speeds [42].

Surface quality in additive manufacturing processes, such as selective laser melting (SLM), is significantly impacted by what is known as the "stair step" effect [43]. This effect arises due to the layer-by-layer additive deposition and fabrication of curves and inclined surfaces. This phenomenon is inherent to all additive layer manufacturing (ALM) techniques. While decreasing layer thickness can potentially enhance surface finish, achieving excellent surface quality is a critical challenge in SLM production. The issue is that inadequate surface quality can lead to extensive and costly post-finishing procedures, often done manually due to the complex shapes of the produced parts. This can counteract the benefits of utilizing additive manufacturing processes for industrial production [44]. As the angle of inclination from the horizontal plane increases, the stair-step effect results in higher surface roughness. Notably, on inclined surfaces, unlike horizontal ones, SLM technology cannot achieve laser remelting, due to the constraints of the orientation of the laser relative to the build plane. The measured surface roughness exhibits a consistent trend within the range of 5° to 45° inclination angles, relative to the build direction. In the range of 50° to 90°, there is a relatively gradual reduction in the measured roughness. This suggests that surface roughness remains relatively stable for moderately inclined surfaces, while there is a decrease in roughness which becomes more gradual as the inclination angle becomes steeper. The stair-step effect due to layered fabrication influences surface quality in ALM processes, particularly in SLM. Surface roughness tends to increase with greater inclination angles. Maintaining a sufficiently good surface quality (noting that surface finish requirements may be more demanding in surfaces that need to be joined to other parts, or where the loading condition increases the risk of fatigue, for example) is crucial to prevent the need for post-finishing and to preserve the advantages of using additive manufacturing for industrial applications [45].

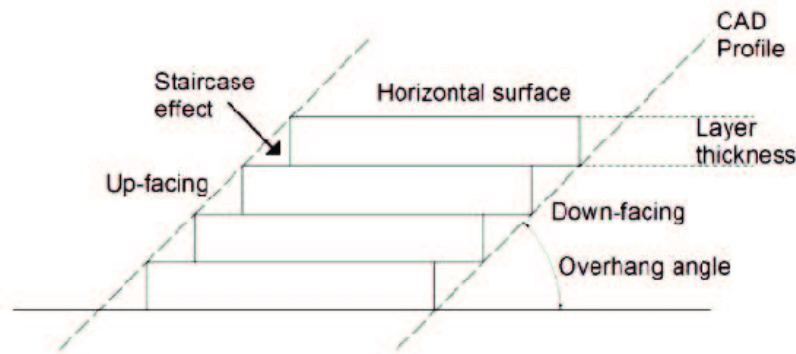


Figure 2.10 The Staircase effect in AM parts [46].

The most effective strategy to enhance surface quality is through post-build polishing, which reduces surface roughness and eliminates critical defects in the surface region that can lead to stress concentration and crack initiation [47]. As a result, post-processing methods like machining, chemical etching, and vibrahoning are frequently employed to achieve smoother surfaces, ensuring the overall performance and reliability of additive manufacturing parts. Formanoir et al. [47] demonstrated that polished specimens display a greater strain to failure compared to specimens in their as-built state. This improvement arises from the mechanical removal of critical defects present on the surface; these defects can lead to stress concentration and serve as points where cracks initiate. In actual applications, nearly all additive manufacturing (AM) parts will necessitate some form of post-processing to enhance surface smoothness. For simpler structures, this might involve machining [47, 48], and for more intricate geometries, techniques such as chemical etching and vibrahoning [49] could be employed to achieve a smoother surface.

In addition, another challenge facing the products that processed by SLM is the “up-skin” and “down-skin” surface roughness, as shown in Figure 2.10. Up-skin surface roughness is intricately tied to the geometry of step edges and the presence of partially melted particles attached to these edges. As the length of steps decreases, the number of partially melted particles along these edges increases, thereby contributing to the overall roughness of up-skin surfaces [43]. On the other hand, addressing down-skin surface roughness presents a different set of complexities. The fusion zone of down-skin surfaces relies on the underlying powder bed. However, the heat dissipation process in this region is notably slower, due to the limited contact between powder particles, resulting in insulating air gaps between them [50, 51]. When a laser exposes an overhanging surface surrounded

by the powder bed, it triggers the formation of larger melt pools. The combined effects of gravity and capillary forces cause these melt pools to extend into the powder bed [52]. The outcome is the attachment of more semi-melted powder particles to the surface [53]. As these particles solidify, they can lead to an elevation of the surface by curling up from the powder bed [54]. Consequently, down-skin surfaces typically exhibit higher roughness compared to their up-skin counterparts. Managing these differing surface roughness characteristics presents a significant challenge for designing appropriate processing parameters in SLM. Numerical calculations have shown that melt pool size increases in the vicinity of down-skin surfaces due to inadequate cooling of previously scanned hatches and layers. Furthermore, the relatively sluggish heat dissipation in the powder-supported area contributes to the formation of larger melt pools [54]. To address these issues, a faster scan speed is recommended as a corrective measure. This adjustment can be achieved through either real-time monitoring and adjustment [52] or a controlled gradual modification of laser exposure parameters. This transition from parameters suited for the core to those optimized for overhanging structures and downward-facing inclined surfaces can help to mitigate the increased melt pool size effect [55].

2.2.2.1. Microstructure and Mechanical Properties

The manufacturing process has an important role to determine and characterise the final microstructure of the product. As described in the previous section, the item is exposed during the SLM process to rapid cooling and solidification with a high difference in temperature, both spatially and with time, which causes residual stresses and porosity [56]. Ti-6Al-4V alloy manufactured by SLM has two main microstructures: a) α' martensite and columnar β grains, and b) lamellar $\alpha + \beta$ phases, as shown in Figure 2.11 [57]. The dominant microstructure of Ti-6Al-4V as-fabricated by SLM is the α' martensite and columnar β grains due to the rapid cooling rate, while the lamellar $\alpha + \beta$ phases can be achieved by either adjusting the machine parameters such as the laser scanning speed or by post processes such as hot isostatic pressing (HIP) [57].

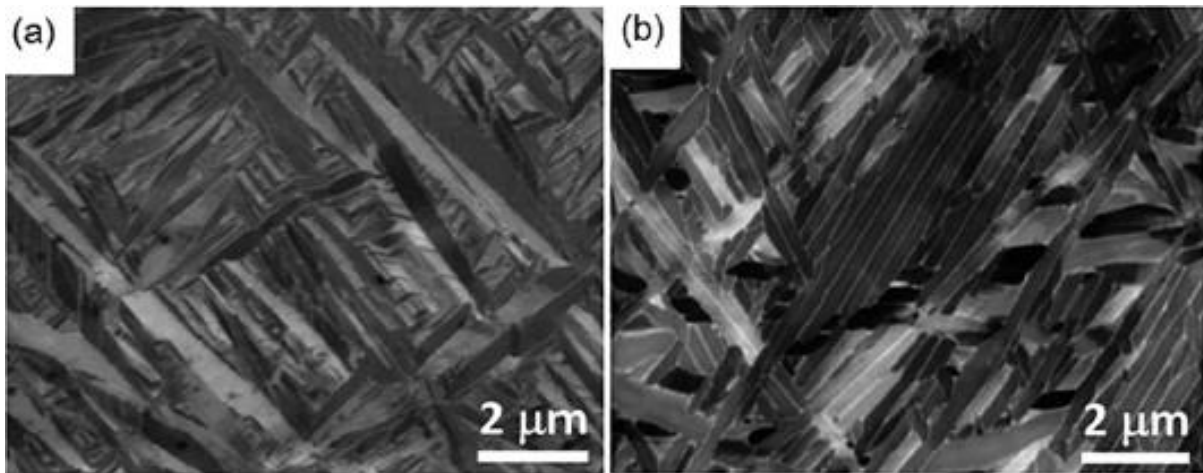


Figure 2.11 The two microstructures of Ti-6Al-4V via SLM, a) α' martensite, and b) $\alpha + \beta$ phases [57].

In general, Ti-6Al-4V alloy fabricated by SLM has a higher strength than other AM or conventional processes which reach 1300 MPa for yield strength (σ_y) [57]. On the other hand, the ductility and fatigue life are lower than the other processes due to the porosity between layers and the surface roughness that result from the microstructure of α' martensite [58]. The changing of α' martensite phase to a series of $\alpha + \beta$ phases has an effect on the mechanical properties which increases the ductility and fatigue life but also decreases the strength, so the use in structural, biomedical, or aerospace applications determines the various combinations of desirable properties [58, 59].

Selective Laser Melting (SLM) and Electron Beam Melting (EBM) processes have the same principle in melting a certain area layer by layer, however the difference between the two processes is the energy source that is used to melt the layers, a laser in SLM and an electron beam in EBM; this has an effect on the final microstructure [58]. As described in the previous section, the microstructure of Ti-6Al-4V by SLM is mainly α' martensite and prior β grains, while the microstructure of Ti-6Al-4V by EBM is lamellar microstructure consisting of α and β phases. The microstructure difference is due to the different cooling rates between the processes which affect the transition of β to α phase via transus temperature (T_β) [60]. SLM has a higher cooling rate than EBM and that leads to transformation of most of the β phase to α' martensite, but both processes have clear grain boundaries of β phase, as shown in Figure 2.12 [60].

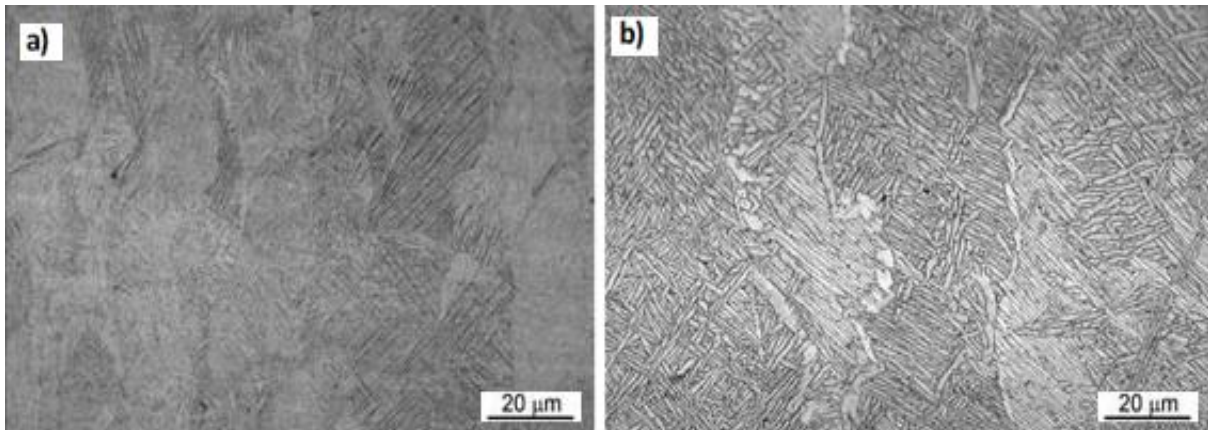


Figure 2.12 Optical micrographs (OM) of Ti-6Al-4V produced by SLM (left) and EBM (right) [60].

The microstructure of the alloy is a significant factor to determine the mechanical properties and the relationship between them has been investigated and compared by researchers [15, 21, 23, 33, 57-62].

Table 2.3 and Figure 2.13 summarised a number of these studies that use Ti-6Al-4V powder via AM processes (SLM, EBM) and it shows that SLM has higher tensile strength than EBM. Moreover, some studies have linked the anisotropy in the mechanical properties of material made by both processes to the anisotropy of the microstructure [62].

Table 2.3 Comparison of reported mechanical properties of Ti-6Al-4V via SLM and EBM.

AM process	Yield Strength (MPa)	Ultimate Tensile Strength (MPa)	Ref
SLM	1125	1250	[15]
SLM	1333	1407	[23]
SLM //	1143	1219	[60]
SLM ⊥	1195	1269	[60]
SLM	1098	1237	[62]
EBM	962	1011	[62]
EBM //	869	928	[60]
EBM ⊥	899	930	[60]

(//) the sample tested parallel to the build direction.

(⊥) the sample tested perpendicular to the build direction.

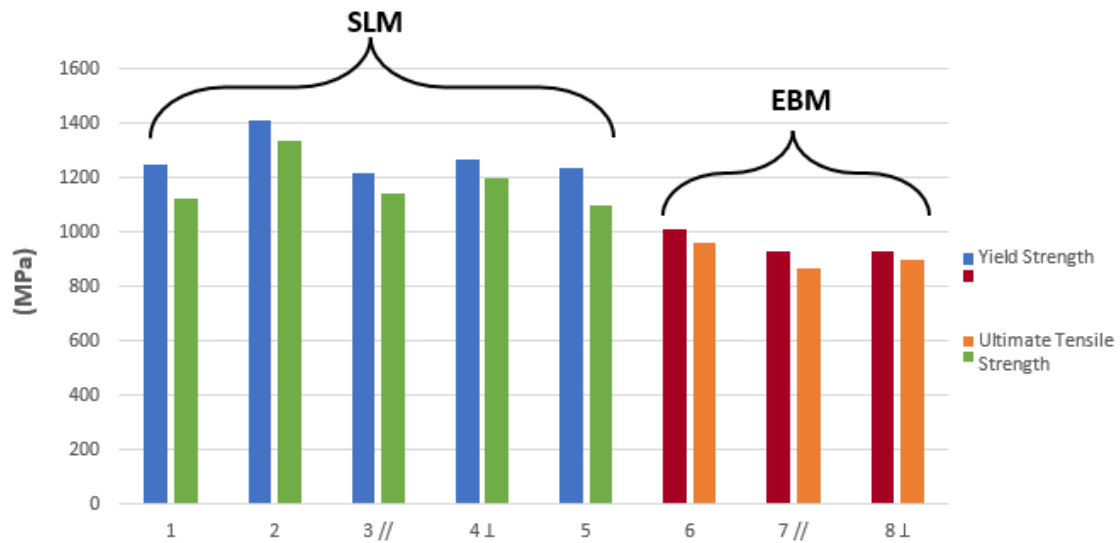


Figure 2.13 Bar graph of mechanical properties of Ti-6Al-4V produced by AM. Data from

Table 2.3.

In addition, there are a number of features affect the crystallographic microstructure such as dislocations and precipitation, which can enhance or deteriorate the strength and toughness of AM products.

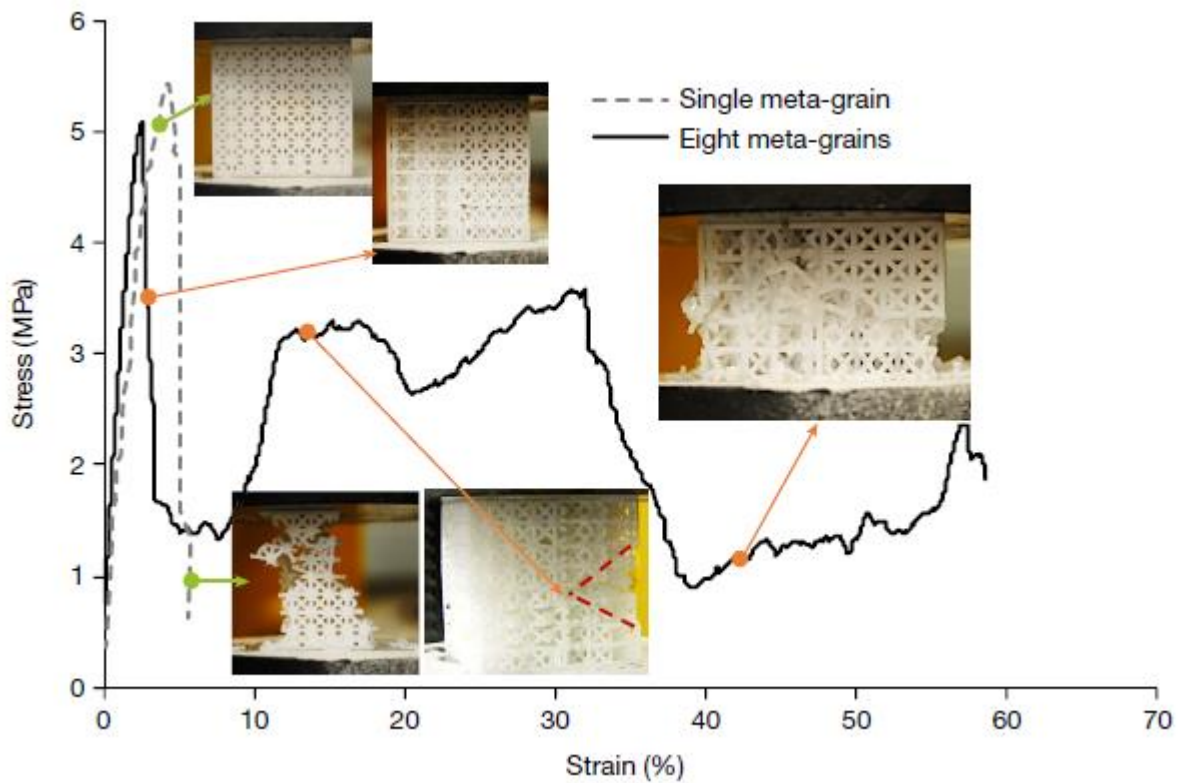


Figure 2.14 A Stress-Strain curve comparing between single meta-grain and eight meta grains of architected structures [63].

2.3. Lattices

A lattice can be defined as network or array of free volume in individual cells that are connected by a series of trusses [64]. There are other terms for lattices, which may also be known as cellular materials. These materials are classified depending on the shape of the structure as a) materials which have organised pores such as lattices or b) materials which have random pores such as sponges and foams [65]. The randomness of the pores has an effect on the properties of the material which can be anisotropic for geometries that have random pores [65]. This group of materials have unique properties as they are often very light but also very strong which may be excellent for structural, aerospace, and medical industries. The properties of lattices depend on three factors: a) the material, b) the topology, and c) the relative density (ρ^*/ρ_s), where ρ^* is the lattice density and ρ_s is the solid density [64]. Ashby investigated the three principles that affect the lattices properties and made a flow chart to explain it briefly, as shown in Figure 2.15 [64]. Firstly, the properties of the raw material of the lattice (such as mechanical, thermal, and electrical properties) give a prediction of the final properties of the lattice. Secondly, the topology and the shape of the lattice which is have either random or organised pores, which is an important factor to determine the mechanism of the deformation [66].

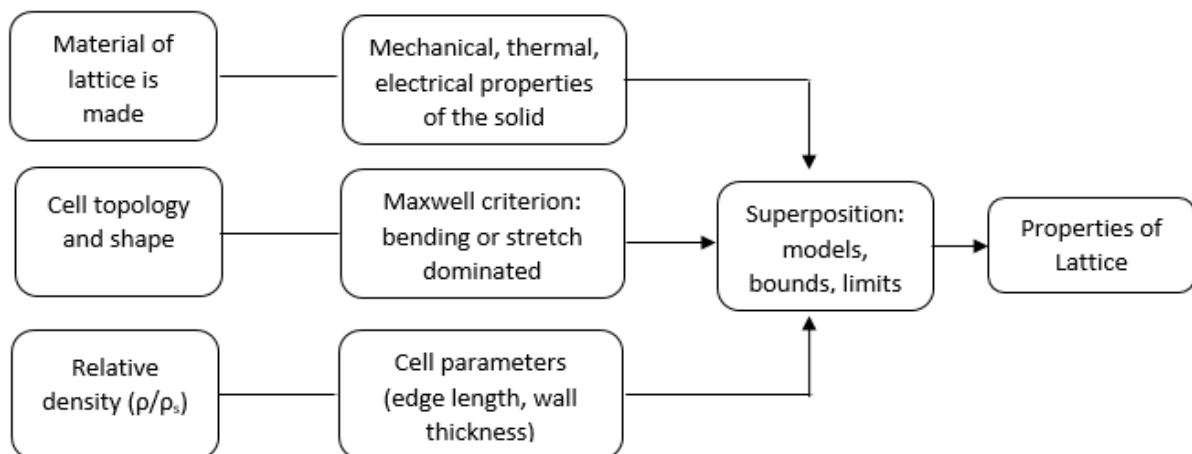


Figure 2.15 A flow chart shows the factors that have influence the properties of lattice [64].

There are two deformation mechanisms in lattices and cellular materials, a) bending, and b) stretching deformation as shown in Figure 2.16. When a force is applied to the unit cell of the lattice, the connectivity between the elements will determine the type of deformation. Bending behaviour is more likely to occur where there is low connectivity between the elements, while stretching behaviour occurs with high connectivity between the elements [67]. In the bending deformation case, the struts of the structure will start bending and buckling at the edges due to the load that is applied. On the other hand, rigid structures that have no flexibility at the nodes will start stretching by elongation of the struts in the long dimension under tension or break under compression due to lack of flexibility in the nodes [68]. Furthermore, the elastic properties of the structure are different between bending deformation and stretching deformation, which directly affect the stress-strain curve as shown in Figure 2.17.

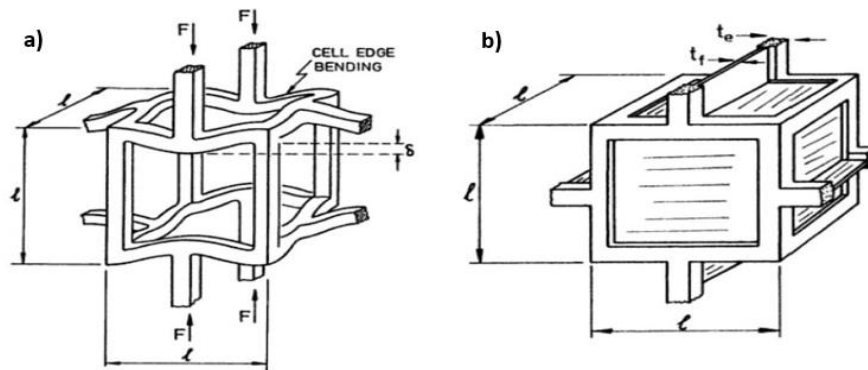


Figure 2.16 The two deformation mechanisms in cellular materials, a) Bending, b) Stretching [64].

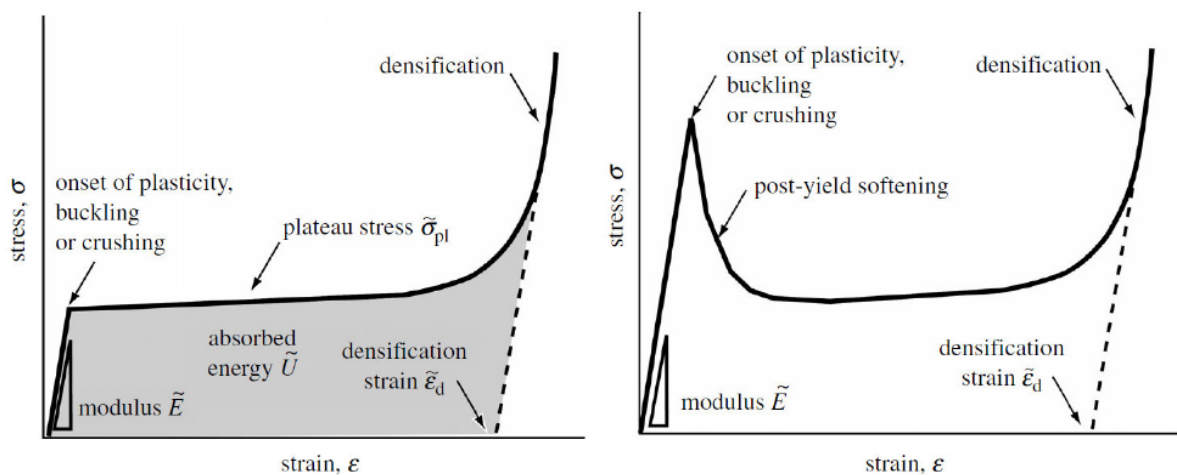


Figure 2.17 The stress-strain curves of cellular materials where the microstructures are dominated by bending deformation (left) and stretching deformation (right) [64].

Lastly, the third factor that affects the properties of the lattices is the relative density of the lattice (ρ^*/ρ_s) which plays a key role to determine the elastic properties such as stiffness (k) or young's modulus (E), and plastic properties such as yield strength (σ_y) and strain (ϵ). In an open cell structure, which is the main interest of this project, the relationship between the relative density and the Young's modulus is derived for a simple structure such as that shown in equations 1.1 and 1.2 from Timoshenko's beam theory [64].

$$E^* = \frac{\sigma}{\epsilon} = \frac{C_1 E_s I}{t^4} \quad (1.1)$$

where the relative density in three dimensional structures related to the thickness of the edge (t) and the cell size (L) and it can be expressed as $\rho^*/\rho_s \propto (t/L)^2$, so

$$\frac{E^*}{E_s} = C_1 \left(\frac{\rho^*}{\rho_s} \right)^2 \quad (1.2)$$

where E^* is the young's modulus of the lattice,
 E_s is the young's modulus of the solid,
 C_1 is estimated to be approximately 1 [64].

Pham et al. [69] investigated the effect of component size on the crystallographic microstructure by using architected materials, which is a designed material replicating some of the features of crystals within metals, with different regions having specific strut arrangement with the same orientation at the mesoscale. The aim by using this type of designed material was to reduce the propagation of shear failure bands through the lattice (in the same way that different grain orientations can block the slip of dislocations), The mesoscale structure was designed, and then created in a polymeric material by Fused Deposition Modelling (FDM). The results (Figure 2.14) showed that samples with a high number of meta-grains were successful in stopping cracking because of the boundaries between the grains and this lead to an increase the toughness of the architected structure. The approach of this study simplified potentially complicated structures to a small number of crystals representing a microstructure, and showed that such designs can enhance these crystals for particular purposes, such as strengthening or toughening.

A considerable number of studies have investigated the effect of these factors on the mechanical and thermal properties such as yield strength, Young's modulus, and thermal conductivity for different geometries [67, 70-75].

2.3.1. The Geometry

As discussed in the previous section, the importance of the lattice shape leads to focus on the geometry design which can enhance the structure for particular applications. Aerospace and medical industries have the most developed applications for lattices because of it being considered as a light weight metal [65]. In addition, different designs and geometries are examined to achieve the desired properties leading to a proliferation of investigations by researchers. Rashid et al. examined three different geometries of AlSi12 lattices fabricated by SLM under bend testing [76]. The samples shapes were hexagonal, circular, and triangular that fitted in solid boxes as shown in Figure 2.18; this study compared the lattices performance with that of the solid. As expected, the solid samples showed better performance in terms of the strength level compared to the three lattices, as shown in Figure 2.19a (though also would have had reduced density). All the samples (except the hexagonal) show a sudden brittle failure as shown in Figure 2.19 [76].

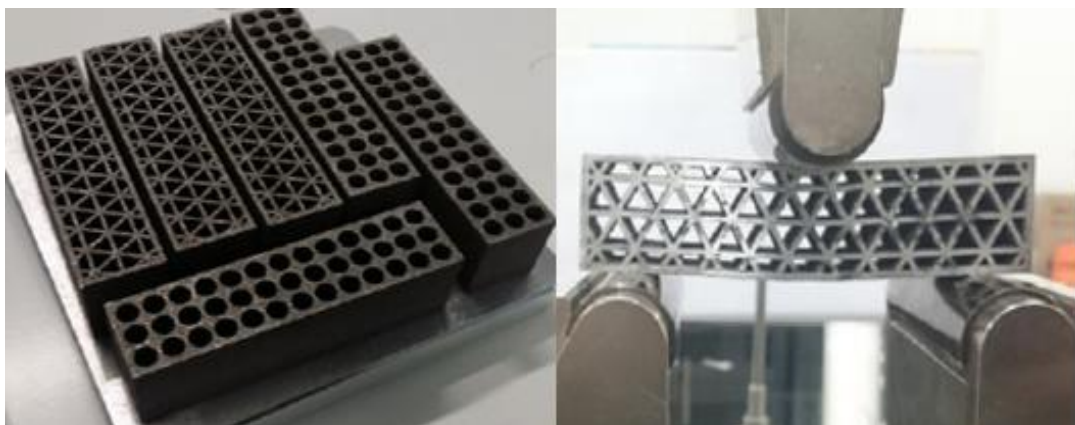


Figure 2.18 The different lattices fabricated by SLM (left), the sample during bend test (right) [76].

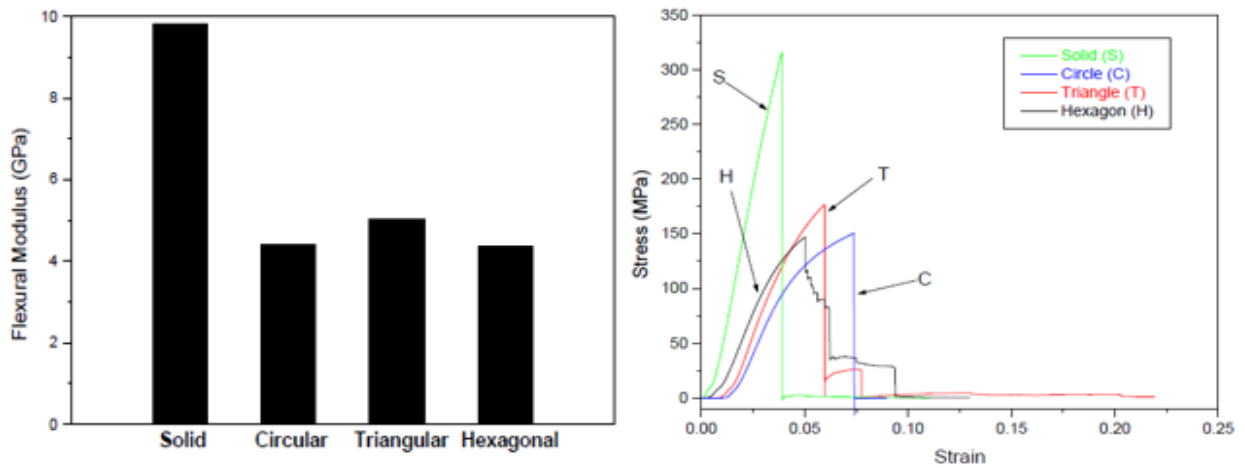


Figure 2.19 The comparison between the different lattices and the solid [76].

In addition, Sallica-Leva et al. examined the mechanical properties of Ti-6Al-4V cubic lattices fabricated by SLM to compare it with another study by Parthasarathy et al. [71] who used Ti-6Al-4V cubic lattices fabricated by SEBM [75]. The two studies have similar factors such as the structure and the material, but they differed in the manufacturing processes and this comparison revealed that lattices made by SLM have a higher ultimate compression strength than lattices by SEBM, as shown in Figure 2.20. Sallica-Leva et al. also compared two different energy inputs, high (HEI) and low (LEI). The lattices that made by high energy input have thinner struts and higher O₂ and N₂ content which could be the reason for the high mechanical properties [75].

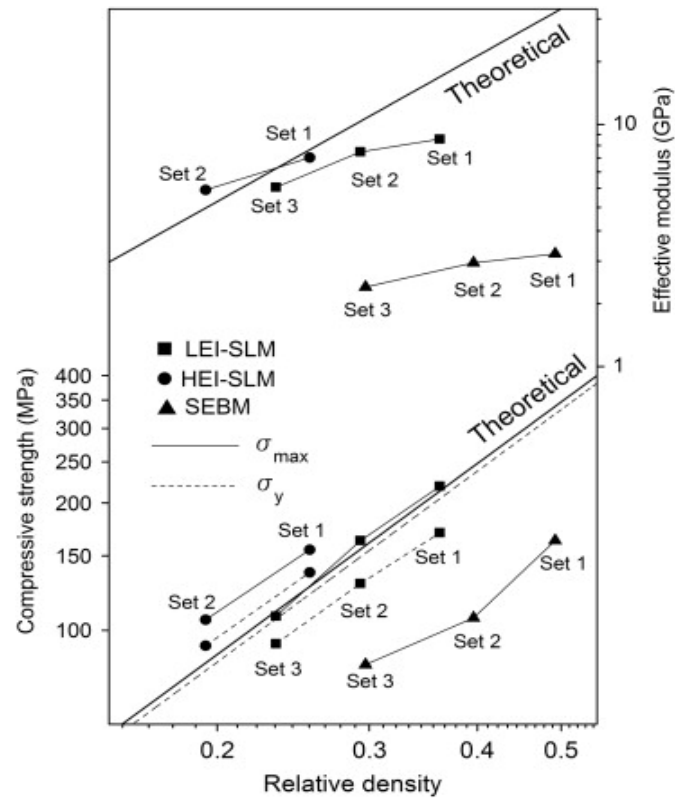


Figure 2.20 The mechanical properties of Ti-6Al-4V lattices that made by SLM and SEBM [75].

Furthermore, Horn et al. examined different geometry of Ti-6Al-4V lattices [72]. Different cell sizes of rhombic dodecahedron structure with different relative densities, as shown in Figure 2.21, fabricated by EBM to investigate the relationship between the relative density and the strength of the structures. The result of bend tests showed agreement with the Gibson-Ashby model, in that higher density structures have higher strengths [72]. The rapid development in industries that may use lattices has led to an increase in studies on different shapes and structures. Researchers have used the Finite Element Method (FEM) to simulate and compare the models with the experiments and optimise the structures for specific applications. A study was conducted by Bonatti and Mohr to investigate the mechanical properties of different geometries of FCC lattices manufactured by SLM and compare them with computational estimations [73]. The stress-strain curves of the experiments were compared with the simulation results as shown in Figure 2.22; the results of the experiment were lower than the results of the simulation which could be the friction effect in the compressive testing used.

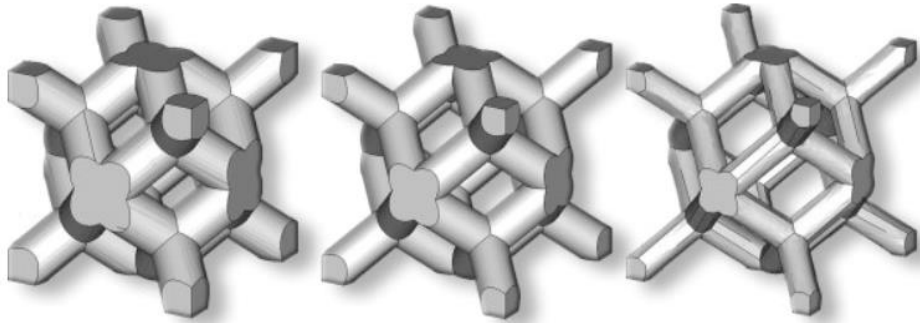


Figure 2.21 A unit cell of rhombic dodecahedron structure with different relative densities [72].

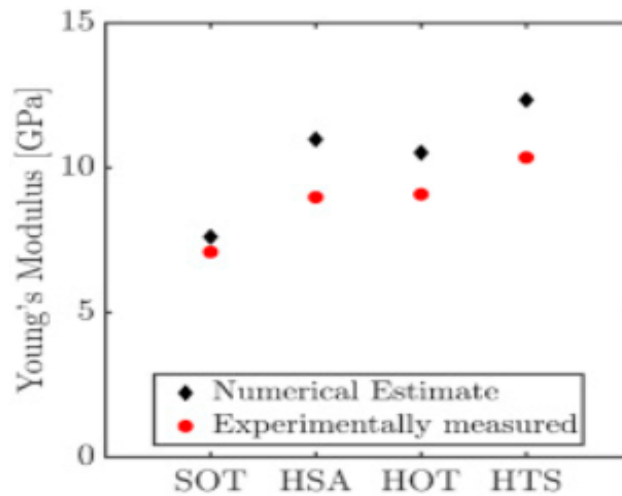


Figure 2.22 A comparison between simulation and experiment of four different samples [73].

Another study focused on different structure and geometry was conducted by Koizumi et al., these researchers aimed to optimise the mechanical properties of inverse body centred cubic (iBCC) structure, as shown in Figure 2.23, for biomedical purposes by using finite element method (FEM) [77]. The experiments were done by EBM that fabricated two different sets, with spherical and elliptical pores, and two different level of porosity, 70% and 80%, Figure 2.24 [77]. The experimental results show that the dense samples have higher strength, however, the surface roughness (which is commonly present in Additively Manufactured materials) affected the results and led to disagreement between the simulation and the experiment [77].

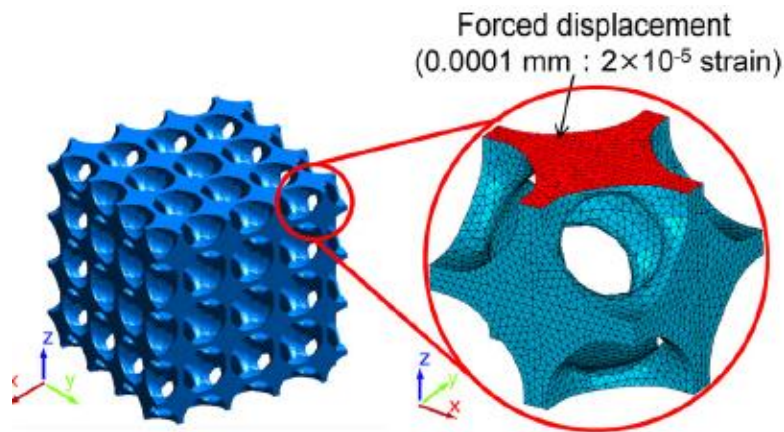


Figure 2.23 A model of iBCC lattice for finite element method [77].

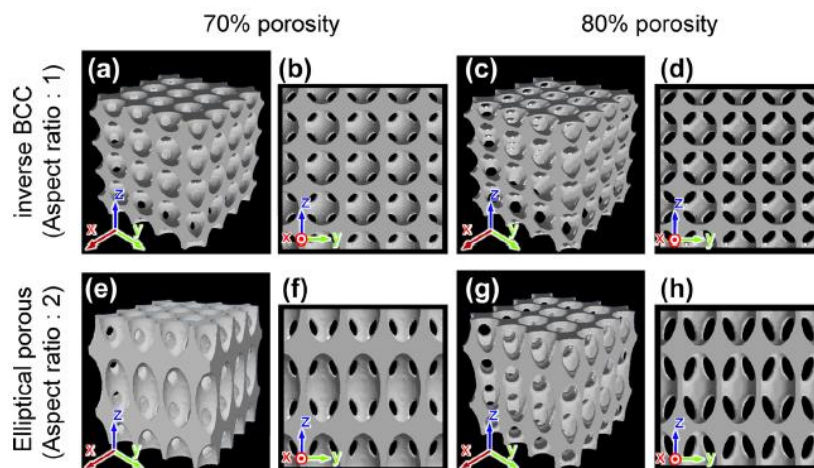


Figure 2.24 A set of designed lattices [77].

Nevertheless, numerical models are continually developing to be a comparing tool to the experiments. The microstructure and its imperfections in the physical samples such as surface roughness or defects, which could affect the experiments results, are not represented completely in the models. Ajdari et al. [63] and Li et al. [78] they studied the effect of cell shape imperfections, defects, and irregularity on the cellular structure using FEM. Another study focused on comparing the energy absorption in lattices structures in dynamic experimentally and numerically conducted by Ozdemir et al. [79, 80]. The study used different geometries for quasi-static and Hopkinson Pressure Bar (HPB) tests, and the results of FEM and the experiments were quite similar. The researcher used numerical models for further investigations and found the complexity of the shapes could affect the

FEM results and a simple structure of the unit cell could represent multi-layers unit cell impact behaviour and the imperfections also could have an effect on the results for complicated shapes.

In summary, there are number of studies which have investigated the relationship between the microstructure and the mechanical properties of Ti-6Al-4V manufactured by SLM. Most of these studies have concentrated on one or two shape characteristics that influence the microstructure. In addition, researchers focused on comparing between AM processes and traditional manufacturing processes or between AM processes themselves such as SLM and EBM. However, there have been no systematic studies that investigate the effect of different characteristics such as changing in the thickness, the build angle, and the relative densities on the microstructure Ti-6Al-4V lattices and the mechanical properties. Furthermore, the sheer variety of structures possible suggests that a simulation capability would be of value.

2.4. Simulation Techniques

Multiscale modelling is commonly utilized to make predictions of the development of microstructures in materials, owing to the significant spatial and temporal extent of microstructural variations, and the intricate nature of the processes involved [81]. In simulation materials science, different simulation methods are used for different spatial and time scales, as shown in Figure 2.25.

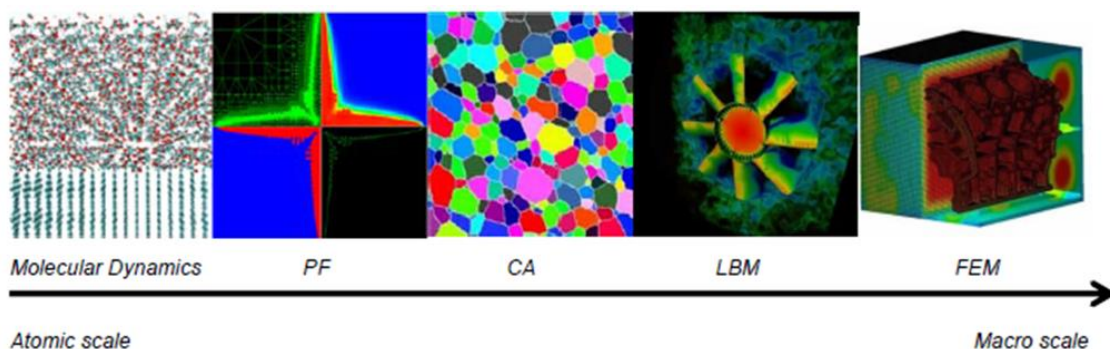


Figure 2.25 Multiscale modelling techniques scale representation [81].

The process of creating parts through SLM involves the rapid solidification of materials, leading to the formation of their microstructure. Simulating this phenomenon can be intricate. Tan et al. (2011) have attempted to predict the resulting microstructure in analogous processes such as laser welding, where rapid solidification can also occur [82]. They employed the cellular automata - phase field (CA-PF) method to forecast dendritic growth. Conversely, there has been extensive development in simulating the changes in microstructure during the solidification phase of the processes over time. These models have been developed using different simulation techniques such as FEM [83],[84], CA [85-88], PF [89-91], Monte Carlo (MC) [92-95], and more recently the Lattice Boltzmann Method (LBM) [96]; these models on their own had shown different strengths and weaknesses in terms of the scale, accuracy and computing efficiency of the models, and for this main reason a variety of combinations between the mentioned techniques have been explored. The most successful combinations that have been investigated are CA-FE [97, 98], PF-FE [99, 100], CA-PF [82], and CALBM [98, 101-103]. Each of these investigated connections have the objective of emulating distinct challenges that arise during the development of microstructure in metal components.

The SLM process is an AM process characterised by the use of a high powdered laser beam, which fuses metallic powder together in a layer-by-layer process. In literature, FEM has been widely used by researchers [39, 104-113] in order to simulate the microstructures and the temperature profiles generated in this process. The most representative research will be discussed in order to highlight the findings and weaknesses of each. Shiomi et al. (1999) employed the finite element method (FEM) to elucidate the shaping mechanism within laser systems [104]. They simulated the process of melting and solidification, validating their model by comparing calculated weights of solidified powder with experimental data. The calculated and experimental weights were in agreement, revealing that the highest temperature attained by the system was influenced more by the peak laser power than the duration of laser irradiation. However, it is important to note that this model was designed to simulate a solitary irradiation spot, and did not incorporate the intricate thermophysical properties of the powder, or the effects of the geometry of a real part into the model.

Matsumoto et al. (2002) introduced a technique utilizing finite element method (FEM) to compute temperature distribution within an individual metal layer formed on a powder bed during SLM [105]. Their approach accounts for transitions from powder to liquid to solid, predicting temperature profiles that inform stress development. However, it overlooks factors like the substrate plate beneath the powder bed, metallic powder absorption, and doesn't consider material properties as temperature-dependent. Despite lacking experimental validation, it was one of the earliest attempts at modelling powder-to-liquid-to-solid transitions. Roberts et al. (2009) employed FEM with an element birth and death technique to simulate temperature profiles resulting from laser irradiation across multiple layers in a powder bed [111]. The model was validated against experiments, enhancing comprehension of SLM, yet a more comprehensive model is necessary for accurate solidification prediction.

Song et al. (2012) emphasized the significance of SLM temperature distribution simulation for optimizing processing parameters [109]. Although their model featured basic thermally dependent properties and predicted very high temperatures, it aided in producing a component with desired porosity. This underlines the necessity of a meticulous FEM approach that precisely forecasts temperature profiles to optimize or predict processing parameters. Loh et al. (2015) devised a single-layer FEM model accounting for powder-to-solid transitions, volume shrinkage, and material removal [113]. Their model incorporates a "sacrificial layer" to achieve the desired temperature profile and melt penetration. While volume shrinkage was validated through experiments, the assumptions made restrict the model to simulating a single layer of powder bed, rendering it unsuitable for actual SLM processes. Recently, Foroozmehr et al. (2016) introduced a Finite Element Method (FEM) approach to simulate the size of the melt pool during SLM [112]. They incorporated the optical penetration depth of a laser beam into the powder bed, considering its dependency on powder size for defining the heat source. This three-dimensional single-layer powder bed model meticulously characterized thermal properties of solid and powder (excluding mushy zone properties) to simulate the powder-to-liquid-to-solid transition. Experimental data calibrated the optical penetration depth for more precise results. While the outcomes aligned with experiments, inter-layer interactions were not explored.

In a broader context, FEM has proven effective for simulating specific parts of the SLM process. Studying the FEM models revealed the necessity of accounting for melt pool flow and detailed thermal properties (including the mushy zone) to accurately predict temperature distributions and track solidification. This ongoing research emphasizes an in-depth exploration of powder-to-liquid-to-solid transformation, particularly emphasizing mushy zone properties, to create a more intricate solidification model.

Yin and Felicelli (2010) explored microstructural evolution in a metallic AM process using the Cellular Automata - Finite Element (CA-FE) [98]. Their model depicted dendritic structure formation within a melt pool during the LENS deposition process. However, this model concentrated on a small dendrite growth scale at a melt pool boundary and did not simulate solidification involving interaction between multiple melt pools or layers. Current research in this area aims to develop an FEM model capable of simulating the microstructure of components produced using the SLM process, encompassing a broader scope.

2.4.1. Finite Element Method (FEM)

The Finite Element Method (FEM) is a computational technique widely employed to solve complex problems in engineering, physics, and other scientific disciplines by analysing the complicated systems and structures by substituting them with simpler counterparts [114]. FEM divides a continuous domain into a finite number of smaller, simpler subdomains, referred to as finite elements. These elements are interconnected at specific points known as nodes, forming a mesh that approximates the geometry of the system under study. By discretizing the domain in this manner, FEM transforms the governing equations of the system into a set of algebraic equations that can be numerically solved. This substitution leads to obtaining an approximate solution rather than an exact one. The solution regions are constructed from numerous small, interconnected subdivisions known as finite elements, as shown in Figure 2.26. FEM has found extensive application in areas like structural mechanics, heat conduction, and fluid dynamics. It has been demonstrated as a valuable tool for numerically solving ordinary and partial differential equations, especially those related to microstructural evolution [115].

In a broader sense, as described by Rao (2011) [114], the finite element method represents the actual continuous body of matter as a collection of finite elements, as shown in Figure 2.26. These elements are interconnected at specified points called nodes or nodal points. Nodes are usually located on element boundaries where adjacent elements are connected. Since the precise variation of the field variable (e.g., displacement, stress, temperature, pressure, velocity) within the continuum is unknown, the variation inside a finite element is approximated using a simple function. These approximation functions, known as interpolation models, are defined based on the field variable values at the nodes. When formulating field equations for the entire continuum, the new unknowns become the nodal values of the field variable. Solving the resulting finite element equations, typically in matrix form, yields the nodal values of the field variable. Once known, these values, in combination with the approximating functions, describe the field variable behaviour across the collection of elements.

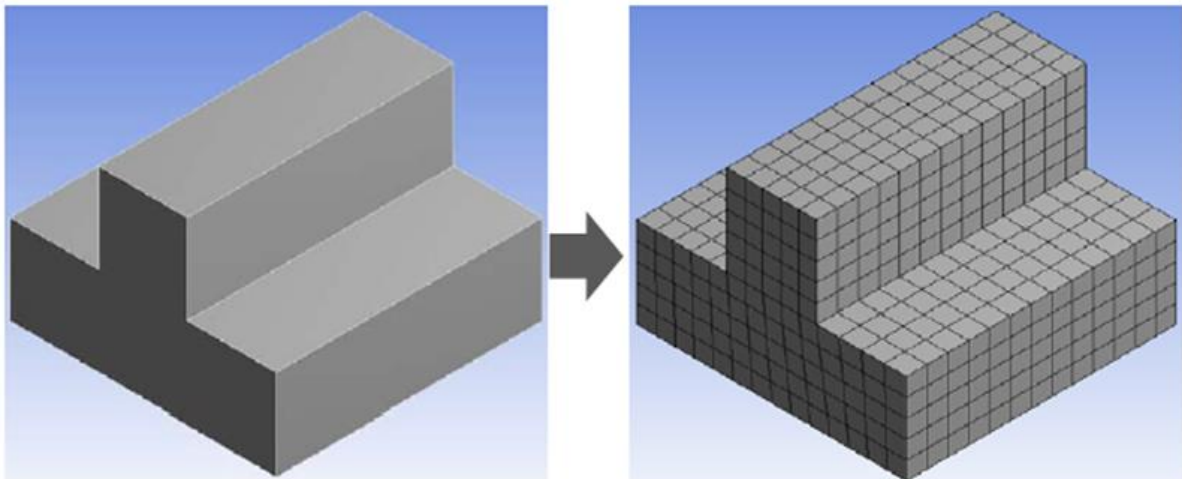


Figure 2.26 A finite element representation of a basic component shape [114].

2.4.2. Cellular Automata (CA)

Cellular Automata (CA) are algorithms that describe discrete spatial and/or temporal changes within various systems. These changes are enacted by applying transformation rules to a regular grid of cells, also known as a lattice [81]. This lattice is defined by a finite number of points, which can be associated with nodes in a finite difference field. The evolution of a CA transpires through the application of specific transformation rules (256 different rules according to Wolfram, 2002) that operate on the state (on/off) of each cell or node. These rules dictate a node's state based on its previous state and the states of its neighbouring cells or nodes. Generally, CA evolves in discrete time steps, with all cell or node states updated simultaneously after each time interval.

A basic representation of a two-dimensional CA involves an infinite set of cells and a set of defined transformation rules applied to each cell. Each cell can have two states: on (black) or off (white). The neighbourhood of a cell is the nearby or adjacent cells surrounding it. Common types of neighbourhoods include the von Neumann neighbourhood (four orthogonally adjacent cells) and the Moore neighbourhood (von Neumann neighbourhood plus four additional surrounding cells) as shown in Figure 2.27. The von Neumann neighbourhood consists of four cells orthogonally adjacent to the central cell, while the Moore neighbourhood includes those four and the four diagonally adjacent cells .

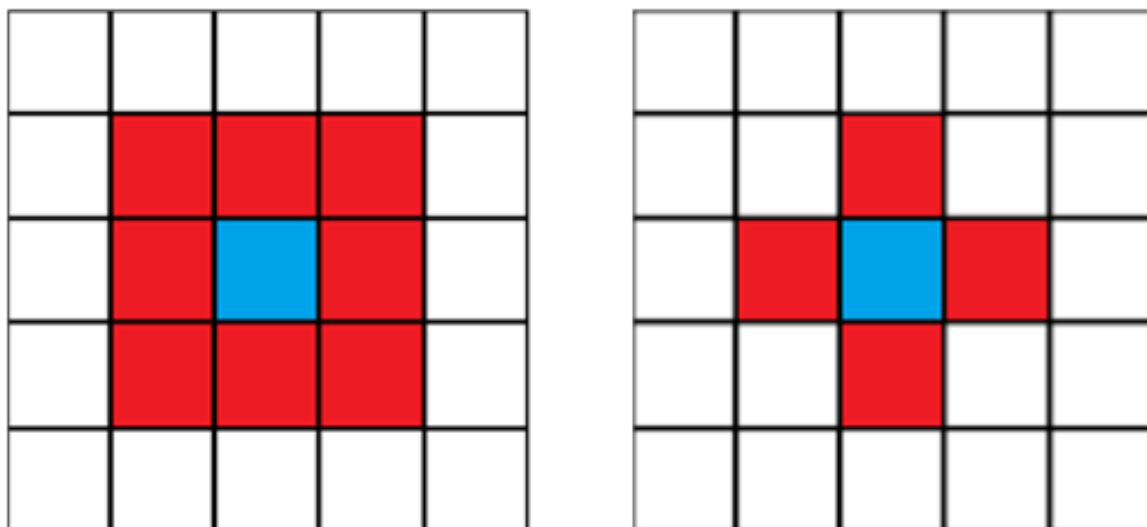


Figure 2.27 Moore and von Neumann neighbourhoods.

In generalized microstructure CA, a discrete spatial grid of cells or nodes is employed, and space can be defined using real space values. This defined space is usually uniform throughout the lattice, with the same transformation rule applied everywhere. Typically, each cell/node in the lattice starts with the same initial state value. Occasionally, the simulation might assume an initial periodic or random pattern (nucleation). These cells are then updated synchronously as time steps progress. As the CA simulation occurs on a finite lattice, in two dimensions, this lattice takes the form of a rectangle. However, this leads to the challenge of handling transformation rules for cells/nodes located at the lattice edges. The method chosen for handling these edge cells/nodes will impact the values of all cells in the lattice. One approach is to keep the edge cells/nodes constant throughout the algorithm. Alternatively, transformation rules for edge cell/node neighbours could be defined differently from those for other cells. The latter approach would result in fewer neighbours for edge cells/nodes. The choice of method depends on the specific problem being addressed in the local context.

2.4.3. Cellular Automata - Finite Element (CA-FE)

In the field of computational materials science, there is a significant surge in utilizing coupled modelling techniques such as CA-FE. The Cellular Automata - Finite Element (CA-FE) coupling is a computational modelling technique used in materials science and engineering to simulate microstructure evolution and other complex phenomena [98]. This coupling combines the strengths of two distinct computational methods, Cellular Automata (CA) and Finite Element (FE), to achieve accurate and efficient simulations of material behaviour. These couplings are applied to forecast the evolution of microstructures under specified conditions. The key advantage of employing these couplings lies in their enhanced computational efficiency and the capacity to incorporate multiscale models, within the same calculations.

It is important to note that the CA method within the CA-FE coupling does not capture the intricate development of dendritic or eutectic patterns as achieved by other methods. These other methods encompass factors like dendrite tip radius, micro-

segregation, secondary arms, etc. Instead, the CA method in this context concentrates on simulating grain growth using simplified kinetic laws, while the internal solid-liquid mixture is characterized by an internal volume fraction of solid. The CA-FE approach involves overlaying the FE mesh onto the CA lattice, as shown in

Figure 2.28. This overlay is implemented to more efficiently calculate and solve the conservation equations used at a larger scale in FEM than would be feasible within the finer-scale CA lattice.

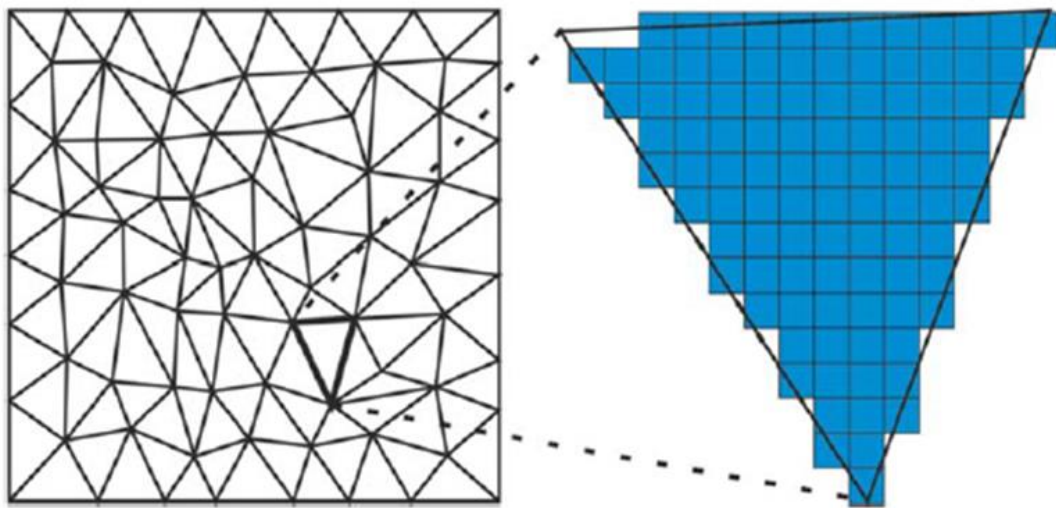


Figure 2.28 A schematic representation of a coupling between CA and FE grids [98].

Chapter 3 : Experimental Procedures

In this chapter, the methodology of this project will be discussed. The different shapes of lattices (such as different features, build angle, relative densities) will be detailed. Selective Laser Melting (SLM) manufacturing process will be used to fabricate Ti-6Al-4V specimens, and microstructures will be investigated by optical and Scanning Electron Microscopy. Mechanical behaviour will be assessed by compression testing. Finally, the numerical simulations of the project will be carried out by ANSYS 18.2 software.

3.1. Specification of AM Samples

The choice of lattice shapes was based on a systematic method that considered the most common shapes and features. The structures are detailed below, while the reasoning for the selection is discussed in more detail in the results chapters. These lattices were drawn and designed on one of three different software packages; Netfabb 2019 premium, Autodesk, CA, USA, and ANSYS 18.2 workbench, ANSYS, PA, USA were used for drawing the lattices, and Magics 21.1, Materialise, Leuven, Belgium was used to prepare the CAD file in .stl format. The base structure was a simple cube ($15 \times 15 \times 15 \text{ mm}^3$) which was then modified with different geometries of free space included inside it to assess the effect of the different features and characteristics.

Three different geometries were used to produce a hole inside the basic cube: a cuboid, a cylinder, and an elliptical cylinder. Three different sizes of the cuboid shape were used to make the hole, as shown in Figure 3.1, which are $5 \times 5 \times 15 \text{ mm}^3$, $10 \times 10 \times 15 \text{ mm}^3$, and $13 \times 13 \times 15 \text{ mm}^3$. While the diameter of the cylinder was 10 mm and the height was 15 mm, the ellipse shapes used two different diameters 7 and 13 mm with changing the direction

vertically and horizontally and 15 mm as height of the cylinder, as shown in Figure 3.2.

The same cuboid geometry that used before was used in the investigation of the build angle. The three different sizes of cuboids are used with three different build angles: 90° , 45° , and 20° from the x-y plane, as shown in Figure 3.1Figure 3.3Figure 3.4.



Figure 3.1 A front view of different sizes of square holes within a cube.

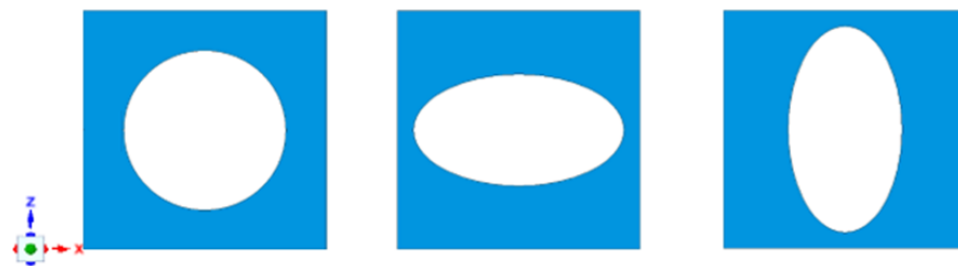


Figure 3.2 A front view of a cylinder and elliptical holes within a cube.



Figure 3.3 A front view of different sizes of cuboid holes within a cube with 45° angle.



Figure 3.4 A front view of different cuboid holes within a cube with 20° angle.

Table 3.1 A summary of the specification and pictures of the samples

	Label	Description	Hole size	Machine	X-Z Plane Picture
Group 1	Shape-S1-A90	Cuboid hole within a cube	5×5×15 mm ³	Renishaw SLM 400	
	Shape-S2-A90		10×10×15 mm ³		
	Shape-S3-A90		13×13×15 mm ³		
Group 2	Shape-C1	cylinder hole within a cube	D= 10 mm H= 15 mm		
	Shape-E1	Horizontal elliptical cylinder hole within a cube	D ₁ = 7mm D ₂ = 13 mm H= 15 mm		
	Shape-E2	Vertical elliptical cylinder hole within a cube	D ₁ = 13mm D ₂ = 7 mm H= 15 mm		
Group 3	Shape-S1-A45	Cuboid hole within a cube with 45° angle build angle	5×5×15 mm ³		
	Shape-S2-A45		10×10×15 mm ³		
	Shape-S3-A45		13×13×15 mm ³		
Group 4	Shape-S1-A20	Cuboid hole within a cube with 45° angle build angle	5×5×15 mm ³		
	Shape-S2-A20		10×10×15 mm ³		
	Shape-S3-A20		13×13×15 mm ³		

3.2. Renishaw Building

Firstly, the material used was Ti-6Al-4V powder grade 5 produced for Renishaw SLM 400 (Renishaw plc, Gloucestershire, U.K.) specification, the particle size range as provided by the supplier was between 15 to 45 μm and the composition is detailed in Table 3.2. The experiments were conducted on a Renishaw SLM 400 in the I-Form Advanced Manufacturing Research Centre at University College Dublin. The building platform size of the machine was $120 \times 120 \times 120 \text{ mm}^3$ with maximum height of 130 mm. The experiments were done under argon atmosphere on a titanium substrate. The layer thickness was 60 microns, the scanning parameters were exposure time, 50 μs , hatching space, 65 μm , and the laser power and point distance were 200 W and 75 μm . The scanning strategy was the meander hatching pattern for the samples.

Table 3.2 The chemical composition (wt%) of Ti-6Al-4V powder provided by the manufacturer.

Element	Ti	Al	V	Fe	O	C	N
Ti-6Al-4V	Bal.	5.5-6.5	3.5-4.5	0.25	0.13	0.08	0.03

3.3. Aconity Building

The Aconity Mini (Aconity3D, Herzogenrath, Germany) is another SLM machine used in this study to produce different samples. The experiment was conducted in the Royce Discovery Centre at the University of Sheffield. The building platform and powder feed plate were cylindrical with 140 mm diameter and builds were carried out under argon atmosphere on a titanium substrate. The machine is equipped with a 1070 nm wavelength laser with 80 μm spot size. The laser power and speed were 190 W and 1200 mm/s respectively with 30 μm as the powder layer thickness. The hatch space was 70 μm and the laser rotated 90° per layer, with a 45° starting offset.

3.4. Micropreparation

All the metallographic processes of the samples were done in the micropreparation laboratory in the Materials Science and Engineering Department at the University of Sheffield. At the beginning, the samples were cut to halves by Struers Secotom-50 machine. Next, the samples were perpendicularly mounted in a conductive Bakelite in SimpliMet 3000 automatic mounting press which runs a cycle of 6 minutes (2 mins heating and 4 mins cooling) under 290 bar pressure. Finally, all the samples were placed on Buehler EcoMet 250 for grinding and polishing. The process was beginning with grinding by different sizes of silicon carbide pad (800, 1200, and 2500), then a polishing part with two different suspensions (1 μm diamond and silica suspension).

3.5. Post Processing (Heat Treatment)

Some samples were heat treated to effect microstructural change and allow a comparison between the “as-built” samples and the “heat treated” form. The heat treatment profile was carried out under a high vacuum atmosphere with heating rate of $10^{\circ}\text{C}/\text{min}$ to 1050°C for 2 hours followed by furnace cooling. This process was aiming to take the samples above the β transus temperature ($\approx 882^{\circ}\text{C}$) to allow transformation of the typical as-built microstructure of SLM-made elements which is columnar β .

3.6. Measurements

3.6.1. Optical Microscopy

The microscopical observations were carried out in a Nikon eclipse LV150 microscope using polarized light (PL) because titanium alloys show contrast under this imaging mode. The microscope is fitted with Buehler Omnimet 9.5 software. The micrographs were taken at different magnifications 5, 10, and $20\times$.

3.6.2. Electron Backscatter Diffraction (EBSD)

The crystallographic examinations were conducted in JEOL 7900F (JEOL Ltd, Tokyo, Japan). The machine was equipped with an advance EBSD system called Oxford Instruments HKL (Oxford Instruments HKL, Hobro, Denmark). During the data acquisition, the step size was 1 μ m and the accelerating voltage was 20kV. The specimens were tilted for 70° and the working distance was 13mm. The workplace during the mapping acquisitions was in parallel plane to the build direction. The data analysis done using Oxford Instruments' software packages such as AZtecCrystal and Channel 5 (Mambo).

3.6.3. Surface Roughness

Surface roughness is a critical parameter that characterizes the texture or irregularities on a surface. There are several methods for measuring surface roughness, and the most common parameters used to quantify it are Ra (Arithmetic Mean Roughness), Rq (Root Mean Square Roughness), and Rz (Maximum Height Roughness). These parameters are defined based on the deviation of the surface profile from its mean line.

3.7. Compression Test

All compression tests were done on a Zwick Roell Z050 testing machine. All tests were carried out under the same conditions with an initial strain rate of 10⁻⁴s⁻¹, at room temperature. The machine recorded the applied force on the samples and the displacement of the crosshead. Firstly, compliance correction of the results is performed, using data obtained by running the experiment in a plate-to-plate configuration (i.e. carrying out the compressive loading without a sample present), up to limited values of force, reflecting the loads used in the tests. These data were used to correct the displacement data recorded in other tests because the elastic deformation of the machine itself also contributes to the displacement seen by the crosshead. The force-displacement data from the plate-to-plate test was used to remove this displacement from the crosshead data, leaving just the change in dimension of the samples.

The data were collected from the machine in Microsoft Excel file format. The data was in standard force vs standard travel distance. Some calculations with the following equations were used to produce the initial charts.

Engineering strain was calculated by:

$$\varepsilon = \Delta l / l \quad (1)$$

where: ε = strain, Δl = deformation, l = original length.

Engineering stress was calculated by:

$$\sigma = F / A \quad (2)$$

where: σ = stress, F = force, A = original area.

Most samples showed an initial region where the load increases non-linearly with strain. This can occur in compression when the contact with the sample is not established simultaneously across the specimen [116]. During the data analysis process, the stress-strain were corrected by identifying the real zero strain position as that where the projection of the linear part of the curve would meet the x-axis, to accurately determine the strain values. Finally, the Young's modulus and yield strength were calculated from the new curves.

3.8. Finite Elements Method (FEM)

For finite element analysis, ANSYS 18.2 software was used to simulate all geometries and structures. In the beginning, the specifications of the material were modified, as shown in Table 3.3, to be approximated to the material properties that were used in the experiments. Then, To understand the behaviour of anisotropic Ti-6Al-4V with α and β phases, three different material properties of Ti-6Al-4V were used separately on the cube model: 1) a cube with an isotropic Young's modulus 114 GPa, 2) two cubes with different stiffness matrices are used to simulate the two different phases α and β of Ti-6Al-4V alloy,

as shown in Table 3.4. The properties of the material were, for the initial modelling, assumed to be isotropic and uniform. The results were limited on local von mises stress and effective strain.

Table 3.3 The properties values of Ti-6Al-4V alloy that used in ANSYS [5].

Property	Density (kg/m ³)	Young's Modulus (GPa)	Tensile Yield Strength (MPa)	Compressive Yield Strength (MPa)	Tensile Ultimate Strength (MPa)
Ti-6Al-4V	4430	114	880	970	950

Table 3.4 Stiffness coefficient of α and β phases of Ti-6Al-4V (GPa) [117, 118].

Phase	C ₁₁	C ₁₂	C ₁₃	C ₃₃	C ₄₄
α -Ti6Al4V	168	95	69	191	48
β -Ti6Al4V	134	110	-	-	55

3.8.1. Setup of Model Boundary Conditions and Validation

In order to represent the real structure of lattices, specific boundary conditions were applied, intended to make the simulation close to the actual experiments. The boundary conditions that are used in the ANSYS simulation are 1) two centre lines on the bottom surface, forming a plus sign “+” structure and 2) relative positions and orientations of the structure are fixed in the x and z directions while allowing their lengths to change. The same conditions are used in the literature [77] for modelling of this kind as are used in this project, with some modifications to fit with the required structures. These conditions, as shown in Figure 5.1, are: 1) the displacement on the top surface represents the applied strain, which is set as a value of -1.5×10^{-3} in the y-direction, as an arbitrary strain level consistent with elastic deformation, 2) the two centre lines on the bottom surface are both constrained in

the y-direction, but are free to extend along their length (line A is free in z and line B is free in x), and 3) the bottom surface is constrained in the y-direction but is free in both x and z directions to allow the shape to expand. A test was run with a simple cube, set to have the properties of standard Ti6Al4V, and the result of equivalent (von Mises) stress under this strain condition was 171 MPa, as shown in Figure 3.6, which shows a uniform stress distribution (which would be expected for a solid object, stress concentrations would indicate problems with the constraint applied by the boundary conditions) and this gives a Young's modulus of 114 GPa, agreeing with the input material properties. This provides a basic validation of the material property set input and the implementation of basic compressive elastic deformation in the model.

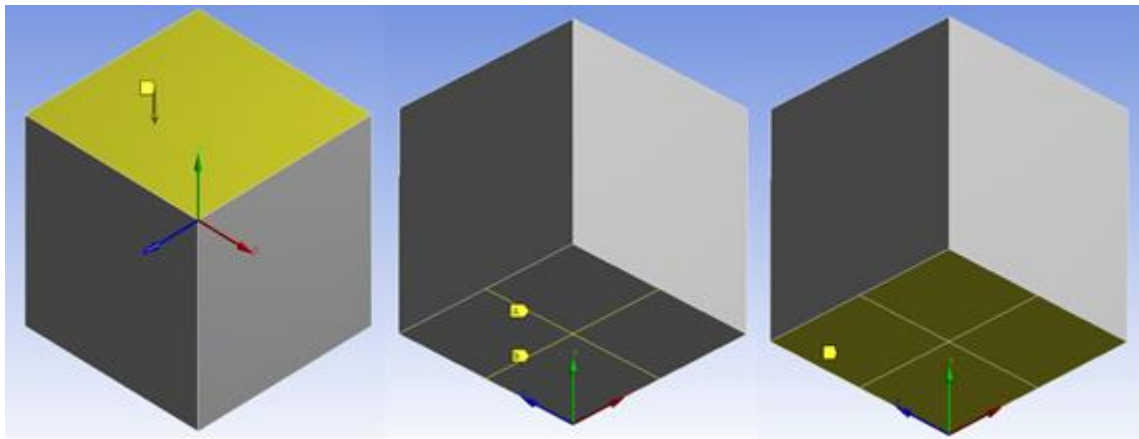


Figure 3.5 A finite element model of a solid cube unit cell showing the boundary conditions that are applied on the cube.

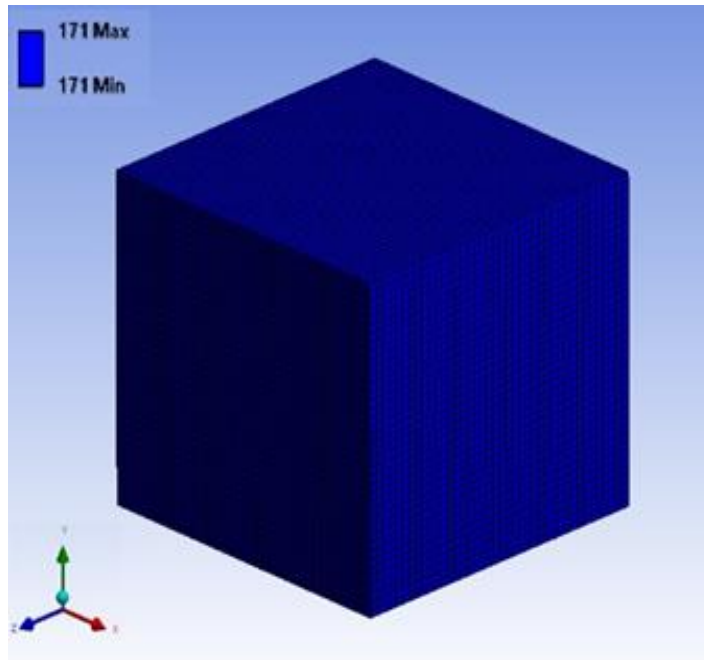


Figure 3.6 The von Mises stress results of the cube unit cell under compression to a strain of -1.5×10^{-3} , the blue colour represents the even stress inside the cube.

Chapter 4 : The Effect of Component Shape on AM Ti6Al4V Microstructure

In Ti-6Al-4V alloys produced by AM processes, it is known that the mechanical properties depend greatly on α' colony size and the texture [14]. As it influences aspects such as the thermal input and flow during the build, the geometry of the part being made is a key factor to determine both the grain structure and the texture. Many different geometrical features are present in lattices, which can have a complex design, and it is very challenging to completely describe the variations in such a part. Therefore, to have a better understanding of the influence of part shape on microstructure that could be applied to a general case, and to be able to set out a defined number of experiments towards this, simplified shapes capturing aspects of shape change were defined. These shapes captured three main features: 1) changing thickness, 2) different curvature, and 3) different inclination of build angle. All samples were designed to contain one of these features or more, to achieve an efficient build where all of these could be explored.

In this chapter, firstly, the effect of build geometry (through parts containing cylindrical and elliptical cylindrical holes) on SLM Ti6Al4V as-built microstructure will be investigated. Then, the effect of build angle on SLM Ti6Al4V as-built microstructure will be studied. Finally, the crystallographic textures of these factors (build geometry and build angle) will be explored.

4.1. The Effect of Build Geometry on AM Ti6Al4V Microstructure

The microstructure of Ti-6Al-4V alloy is initially β phase but is transformed into $\alpha + \beta$ phase because, during the build process, the alloy is first above the β transus temperature (above 882°C) [4], and then cools to below this. However, the amount of retained β phase depends on the cooling rate. In this project and during the SLM process in general, the

cooling rate is very high (thousands of degrees per second) [119] and this leads to a fully martensitic α' microstructure. To evaluate the effect of the different features of the part (curvature, thickness, and build angle) on the microstructure of SLM Ti-6Al-4V samples, various factors such as surface roughness, grain width and orientation, pore size, and near edge area size (as the microstructure near and edge is identifiably different to the bulk) have been assessed for all different EBSD images.

4.1.1. The cylindrical Hole Samples (Shape-C1)

The microstructure of the cylindrical sample, as shown Figure 4.1, Figure 4.2, and Figure 4.3, is fully α' martensitic laths, as expected [4, 119], and they are located within the boundary of prior β grains that formed after solidification. The grains' growth direction is vertically with the build direction, and this is related to the nature of the AM process where the prior β grows in a columnar path through several layers, in the direction in which further material is added, and in the opposite direction to the greatest thermal gradient (where the thermal energy will be extracted through the base plate). The average width of the prior β grains is $90 \pm 6 \mu\text{m}$ which approximately corresponds to the hatch spacing of the process ($65 \mu\text{m}$). The end of each layer has high thermal gradient due to unheated particles next to them, and this caused equiaxed $\alpha + \beta$ grains to form near to the edge (i.e. nucleation of new grains rather than growth on the pre-existing grains of the layer below, which leads to the columnar structures); this region's width is $225 \pm 5 \mu\text{m}$. Where there are internal spaces in the parts, the inner surface roughness of the sample has been measured from EBSD images, where possible, being between $120 - 150 \mu\text{m}$, as shown in Figure 4.1 and Figure 4.2. This occurs because of the melting of some powder particles and solidification near the inner edge of the sample, and is also reported by Antonysamy et al. 2013 who further suggested the inner areas suffer from the incorporation of unmelted particles [120].

The optical microscope image, as shown in Figure 4.4, showed the arrangement of α' martensitic laths within the boundaries of β grains. There were a number of the laths which seemed to continue over the grain boundaries of β , which could be related to the nucleation

of α' grains which originate from β grain boundaries. The arrangement of α' martensitic laths is mainly inclined at 90° and 45° to the build direction which is similar to the observations reported by Facchini et al. (2010) [121] and Sercombe et al. (2008) [122]. This will be due to the orientation relationship between the α' martensitic laths and the prior β grains they transform from, with the orientation of the β grains being determined by the preferred growth direction.

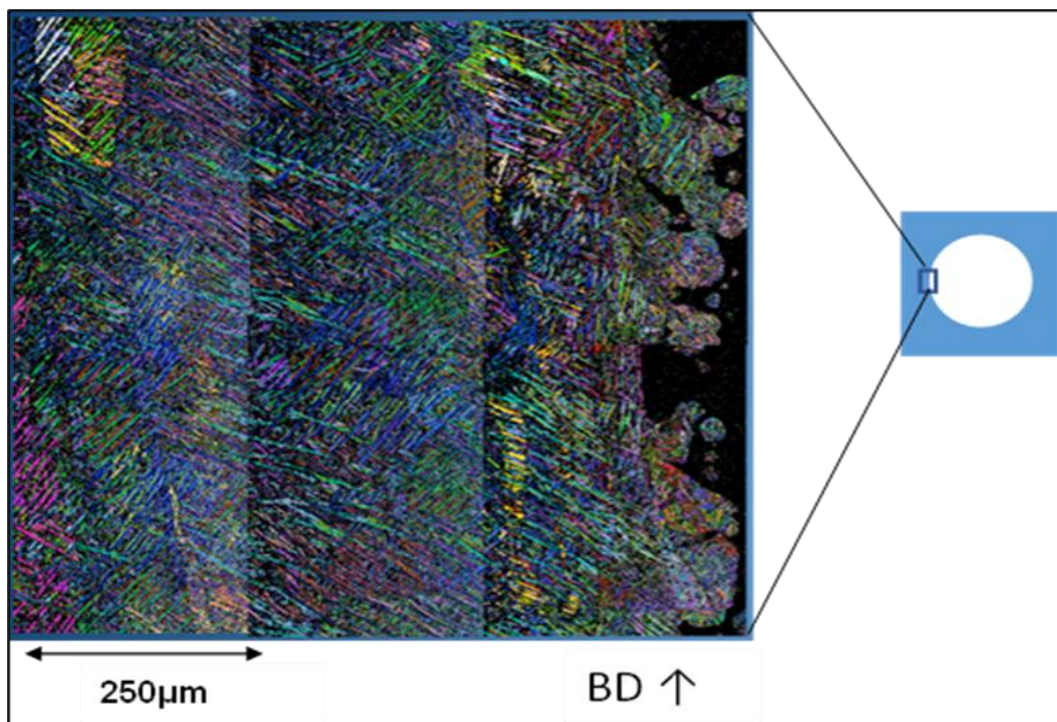


Figure 4.1 An SEM EBSD micrograph showing part of an as built AM Ti6Al4V component created to explore the variation in microstructure with component geometry, consisting of a cube with a cylindrical hole, with the image taken from the area indicated.

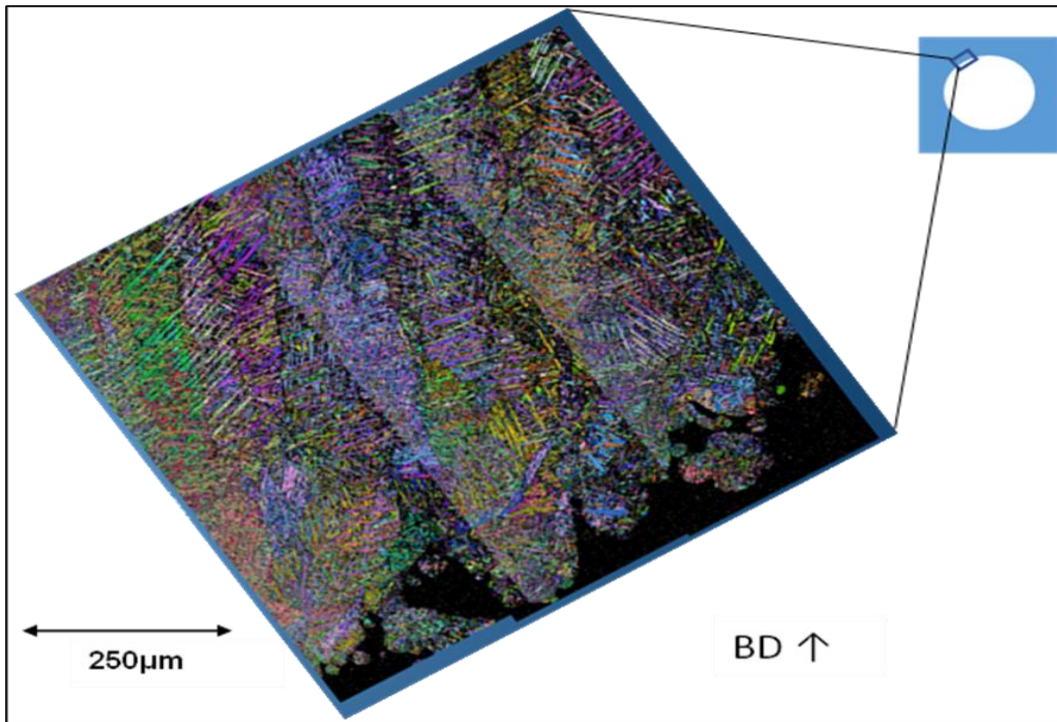


Figure 4.2 An SEM EBSD micrograph showing part of an as built AM Ti6Al4V component created to explore the variation in microstructure with component geometry, consisting of a cube with a cylindrical hole, with the image taken from the area indicated.

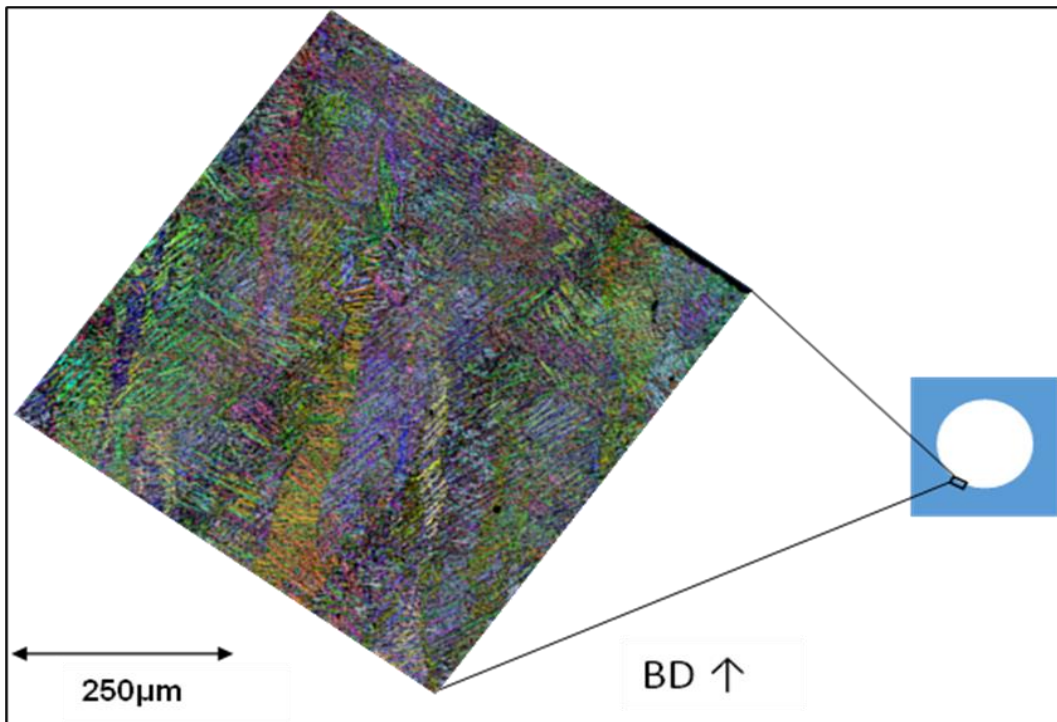


Figure 4.3 An SEM EBSD micrograph showing part of an as built AM Ti6Al4V component created to explore the variation in microstructure with component geometry, consisting of a cube with a cylindrical hole, with the image taken from the area indicated.

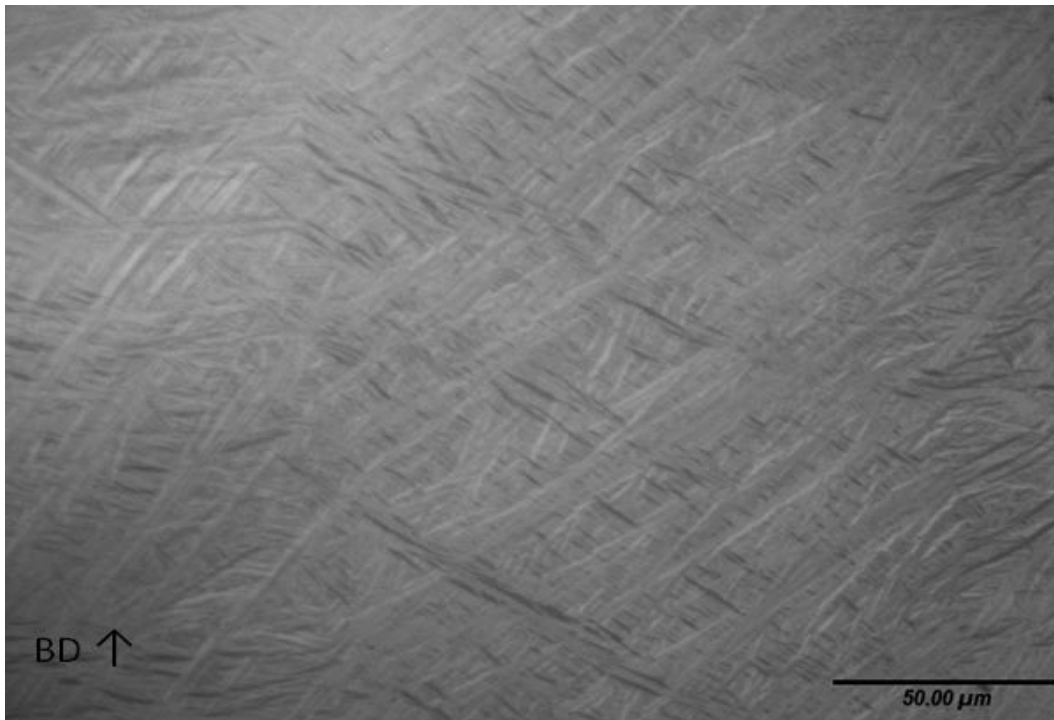


Figure 4.4 An optical micrograph showing part of an as built AM Ti6Al4V component created to explore the variation in microstructure with component geometry, consisting of a cube with a cylindrical hole.

4.1.2. Elliptical Cylindrical Hole Samples (Shape-E1 and Shape-E2)

These samples will be divided into two sets depending on how the long diameter of the ellipse was oriented relative to the vertical build direction: 1) Horizontal elliptical cylindrical hole “shape-E1” (producing a wider overhang, with more rapidly changing profile of the hole with height), and 2) Vertical elliptical cylindrical hole “shape-E2” (where the profile of the hole changes less rapidly with build height), and each set will be discussed separately to focus on differences of the microstructures in various spots.

4.1.2.1. Shape-E1 Samples

Firstly, the EBSD maps taken from the horizontal elliptical cylindrical hole sample, are shown in Figure 4.5, Figure 4.6, and Figure 4.7. These were taken from three different places to investigate the effect of a curved surface at a high angle to the build direction on the growth of the columnar β grains. The columnar grains of β are seen to grow in the build direction (BD), as expected, and continue to grow through a number of layers in the build.

Due to the cooling to room temperature after building, α' martensitic laths form within the prior β . As consequence of the shape requirements of this sample geometry, the inner surface finish has been affected to have a “wavy” form, because of the variation of grain heights as shown in Figure 4.5. There are a few differences observable between the bottom and upper areas of the sample, which will now be discussed.

In the bottom area, the surface roughness covers a zone of around $40\ \mu\text{m}$ width and there is no appearance of equiaxed $\alpha + \beta$ grains near to the edge. However, in the upper area (Figure 4.6), the equiaxed $\alpha + \beta$ grains near to the edge are clear to seen in a band with a width around $175\ \mu\text{m}$ and surface roughness of about $85\ \mu\text{m}$. These differences could arise from differences in the thermal gradient at the melt pool and how it is built up layer by layer. On the lower side of the hole, where the layer-by-layer build terminates, it is clearly not possible to create new grains above the final layer and if this grows on the crystal of the layer below it has a high chance to retain a preferred orientation. On the upper side of the hole however, the laser path will first move over and melt powder on top of powder particles, and the initial solidification will not have an oriented solid to nucleate on, or as strong thermal gradient (due to the lower thermal conductivity of the powder), to encourage directional solidification and growth. These first few layers will therefore be equiaxed $\alpha + \beta$ grains before a preferred growth orientation is established and columnar grains of β grow on that base of equiaxed grains. There are a few pores appearing in the upper side of the sample, as shown in Figure 4.6, the average size of these pores is $352 \pm 48\ \mu\text{m}^2$. As these pores are remote from the surface, they are probably not due to surface effects and could be related to gas entrapment [123]. This can rise from gas trapped between, or even contained within, the powder in the melting pool and these pores are common in AM samples [123, 124].

The middle area, as shown in Figure 4.7 and Figure 4.8, is the thinnest area in the sample with a nominal width of $1\ \text{mm}$, and it is clear that in this area the columnar β grains disappeared, leaving in the observed areas, only three large grains in the middle with average width $247 \pm 45\ \mu\text{m}$, where laths of α' have formed over the prior β grains. This

confirms that these laths originate from two different points during the martensitic transition from the parent β grain [119].

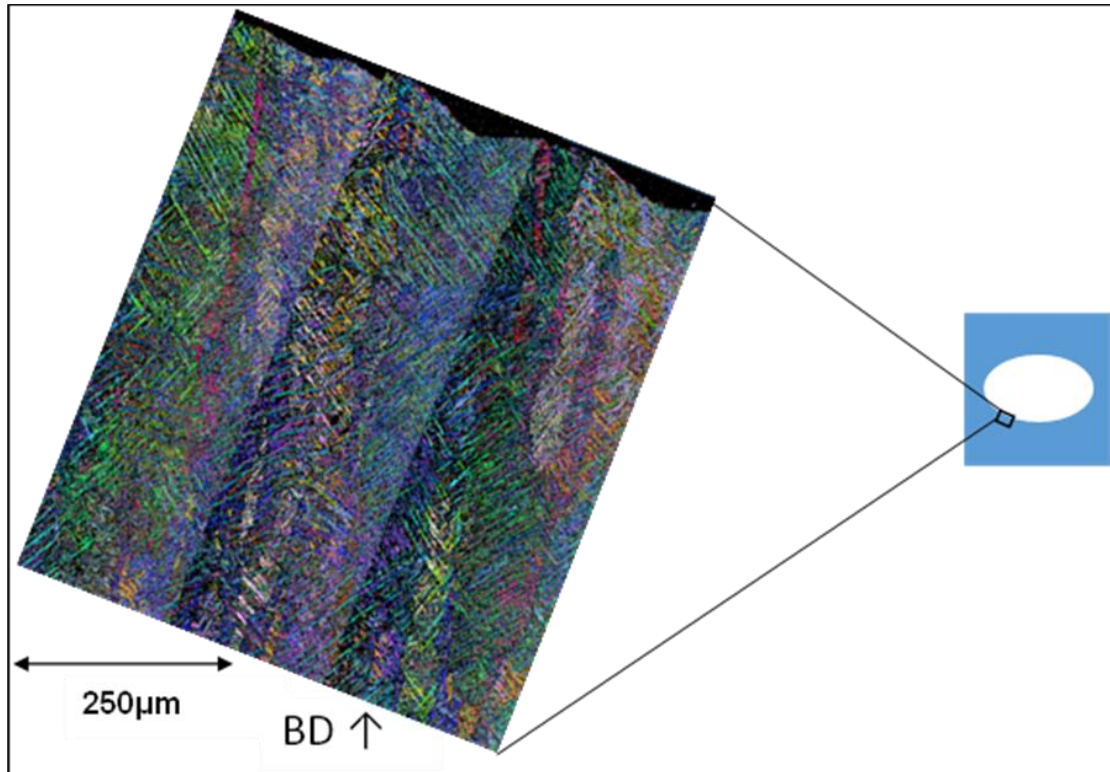


Figure 4.5 An SEM EBSD micrograph showing part of an as built AM Ti6Al4V component created to explore the variation in microstructure with component geometry, consisting of a cube with an elliptical cylindrical hole, with the image taken from the area indicated.

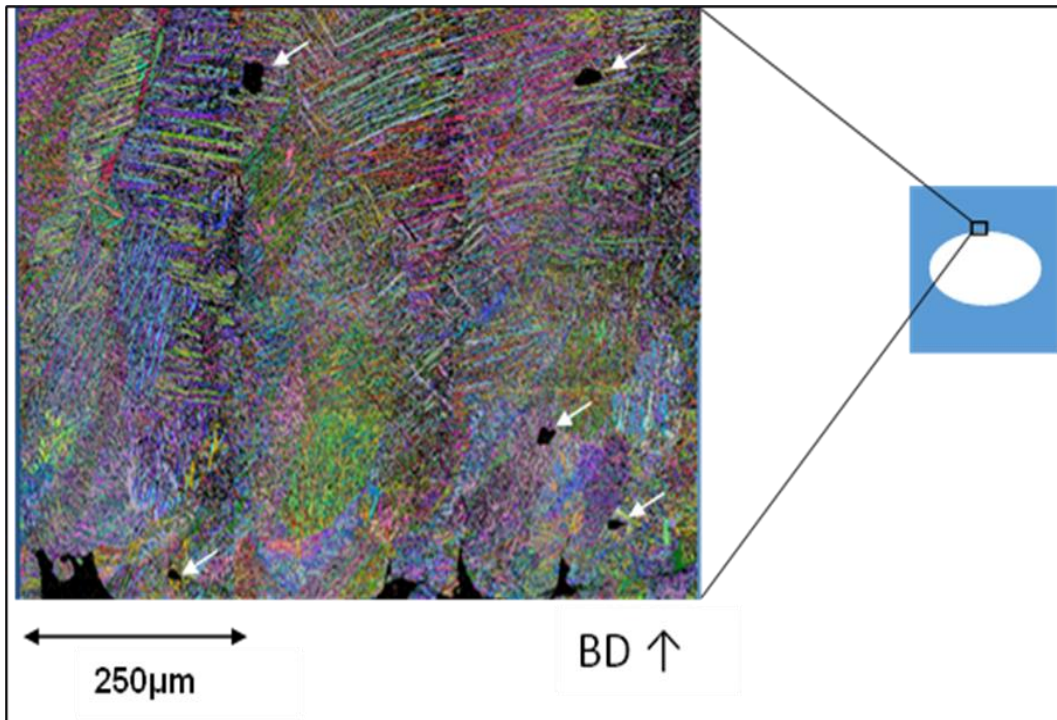


Figure 4.6 An SEM EBSD micrograph showing part of an as built AM Ti6Al4V component created to explore the variation in microstructure with component geometry, consisting of a cube with an elliptical cylindrical hole, with the image taken from the area indicated.

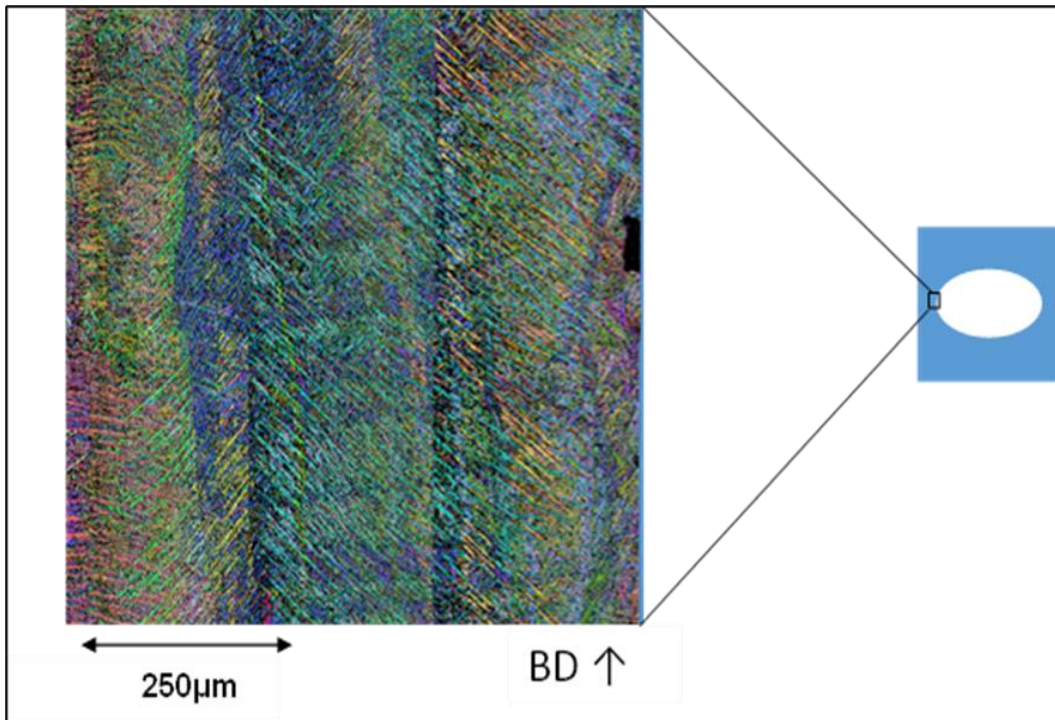


Figure 4.7 An SEM EBSD micrograph showing part of an as built AM Ti6Al4V component created to explore the variation in microstructure with component geometry, consisting of a cube with an elliptical cylindrical hole, with the image taken from the area indicated.

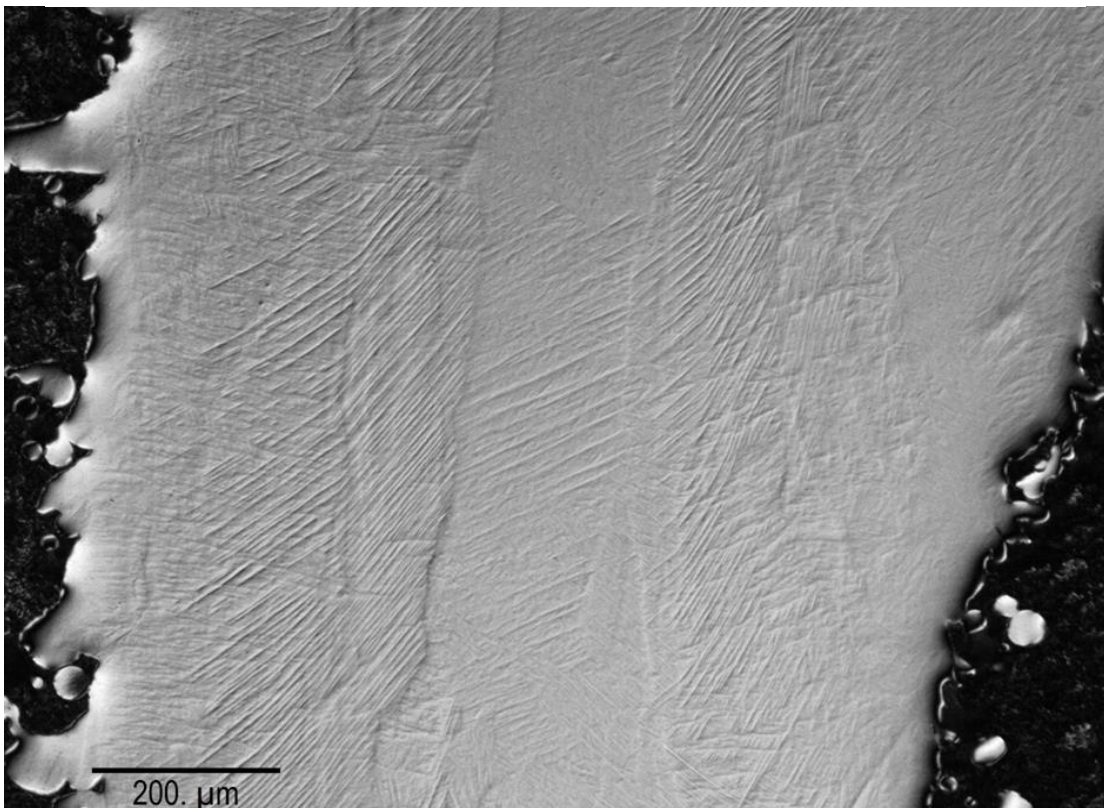


Figure 4.8 An optical micrograph showing part of an as built AM Ti6Al4V component created to explore the variation in microstructure with component geometry, consisting of a cube with an elliptical cylindrical hole.

4.1.2.2. Shape-E2 samples

The shape-E2 was rotated from having the longer radius in the horizontal direction to this being vertical, in order to study the effect of a curved surface at a lower angle to the build direction. The microstructure, as shown in Figure 4.9Figure 4.10Figure 4.11 Figure 4.12, has a number of differences from other samples, that are related to the geometry and its relationship to the build direction. The main difference is that the columnar β grains are clearly growing inclined approximately 45° away from the build direction, as shown in Figure 4.9. The inclination of the β grains is clear in the EBSD map, however, the EBSD map covered only $300\ \mu\text{m}$ from the edge downwards and the base's thickness is $1\ \text{mm}$, therefore, no information is available on whether this inclination of the grains commenced after a certain distance from the base, perhaps close to the free surface, or if it was present at the beginning. Simonelli et al. (2014) assumed that the thermal gradients during the building process have an influence on the growth of β grains, and that if the gradients are inclined (as might result from the movement of the beam across the surface) this could cause them to incline away from the typical direction. However, the other images from the middle, bulk and top corner in this sample, Figure 4.10Figure 4.11Figure 4.12, showed typical growth direction of β columnar grains which is upwards with the build direction, and there is no inclination in the maps and the other samples (shape-C1 and shape-E1) have no evidence of inclination despite using the same building process with the same scan strategy. It is therefore not certain what caused this specific observation, but it could be an isolated case over a small volume of material.

Another feature worth noting is the inner surface roughness. The surface was smooth and wavy in shape-E1 sample. In the shape-E2 sample however, the surface roughness is $100\ \mu\text{m}$ and it is rougher than shape-E1 sample ($85\ \mu\text{m}$). This could be related to the geometry and different curvature, as this would lead to a different frequency of the lay to layer "steps" being encountered on the surface, adding to the roughness. It could also lead to the size of the near edge area to be determined to be an average of $75 \pm 25\ \mu\text{m}$. In the EBSD map of the bulk area, as shown in Figure 4.12, the microstructure was clearly

organised and α' martensitic laths within the prior β have consistent inclination of 90° and 45° to the build direction [121, 122]. By contrast, randomisation of α' laths is seen in the near edge areas where they are varying in length and direction due to the transformation from $\alpha + \beta$ phase and heat transfer because of the position between melted and unmelted powder particles.

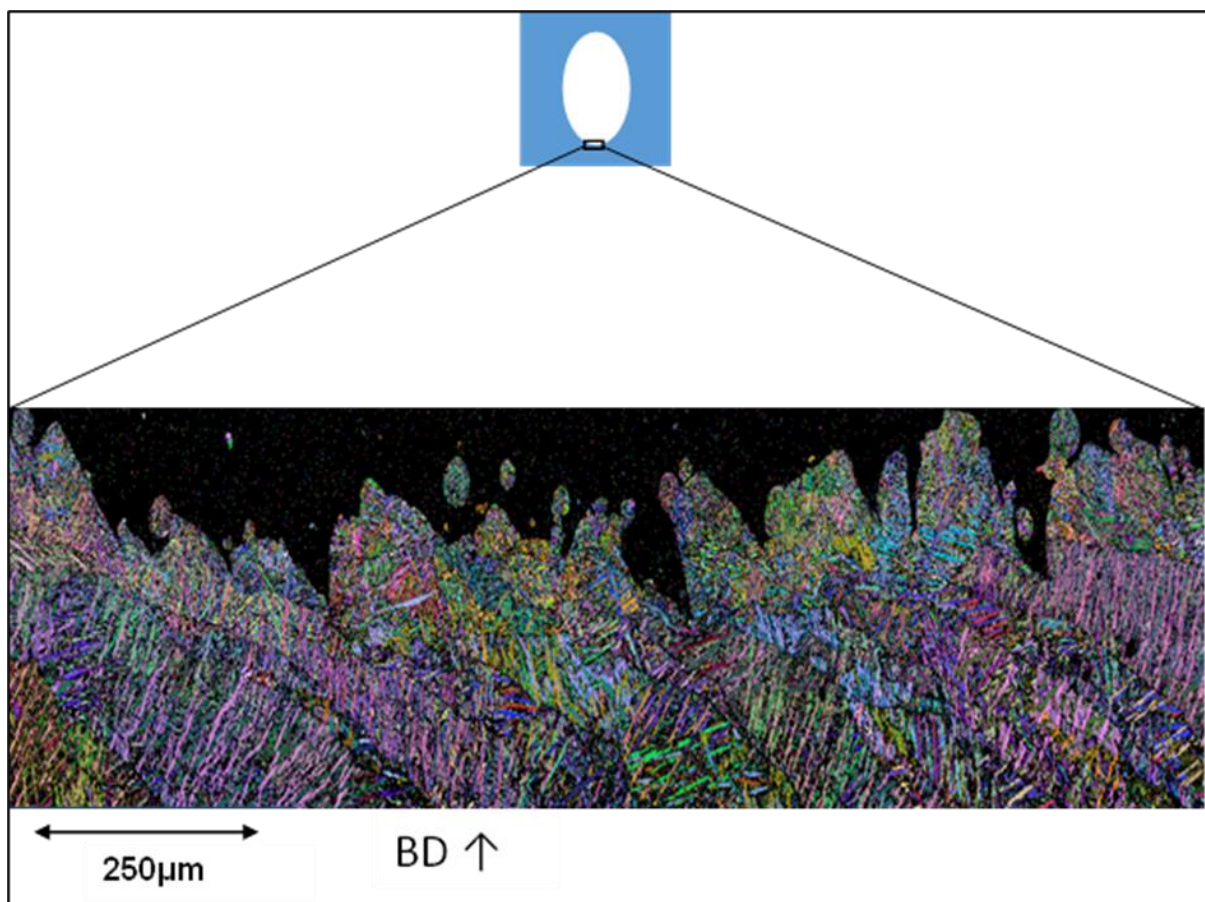


Figure 4.9 An SEM EBSD micrograph showing part of an as built AM Ti6Al4V component created to explore the variation in microstructure with component geometry, consisting of a cube with an elliptical cylindrical hole, with the image taken from the area indicated.

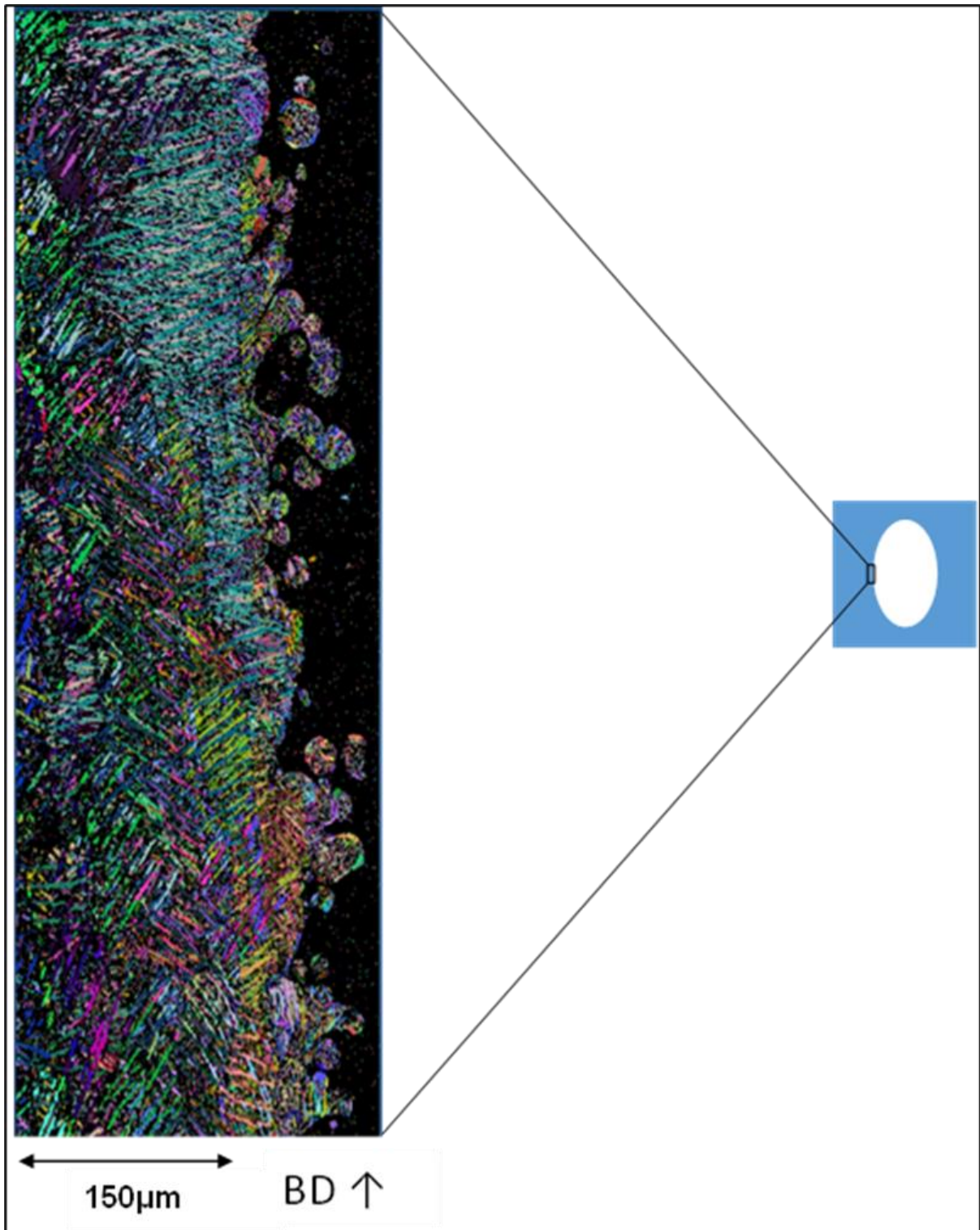


Figure 4.10 An SEM EBSD micrograph showing part of an as built AM Ti6Al4V component created to explore the variation in microstructure with component geometry, consisting of a cube with an elliptical cylindrical hole, with the image taken from the area indicated.

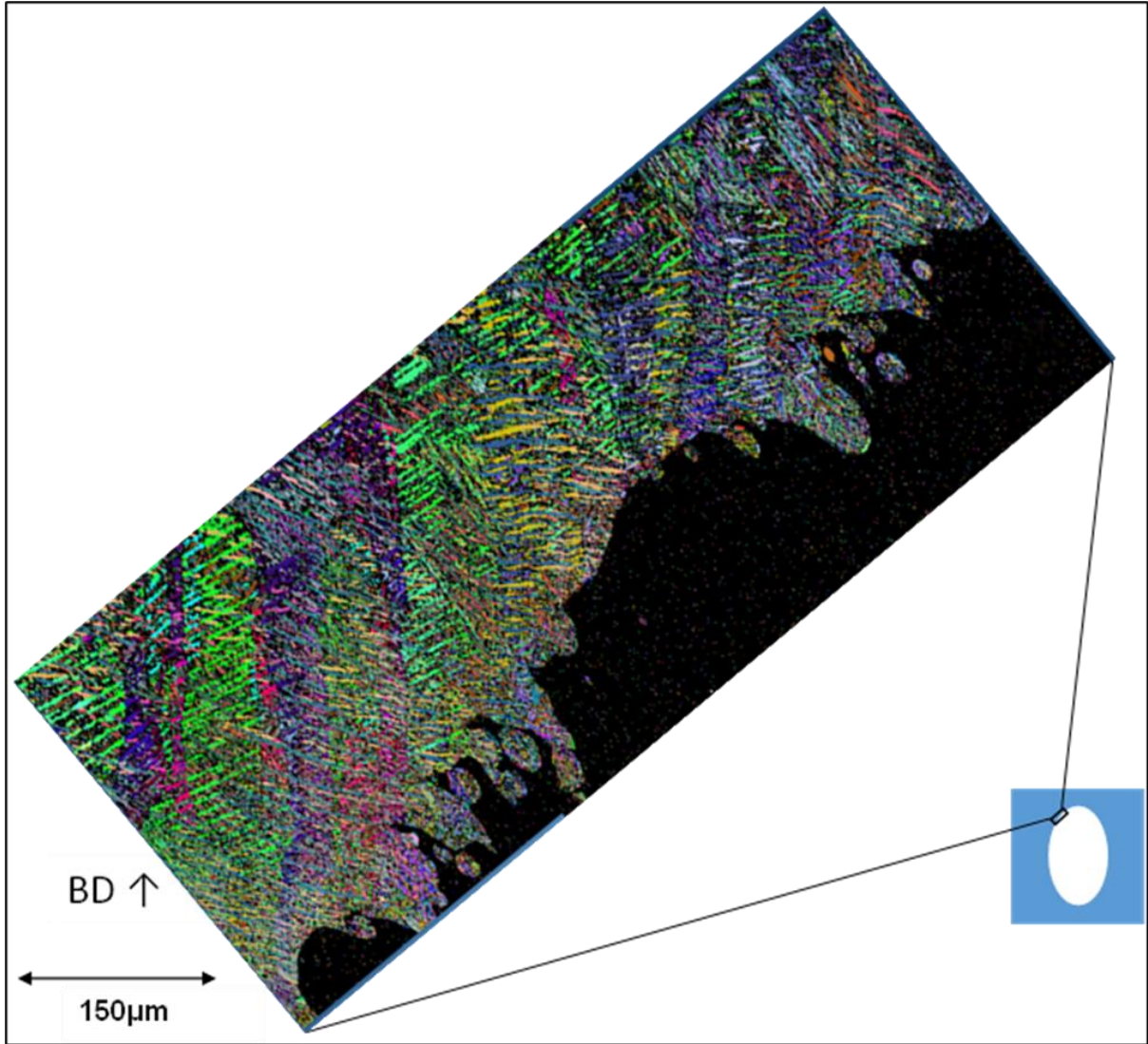


Figure 4.11 An SEM EBSD micrograph showing part of an as built AM Ti6Al4V component created to explore the variation in microstructure with component geometry, consisting of a cube with an elliptical cylindrical hole, with the image taken from the area indicated.

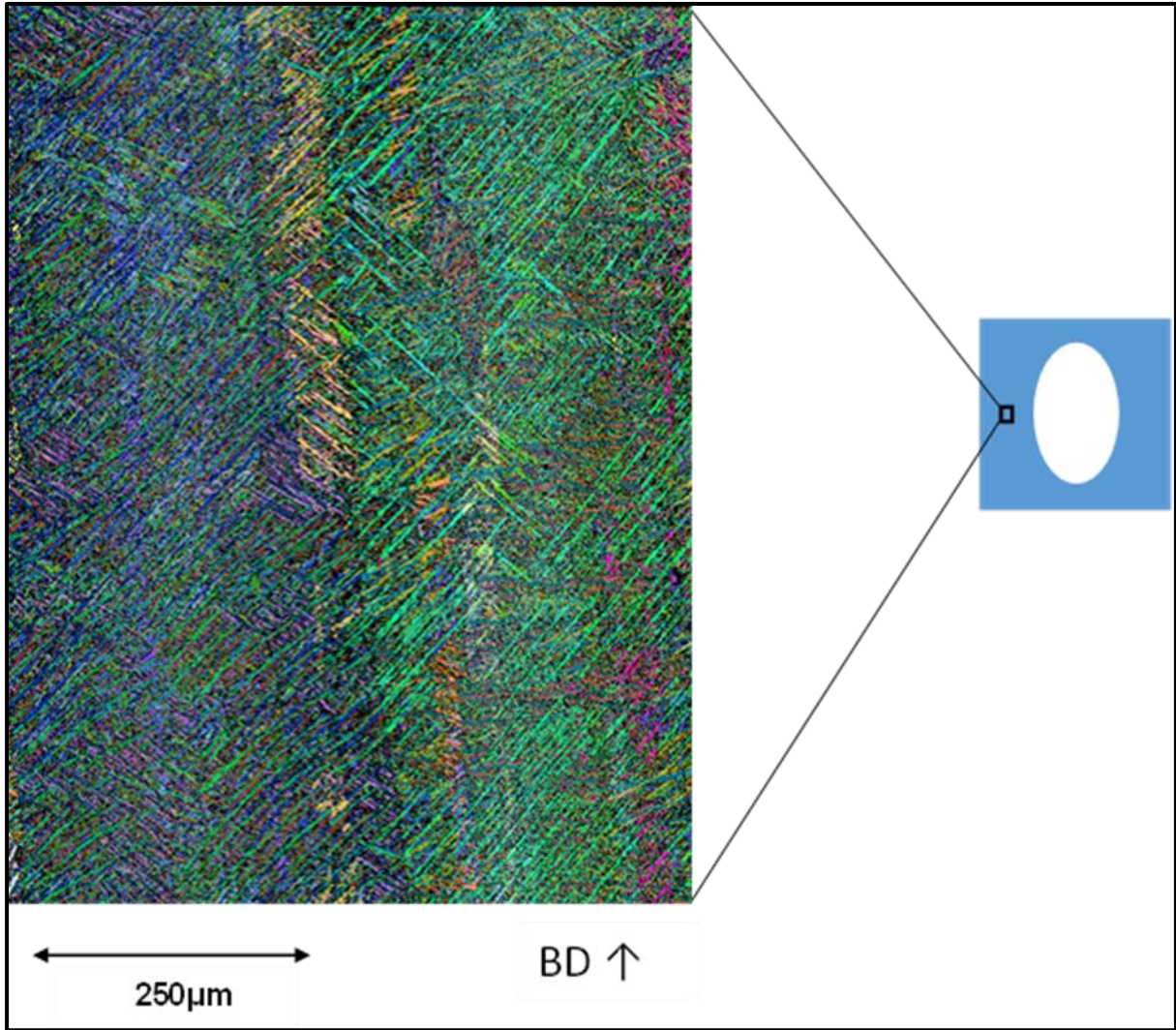


Figure 4.12 An SEM EBSD micrograph showing part of an as built AM Ti6Al4V component created to explore the variation in microstructure with component geometry, consisting of a cube with an elliptical cylindrical hole, with the image taken from the area indicated.

4.2. The Effect of Build Angle on AM Ti6Al4V Microstructure

Three samples were manufactured with side walls tilted at 0°, 45°, and 70° away from the build direction (effectively producing a parallelepiped sample, with a hole through the centre of the same shape), to investigate the effect of the build inclination on the deposition through the layers of powder. The EBSD maps were taken from certain places to make the comparison between the microstructures that result from different build angles. The first sample with 0°, as shown in Figure 4.13, Figure 4.14, and Figure 4.15, showed the normal microstructure with columnar β grains that grow in the build direction. It is obvious from the maps that three different pores are spread in different areas around the sample with different sizes (360 μm^2 , 250 μm^2 , and 860 μm^2). The appearance of porosity in Ti6Al4V lattices produced by SLM is a common feature and it can be reduced by heat treatment or Hot Isostatic Pressing (which was not performed in this experiment). The grains size was of average size between 60 μm and 90 μm , and there are equiaxed grains near to the inner edge of the upper half, as shown in Figure 4.15. These grains probably nucleated on partially melted powder and continued for 350 μm upwards until the columnar grains established. Figure 4.16 and Figure 4.17 show the second sample, with walls at an inclined angle of 45°. The growth of columnar β grains continued vertically upwards in the build direction, and it can be seen clearly in Figure 4.16 that there is continuity of the growth irrespective of the structure inclination. Figure 4.17 shows the inner edge of the sample; the grains near to the edge appear to nucleate on the inclined surface originally, then the columnar grains start to grow in the build direction through a number of layers. Figure 4.18 and Figure 4.19 relate to the final sample built with walls included 70° away from the build direction. The EBSD images were taken from only two places because of the poor index obtained from this sample. These images showed that the growth of the columnar β grains continued vertically upwards to the build direction despite the sharp inclination, and above equiaxed grains which formed near the edge of the structure. It is noted from Figure 4.19 that the width of the columnar grains reduced to be around 60 μm and this seemed to be related to the rapid nucleation on the edge. The powder particles that appeared in the EBSD image could be related to the preparation process and while polishing these particles gathered in the corner.

The three different structures have revealed that the structure inclination in components of the dimensions explored here has a very small effect on the microstructure. Where this takes place, it occurred in certain areas such as near to the edge for the inner side of the sample where the equiaxed grains nucleate. The thermal gradient therefore has a stronger effect on the growth direction than the structure complexity. While the contour passes, the layer solidifies in the melt pool towards the preferred direction $\langle 001 \rangle_{\beta}$ because of the laser path. After a number of layers, this direction will be the stronger and any new layer has weak texture, and it will follow the preferred direction $\langle 001 \rangle_{\beta}$.

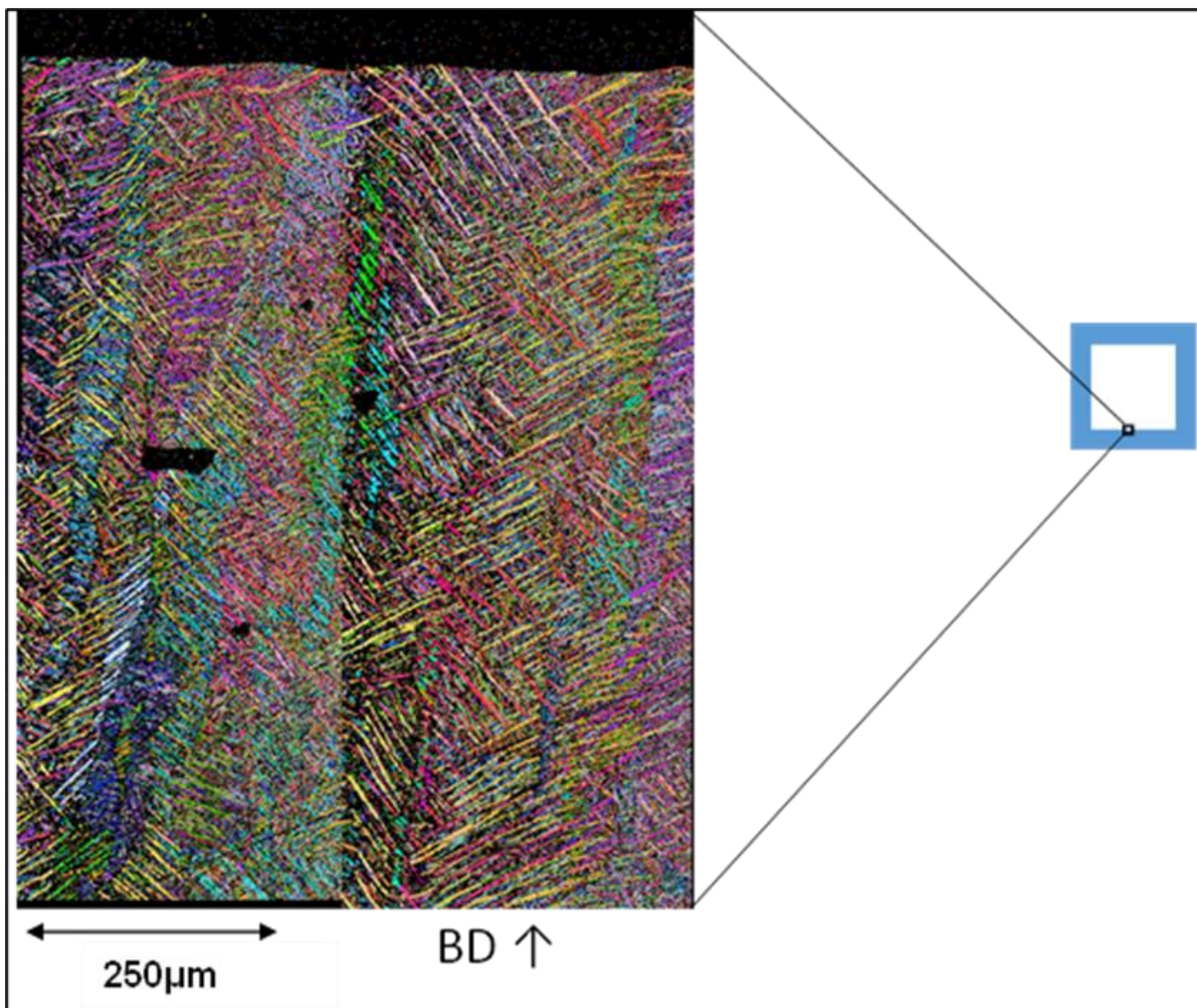


Figure 4.13 An SEM EBSD micrograph showing part of an as built AM Ti6Al4V component created to explore the variation in microstructure with component geometry, consisting of a cube with a square hole, with the image taken from the area indicated.

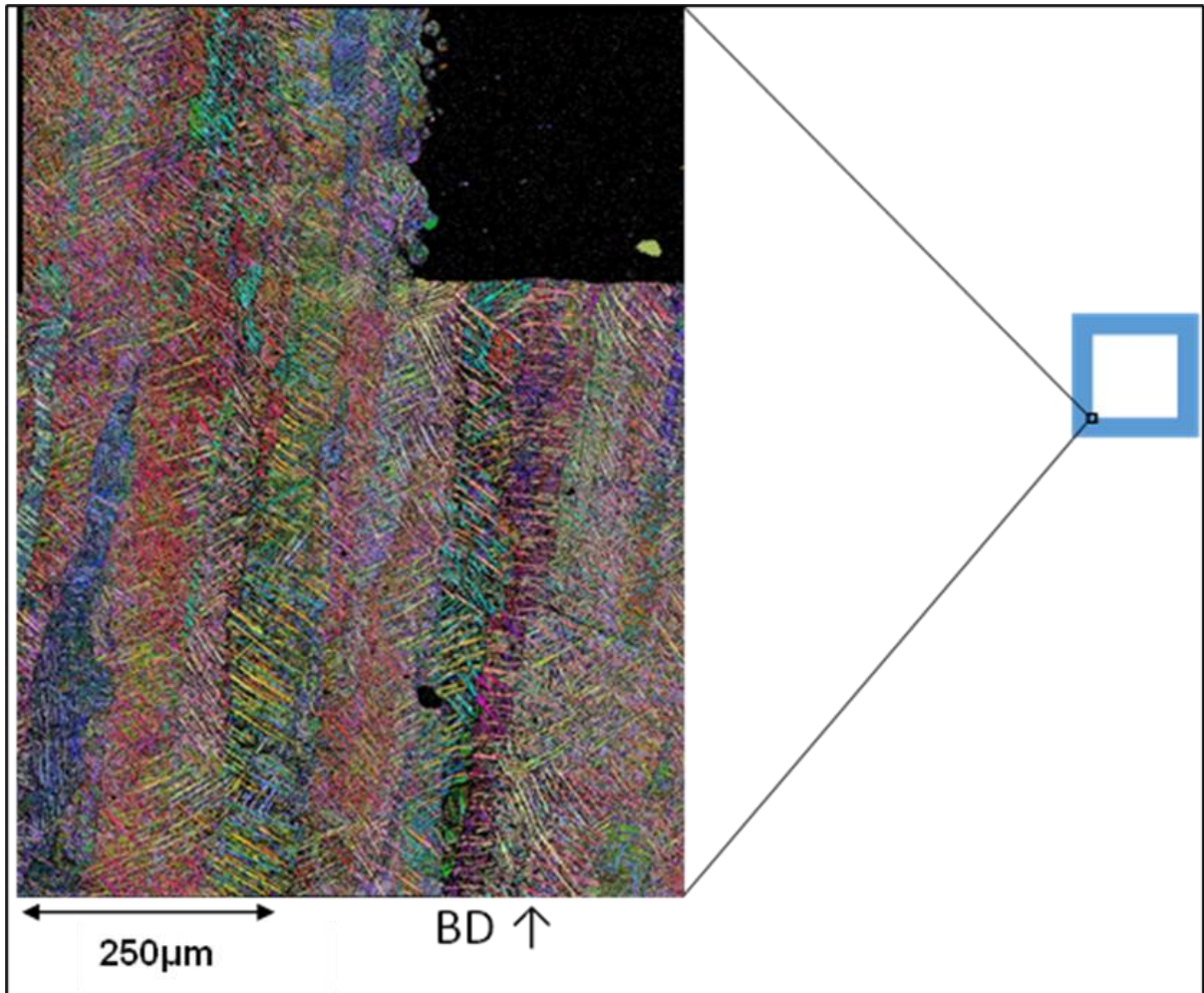


Figure 4.14 An SEM EBSD micrograph showing part of an as built AM Ti6Al4V component created to explore the variation in microstructure with component geometry, consisting of a cube with a square hole, with the image taken from the area indicated.

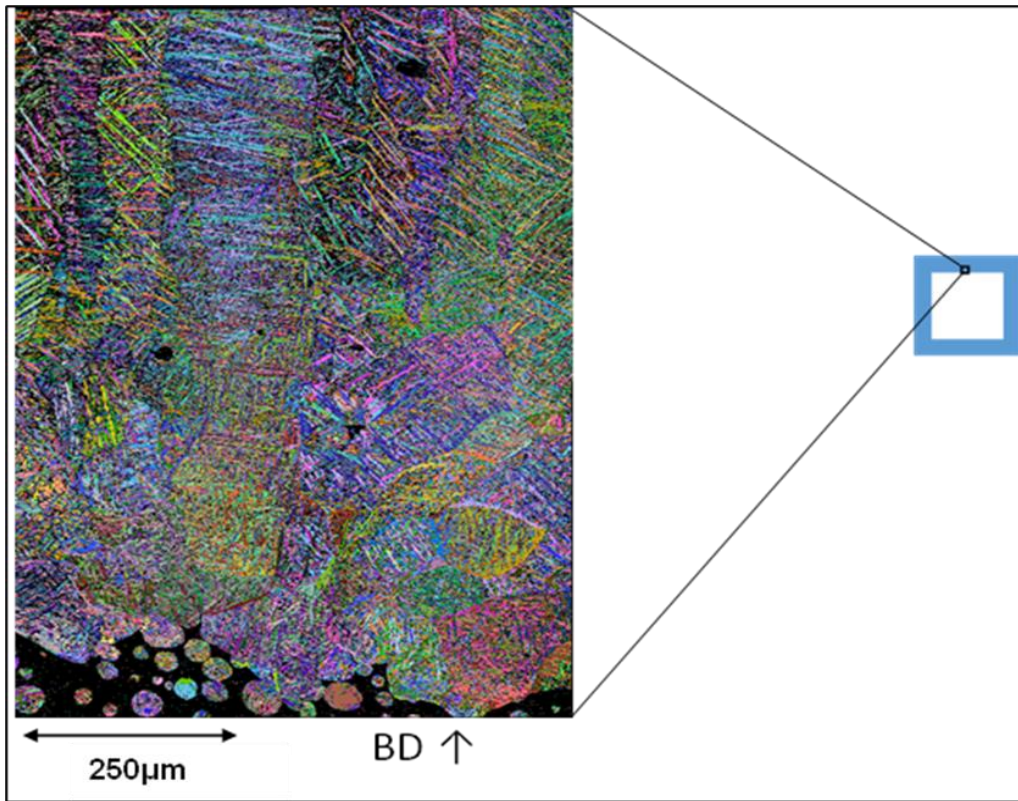


Figure 4.15 An SEM EBSD micrograph showing part of an as built AM Ti6Al4V component created to explore the variation in microstructure with component geometry, consisting of a cube with a square hole, with the image taken from the area indicated.

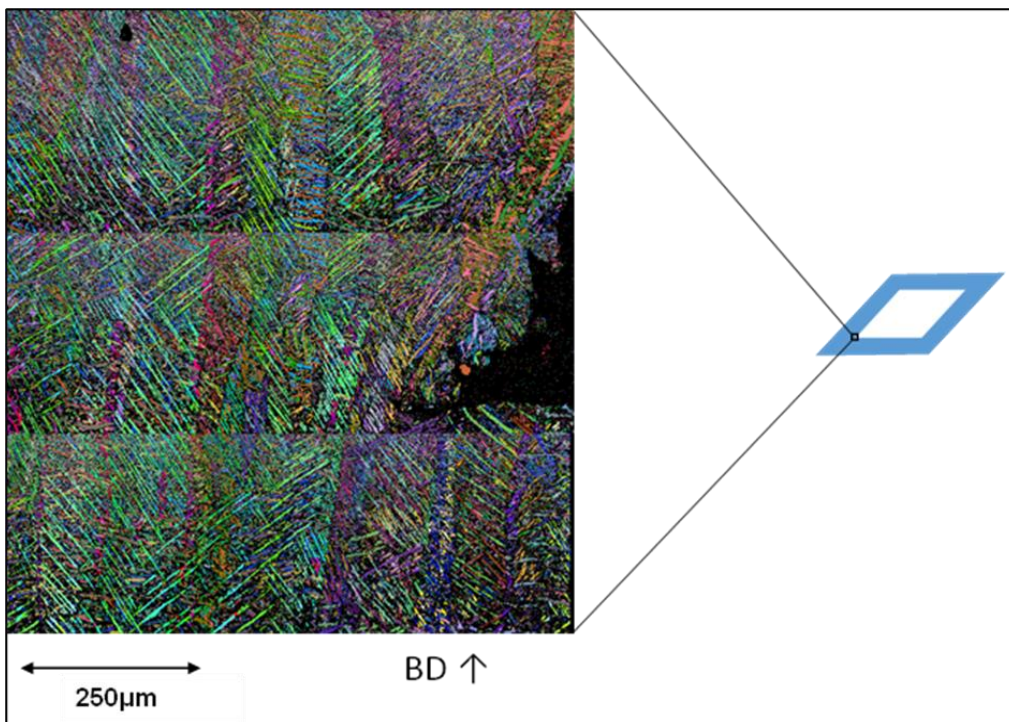


Figure 4.16 An SEM EBSD micrograph showing part of an as built AM Ti6Al4V component created to explore the variation in microstructure with component geometry, consisting of a cube with a square hole, with the image taken from the area indicated

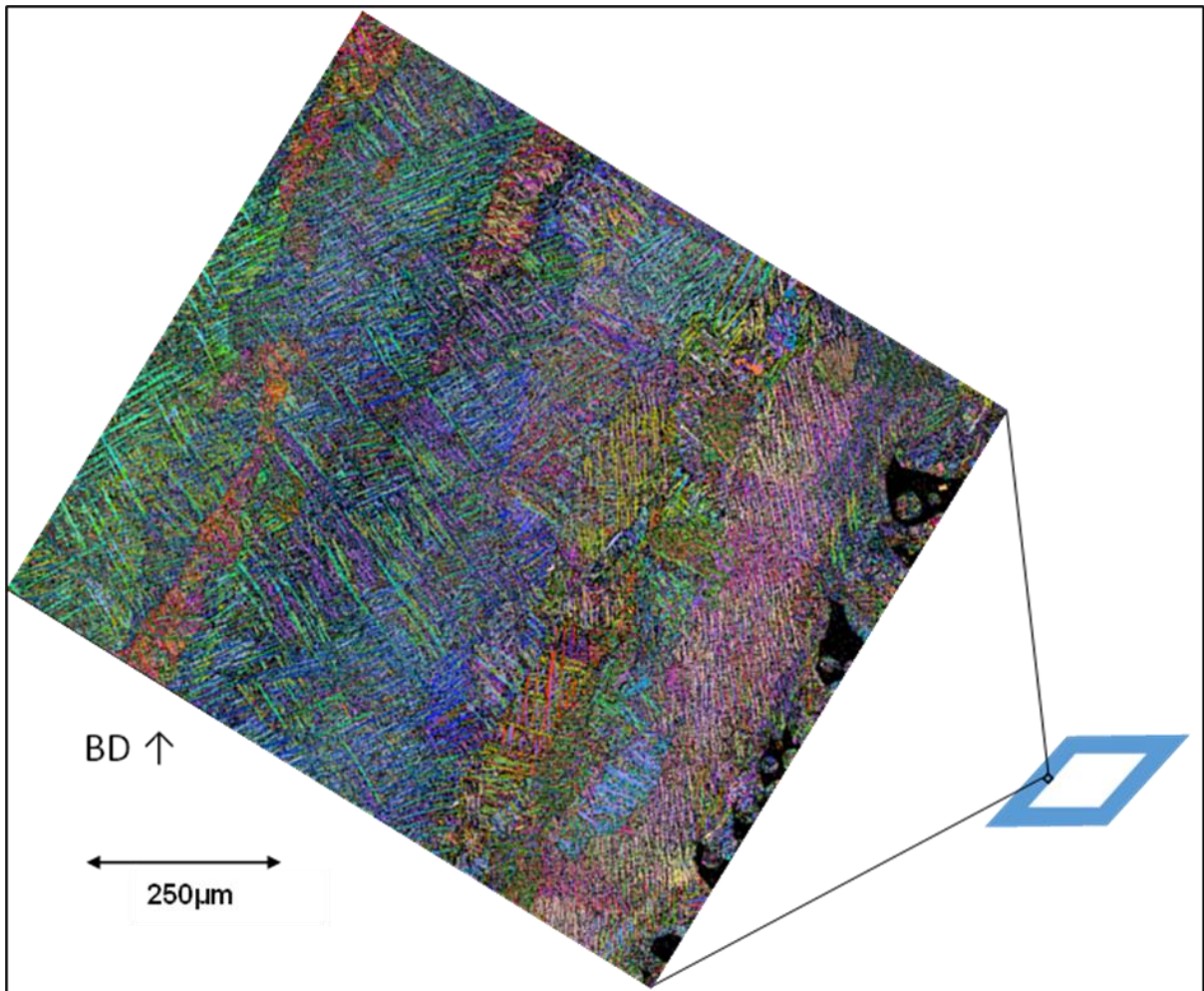


Figure 4.17 An SEM EBSD micrograph showing part of an as built AM Ti6Al4V component created to explore the variation in microstructure with component geometry, consisting of a cube with a square hole, with the image taken from the area indicated

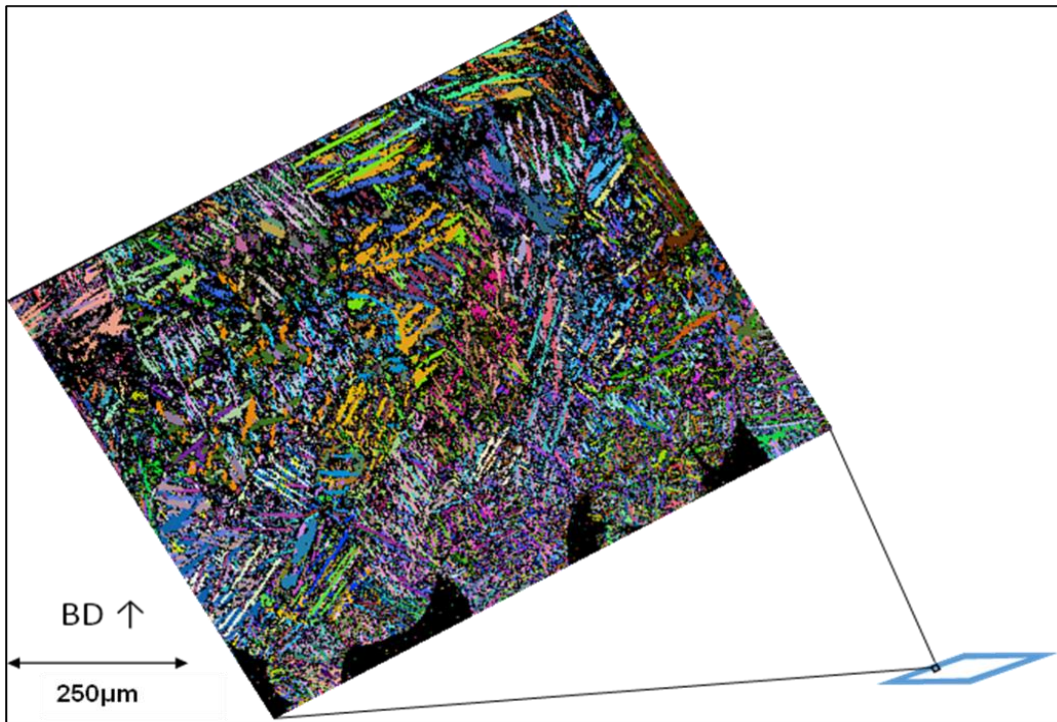


Figure 4.18 An SEM EBSD micrograph showing part of an as built AM Ti6Al4V component created to explore the variation in microstructure with component geometry, consisting of a cube with a square hole, with the image taken from the area indicated.

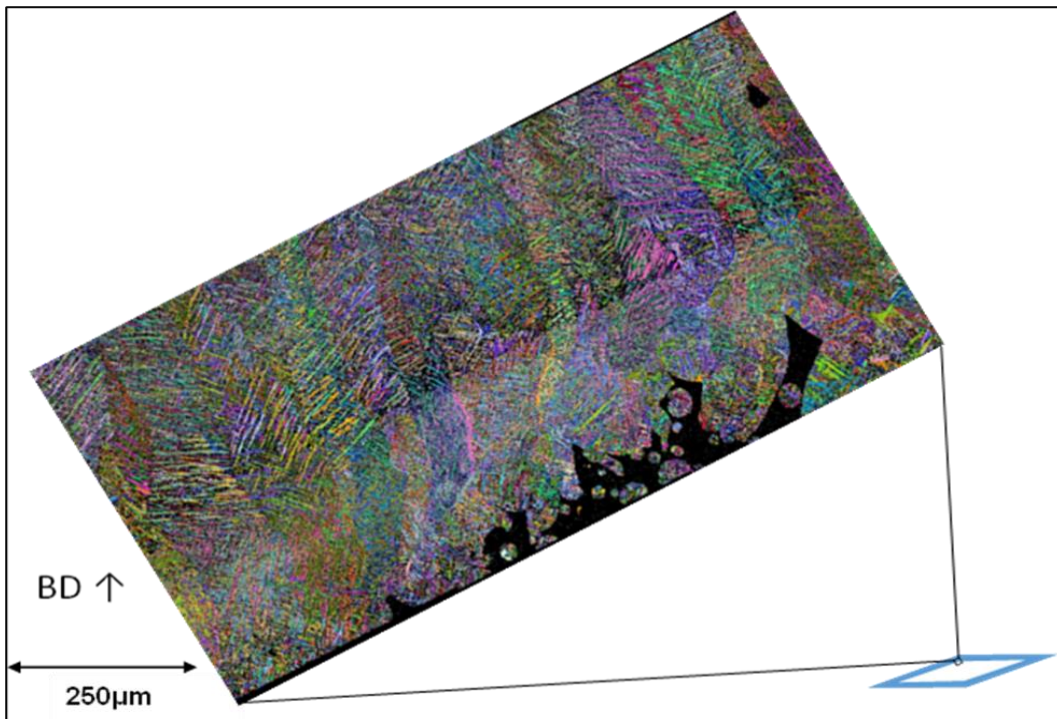


Figure 4.19 An SEM EBSD micrograph showing part of an as built AM Ti6Al4V component created to explore the variation in microstructure with component geometry, consisting of a cube with a square hole, with the image taken from the area indicated.

4.3. The Textures of different AM Ti6Al4V Samples

The crystallographic textures of AM Ti6Al4V samples in general consist of weak texture of α' phase because the parent variants of columnar β grains, which will be discussed later, and strong texture of reconstructed β grains align to the build direction \uparrow with preferential texture $\{100\}$. In this section, the focus will be on the edges of inner areas (away from the bulk) to investigate the effects of the build geometry and build angle and analyse the differences in textures between these areas and the bulk.

4.3.1. The Effect of Curvature (Cylinder, Elliptical Cylinder)

4.3.1.1. Shape-C1 Samples

The pole figures that illustrate the textures of reconstructed β (Figure 4.20) and α phase (Figure 4.21) are obtained from the data analysed to form the EBSD maps in section 4.1.1. The corresponding contour pole figures of the texture distribution of the β phase from the middle inner edge of shapeC1 samples, as shown in Figure 4.20a, revealed a strong $\{100\}$ texture in the direction of grain growth with maximum intensity of ~ 12 times that expected for random orientations. The explored area showed in the previous section a clear columnar β grain structure, produced by growth in a $\{100\}$ direction during solidification, as this is the preferential growth direction of the cubic crystal structure. The corresponding contour pole figures of the texture of the β phase from the top inner edge of the cylindrical hole, as shown in Figure 4.20b, showed other areas with higher intensity than those corresponding to the $\{100\}$ direction. These areas are rotated by ~ 15 degrees from the preferential growth direction. The mapped area has equiaxed grains and the full columnar structure of the β grains has not fully established in this zone, with some retained grains from the first material to be melted and resolidified. This could affect the texture of these areas, leading to the development of the preferential growth direction.

On the other hand, the texture of martensitic α' , as shown in Figure 4.21, was weaker and of lower intensity than the β texture. The overall texture was mainly random, and the absence of a preferential direction may be related to the high number of α' laths between prior β grains. As expected, in the corresponding contour pole figures of α' laths, the transformation from $\beta \rightarrow \alpha'$ follows the Burger Orientation relationship (BOR) which is that the $\{0001\}_{\alpha'}$ poles are parallel to at least one of the reconstructed parent poles of $\{110\}_{\beta}$ and $\{1\bar{1}20\}_{\alpha'}$ poles are parallel to at least one of the reconstructed parent poles of $\{111\}_{\beta}$. Due to the crystal symmetry, there are 12 possible variant orientations from β the parent to form α' laths but because of the fast cooling, the α' laths produced mostly appeared random to reduce the energy of phase transformation.

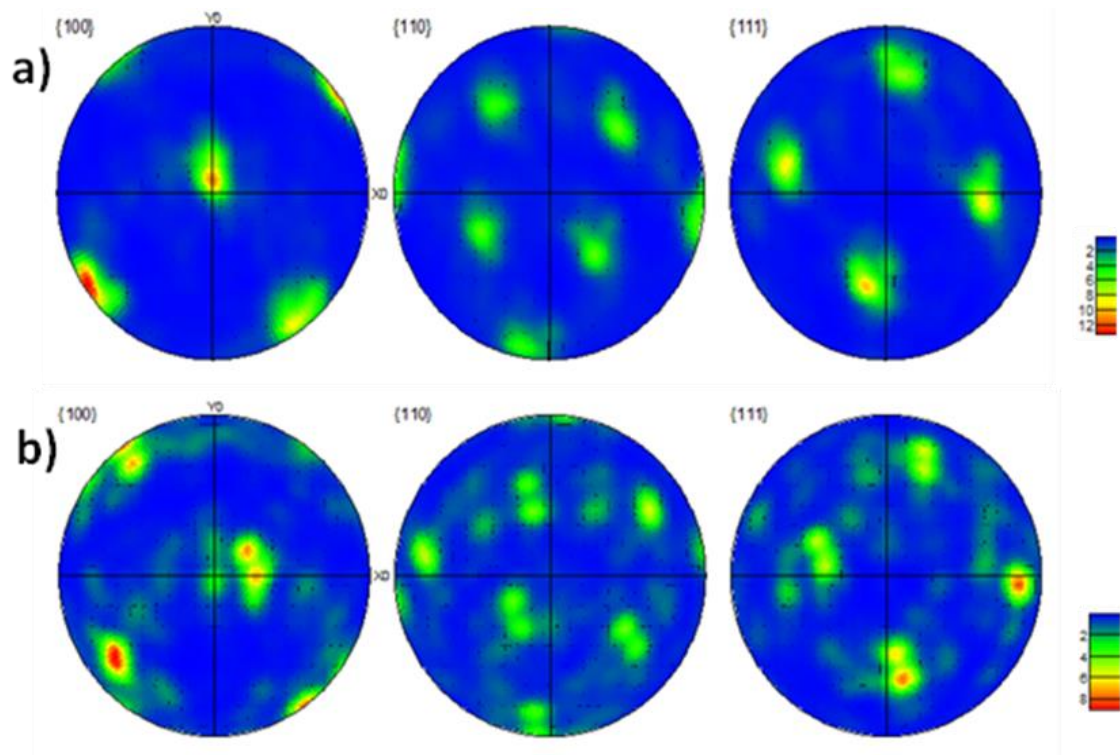


Figure 4.20 Pole figures depicting reconstructed β textures measured by EBSD; a) from the left inner edge of the cylindrical hole, and b) from the upper inner edge of the cylindrical hole.

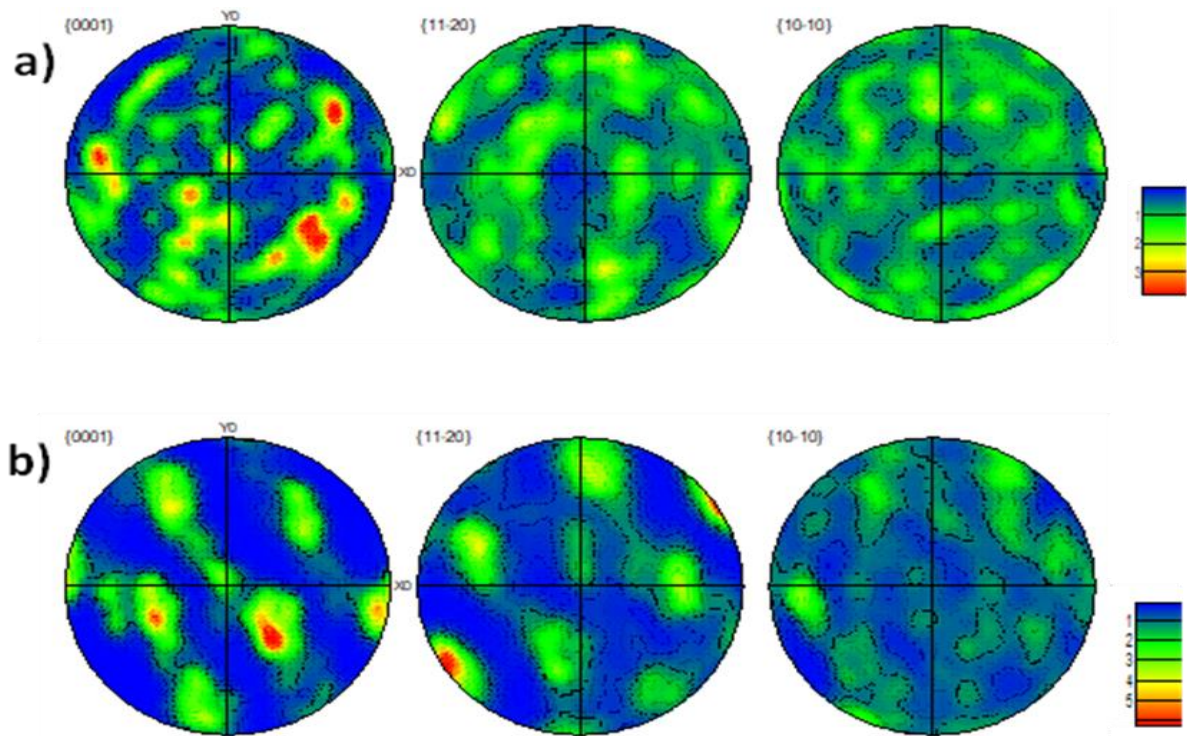


Figure 4.21 Pole figures depicting α -phase textures measured by EBSD; a) from the left inner edge of the cylindrical, and b) from the upper inner edge of the cylindrical.

4.3.1.2. Shape-E1 and Shape-E2 Samples

The corresponding contour pole figures of shape-E1 and shape-E2 samples (with the longer radius of the ellipse oriented horizontally and vertically) showed similar behaviour to shape-C1 in the previous section (4.3.1.1). The textures of reconstructed β from the middle and top inner edge, as shown in Figure 4.22, showed a strong $\{100\}$ texture in the direction of grain growth with maximum intensity of ~ 7 and 12 times random respectively. In the top side, there were several areas that showed different orientation as shown in Figure 4.22a. This is likely to be because of the equiaxed grains near to the edge where the new grains nucleate, and the columnar β grain structure fully formed. The similarities with the shape-C1 shape indicate that at the scales of the shapes investigated (shape-E1 and shape-E2), the minor differences in the angle of the surface do not affect the internal crystallography of the metal,, as shown in Figure 4.24.

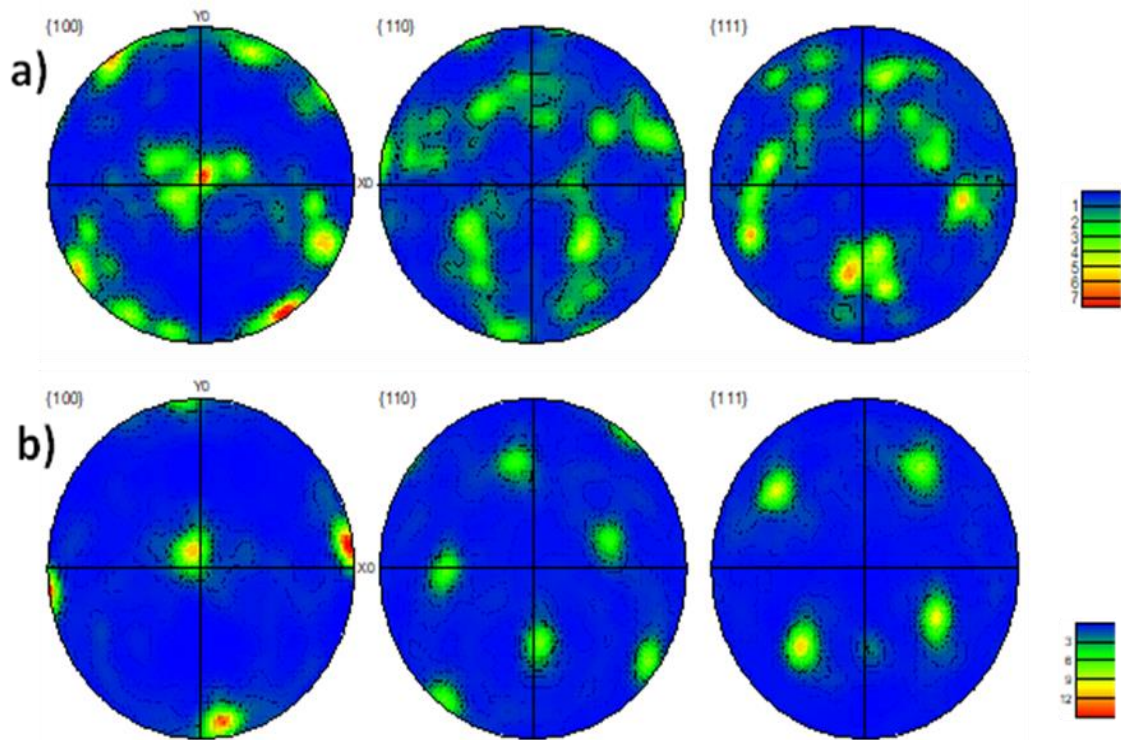


Figure 4.22 Pole figures depicting reconstructed β textures measured by EBSD; a) from the upper inner edge of the horizontal elliptical cylindrical, and b) from the left inner edge of the horizontal elliptical cylindrical.

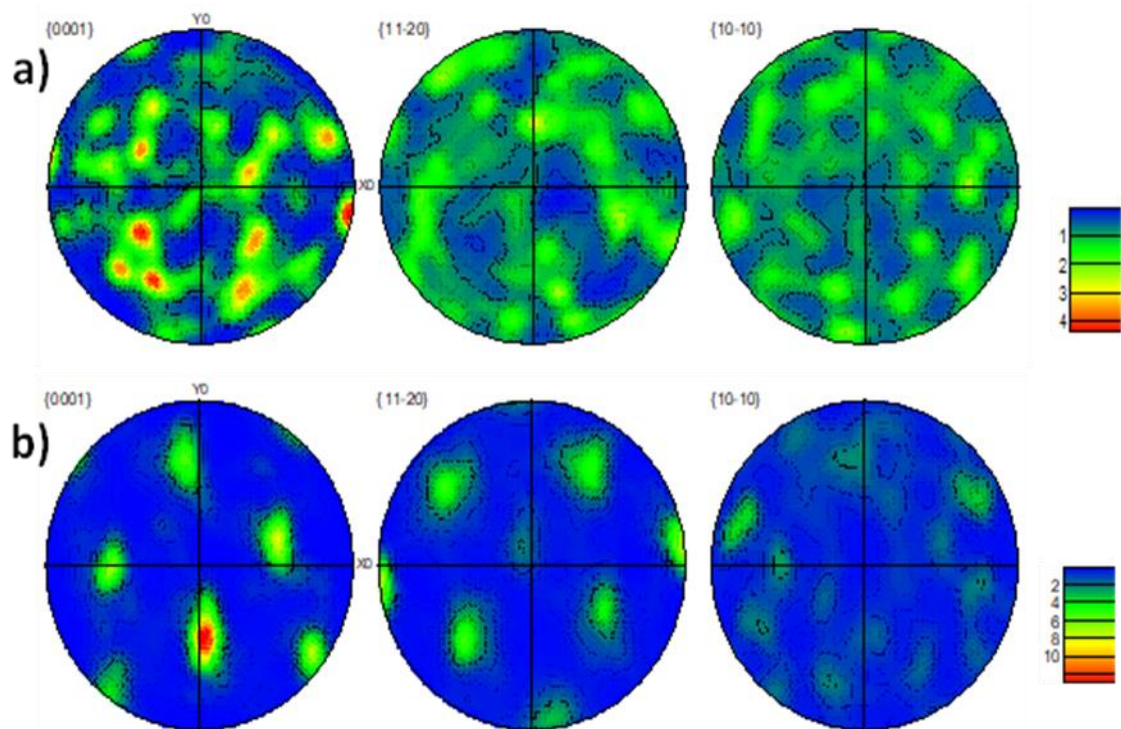


Figure 4.23 Pole figures depicting α -phase textures measured by EBSD; a) from the upper inner edge of the horizontal elliptical cylindrical, and b) from the left inner edge of the horizontal elliptical cylindrical.

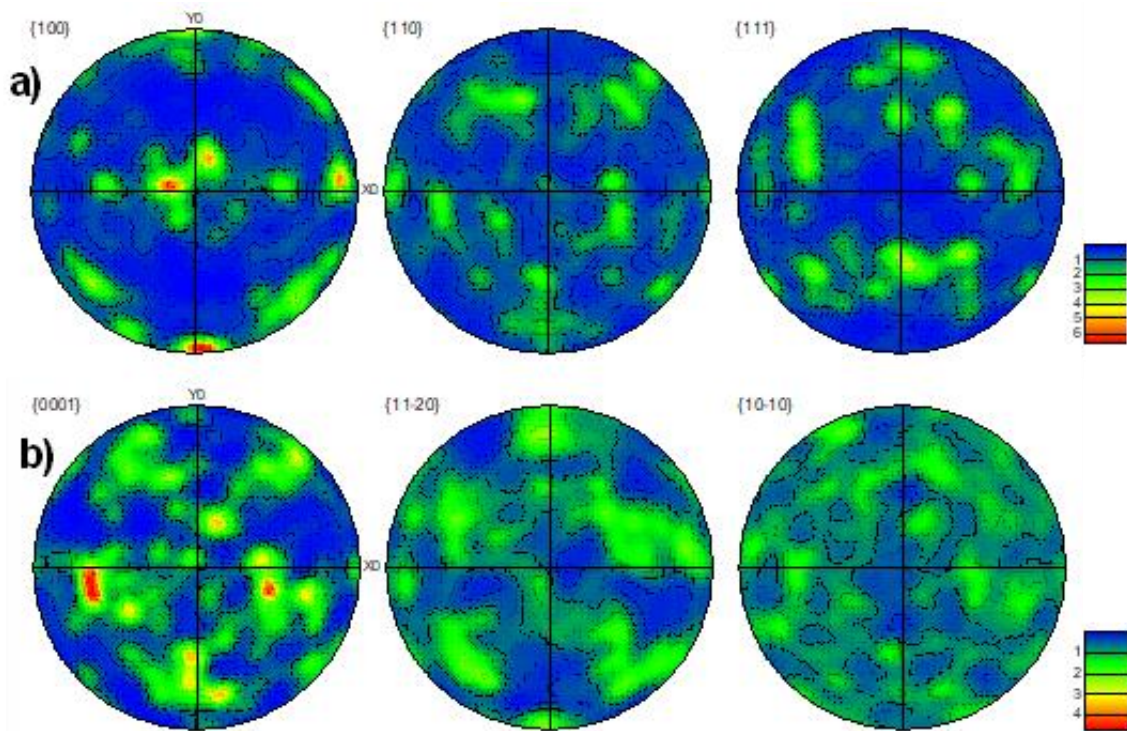


Figure 4.24 Pole figures depicting textures measured by EBSD from the bottom inner edge of the vertical elliptical cylindrical: a) β -phase, and b) α -phase.

4.3.2. The Effect of Build Angle on the Texture

The three different samples with parallelepiped holes (angled 0° , 45° , and 70° away from build direction) showed similar crystallographic textures to the cylindrical samples in the mapped areas. The middle inner edge, as shown in Figure 4.25, revealed a strong $\{100\}$ texture in the direction of grain growth of reconstructed β grains. The inclination has no effect on the textures because the columnar grains continued in the same direction \uparrow . This also has similarities to the results from the investigation of the effect of different inclination angles for square holes and the narrow walls to grow within, and is similar to results reported by Antonyamy et al. 2013 [120].

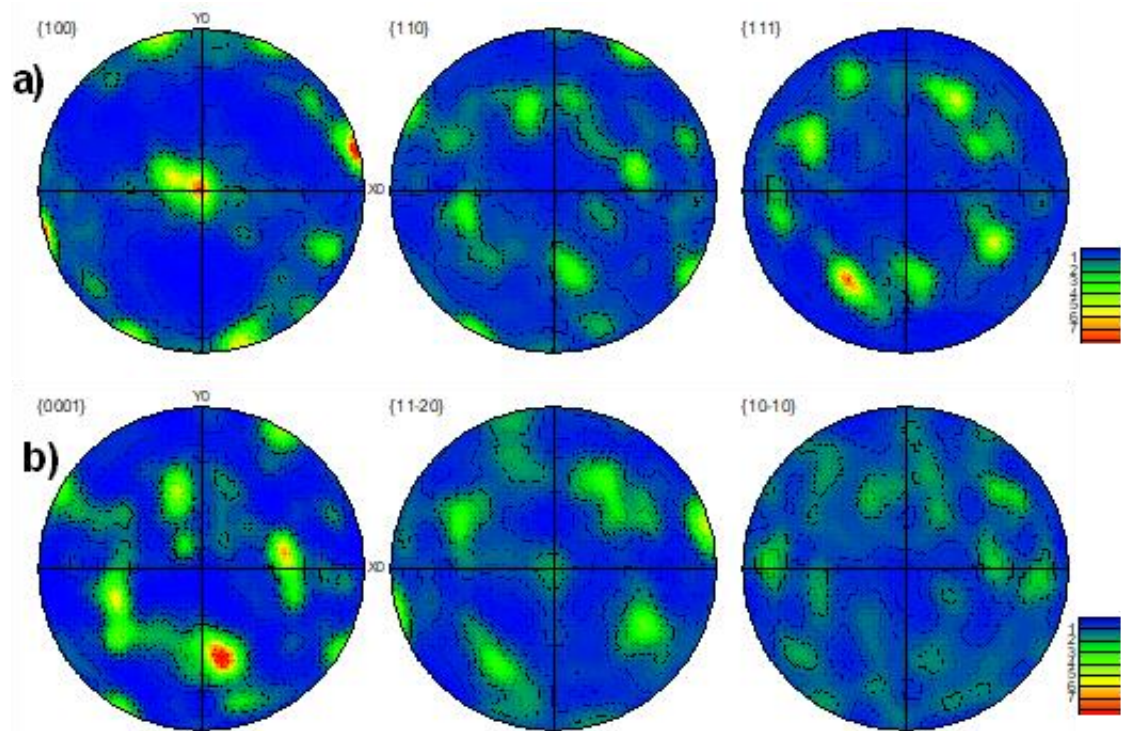


Figure 4.25 Pole figures depicting textures measured by EBSD from the middle inner edge of the cubic hole: a) β -phase, and b) α -phase.

4.4. Chapter Summary

The effect of component shape on Ti6Al4V microstructure and texture produced by Selective Laser Melting (SLM) has been studied in this chapter. The objective was to create different shapes to investigate three main features: 1) Changing thickness, 2) Curvature, and 3) Inclination of build angle. The results presented in this chapter suggest the following:

- 1- The microstructure of top inner edge area (area no.1) , as shown in Figure 4.26, regardless of the hole shape (cylindrical or cubic) consists of equiaxed $\alpha + \beta$ grains near to the edge then the columnar β grains starts growing. This happens because of the thermal gradient at the melt pool and how it is built up layer by layer after the gap in the structure.
- 2- The texture of this area (area no.1 Figure 4.26) of reconstructed β grains is more random from the preferential growth direction (build direction) than other areas because of the equiaxed grains and the full columnar structure of the β grains has not fully established in this zone, with some retained grains from the first material to be melted and resolidified.
- 3- The microstructure of side inner edge area (area no.2) , as shown in Figure 4.26, suffers from surface roughness perhaps because of the unmelted particles being incorporated, which led to nucleate equiaxed $\alpha + \beta$ grains near to the edge before joining the columnar β grains that already nucleated from the base and continued growing vertically in build direction \uparrow .
- 4- The texture of this side inner edge area (area no.2 Figure 4.26) of reconstructed β grains is more organised and aligned into the preferential growth direction (build direction) than other areas because of the well-established columnar grains of β .
- 5- Regardless the edge shape (straight line or curved), the microstructure of bottom inner edge area is fully α' martensitic within prior β grains which grow vertically in columnar shape through several layers. If the inner edge shape is straight line (area no.3) , as shown in Figure 4.26, the surface will be flat, and the roughness will not appear.

- 6- The microstructure of area no.4 (curvy), as shown in Figure 4.26, will be similar to area no.3 (straight line) but the columnar β grains will be inclined away from the build direction \uparrow due to the thermal gradient which is result of the shape demand (sharp curve). The surface will be rougher than the straight line (area no.3) because of the condensing of unmelted powder.
- 7- The surface roughness in the samples is clearly visible, and is high due to the manufacturing process, where the large melt pool, exposure time, the inclination, and the curvature of some of the regions of samples, cause semi-melted powder particles to be incorporated into the surface. The areas denoted no.1 and no.2 are the most effected due to the gravity and capillary forces.

It can be assumed that features of similar type, where present in other geometries, including in lattice samples with repeating unit cell based structures, will give comparable microstructures, and that these results can therefore be used as a basis to make predictions of such structures. Based on the information collected (which is limited in terms of the full sample edge and the depth into the sample), it is not possible to define the dimensions of the roughness, or the size of these different areas. Nevertheless, the roughness is estimated to be at least 50 μm , and the areas are observed covering up to a millimetre of surface; both of these measures are likely to be larger than these lower limits.

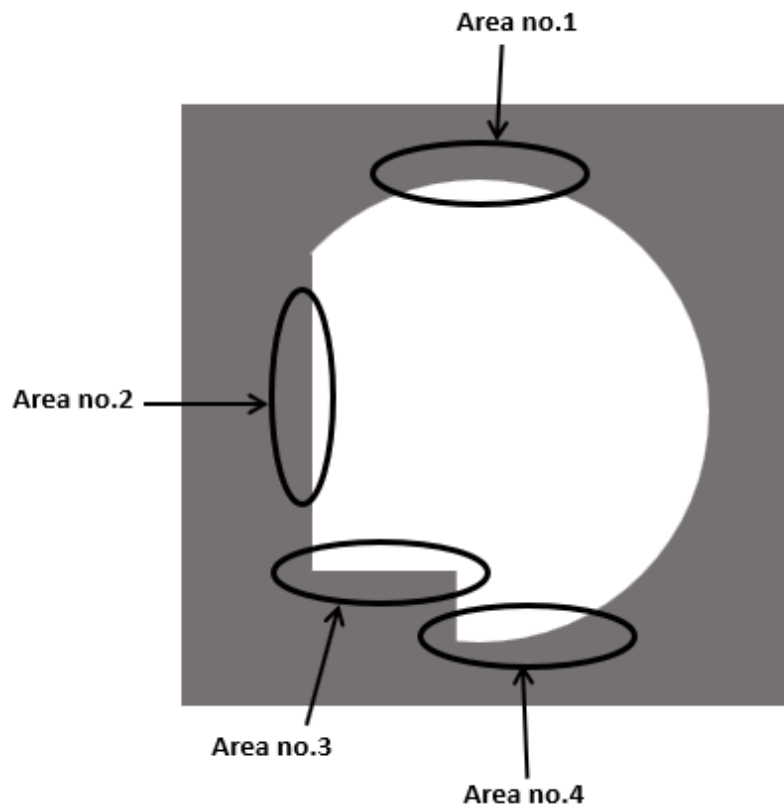


Figure 4.26 A sketch showing different areas in a sample with different features that using to illustrate the summary of the results.

Chapter 5 : Effect of Degree of Microstructural Order on Elastic Behaviour in Ti-6Al-4V

Numerical models have the capability to simulate and assess the impact of the microstructural inhomogeneity on the mechanical properties. One of the objectives of this project is to develop the simulation capability to evaluate and validate this impact of the microstructure on the mechanical properties for lattices. Due to the potential range of structures and complexity of lattices, it is not possible to experimentally explore behaviour, and a predictive approach is needed. Therefore, to achieve this objective, the FEM models need to simplify to the basic in terms of structure (solid cube) or materials (Ti6Al4V α and Ti6Al4V β separately) and validate these conditions. Then, the models need to be developed from single crystal to multi-grains and using the two phases of Ti6Al4V that are present in real samples together. Finally, simulation of the structure of shape-C1, one of those produced and examined in the previous chapter, will permit investigation of the effect of microstructure of this mesostructure on the mechanical properties.

5.1. Setup Boundary Conditions and Validation

In order to represent the real structure of lattices, specific boundary conditions were applied, intended to make the simulation close to the actual experiments. The boundary conditions that are used in the ANSYS simulation are 1) two centre lines on the bottom surface, forming a plus sign “+” structure and 2) relative positions and orientations of the structure are fixed in the x and z directions while allowing their lengths to change. The same conditions are used in the literature [77] for modelling of this kind as are used in this project, with some modifications to fit with the required structures. These conditions, as shown in Figure 5.1, are: 1) the displacement on the top surface represents the applied strain, which is set as a value of -1.5×10^{-3} in the y-direction, as an arbitrary strain level consistent with elastic deformation, 2) the two centre lines on the bottom surface are both constrained in

the y-direction, but are free to extend along their length (line A is free in z and line B is free in x), and 3) the bottom surface is constrained in the y-direction but is free in both x and z directions to allow the shape to expand. A test was run with a simple cube, set to have the properties of standard Ti6Al4V, and the result of equivalent (von Mises) stress under this strain condition was 171 MPa, as shown in Figure 5.2, which shows a uniform stress distribution (which would be expected for a solid object, stress concentrations would indicate problems with the constraint applied by the boundary conditions) and this gives a Young's modulus of 114 GPa, agreeing with the input material properties. This provides a basic validation of the material property set input and the implementation of basic compressive elastic deformation in the model.

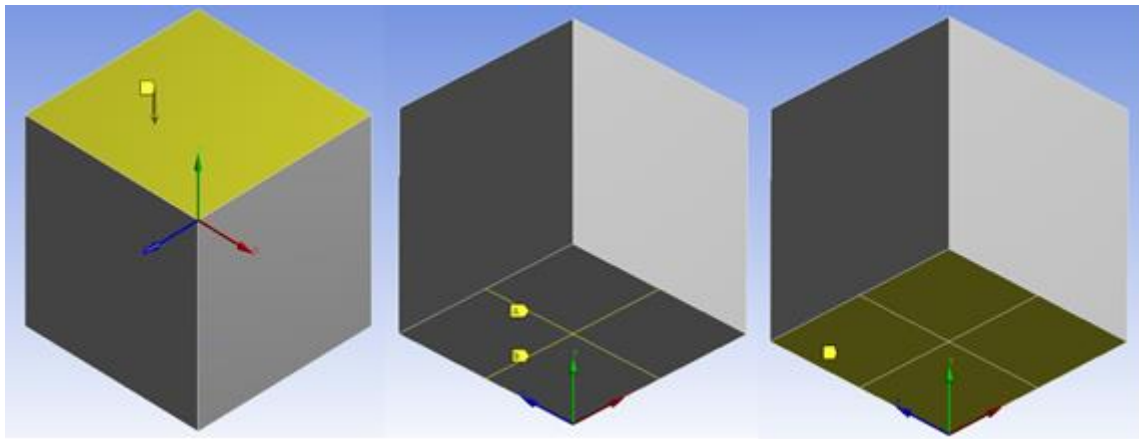


Figure 5.1 A finite element model of a solid cube unit cell showing the boundary conditions that are applied on the cube.

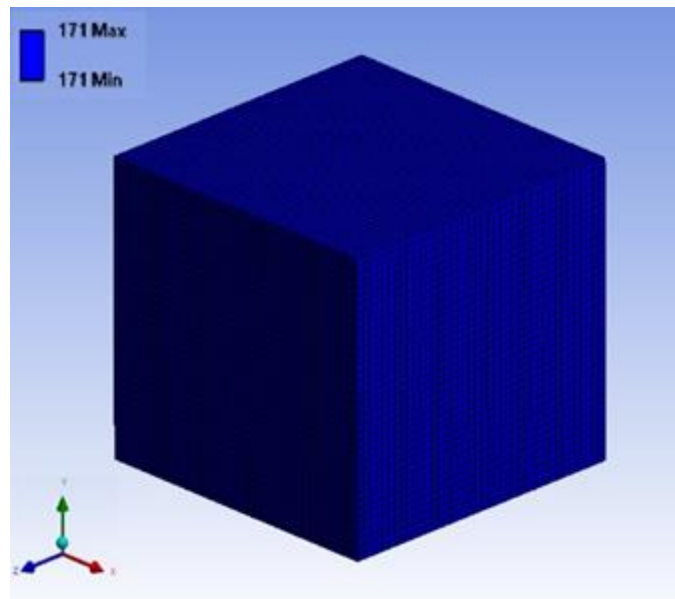


Figure 5.2 The von Mises stress results of the cube unit cell under compression to a strain of -1.5×10^{-3} , the blue colour represents the even stress inside the cube.

5.2. Comparing between α and β as Ti6Al4V Phases

In order to understand the anisotropic behaviour of α and β phases separately, 1) the two different specific stiffness matrices described in 3.8 were used, and 2) a new coordinate system was established to rotate the materials' orientation (the crystal orientation) within the unrotated physical structure, as represented in the diagram in Figure 5.3a. The purpose of the new coordinate system was to control the rotation of the crystallographic orientation of the material inside the structure, so that the effect of the material's orientation on the elastic properties could be captured. The rotational movement was based on rotating the axes through certain angles; to do that, "yaw", "pitch", and "roll" axes were used to simplify the rotation, as shown in Figure 5.3b and Figure 5.4. Yaw represents rotation around the y-axis, and its Euler angle is ψ° , Pitch represents rotation about the x-axis, and its Euler angle is θ° , and Roll represents rotation about the z-axis, and its Euler angle is ϕ° . The material within the model was rotated in 10° steps from 0° to 180° for each axis (yaw, pitch, and roll) separately. The tests on the models

were done under the same strain as previously, -1.5×10^{-3} , and the stress results were used to calculate the Young's modulus for linear elastic deformation in each condition.

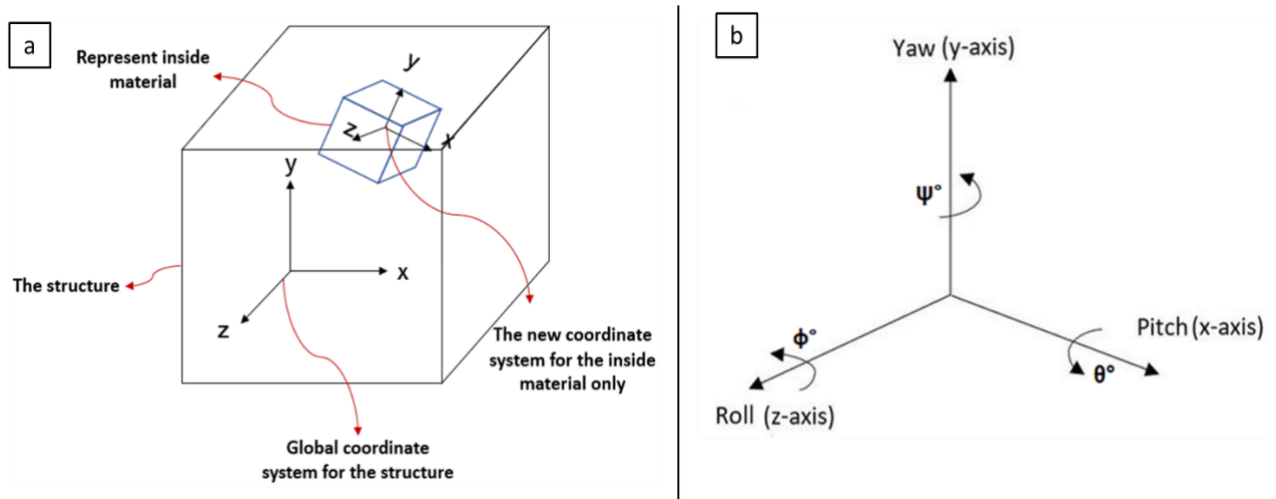


Figure 5.3 A diagram illustrates the model structure and different coordinate systems. a) The black cube represents the model that using in FEM, the blue cube represents the material of the model. b) A diagram shows the coordinate system X,Y,Z as Pitch, Yaw, Roll their angles ϑ , ψ , ϕ .

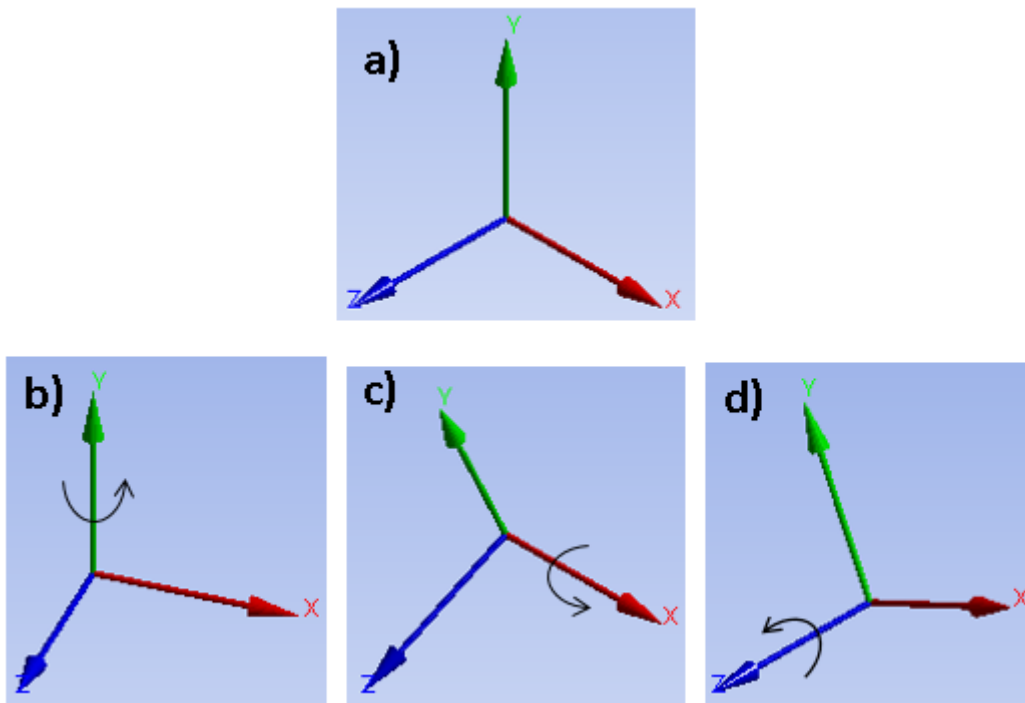


Figure 5.4 Four images of the coordinates system that used in ANSYS showing different rotations. a) Global coordinates system without rotation. b) Global coordinates system with rotation around Yaw (green). c) Global coordinates system with rotation around Pitch (red). d) Global coordinates system with rotation around Roll (blue).

In this test, the anisotropic behaviour of the Ti6Al4V α -phase and the β -phase was investigated individually to determine the effect of crystal orientation on the elastic behaviour. The results using the stiffness matrices for Ti64- α and Ti64- β separately, as shown in Figure 5.5 and Figure 5.5, showed three different behaviours of the structure's stiffness, with angle of rotation around different axes rotation. In these figures, the orange line represents the Young's modulus of the structure while the crystal structure of the material is rotated around the "roll" axis by ϕ° and $\theta^\circ = \psi^\circ = 0$. The blue line represents the Young's modulus of the structure while the crystal structure of the material is rotated around the "pitch" axis by θ° and $\phi^\circ = \psi^\circ = 0$. Finally, the grey line represents the Young's modulus of the structure while the crystal structure of the material is rotated around the "roll" axis by ψ° and $\theta^\circ = \phi^\circ = 0$.

Firstly, the results generated using the stiffness matrix for Ti64- α (Figure 5.5) showed the highest stiffness for the conditions calculated is 167.53 GPa, which is measured when the crystal structure of the material is oriented at 45° or 135° around the roll axis (orange line); this is relative to the starting orientation where the crystal structure is lined up with the c axis of the hexagonal unit cell along the direction of the mechanical test. The pattern of the variation in stiffness was symmetrical around 90° , but it was different from the roll axis (orange line) when the pitch axis (blue line) was tested. Here the highest stiffness modelled was 158.97 GPa at angles of rotation of 60° and 120° . This is consistent with the symmetry of the unit cell structure of Ti64- α , which is hexagonal close packed (HCP), with identical stiffness values being found when the rotation brings crystallographically identical directions into the same alignment. Finally, the rotation around the yaw axis (the load-direction axis) had no effect on the stiffness of the structure, as this does not change any aspect of how the load interacts with the material structure.

Modelling with the stiffness matrix of Ti64- β (Figure 5.6) showed an identical performance around the roll and pitch axes, while using β -phase properties, with patterns reflecting the symmetry of the crystal structure of β , which is body centre cubic (BCC). The highest stiffness is 80.44 GPa when the crystal structure of the material is rotated by 45° or 135° around the roll axis (orange line) or pitch axis. Interestingly, the structure showed the highest overall stiffness of 119 GPa when the material rotated 45° around the roll axis,

45° around the pitch axis and 0° around the yaw axis. This result could be related to bringing the close packed direction of the atoms in the unit cell ([111]) into alignment with the test direction, giving increased stiffness, as the density of bonds is greatest along this direction. Finally, the rotation around the yaw axis (grey line) also had no effect on the stiffness of the structure, as it is not changing anything about how the bonds are loaded.

To conclude, there is an appreciable effect of the orientation on the structure's stiffness in both tests. In Ti64- α case, the stiffness increased by 54.05% during the rotation around the roll axis (z-axis) and it is increased by 46.18% during the rotation around the pitch axis (x-axis). In Ti64- β case, the stiffness increased by 131.02% during the rotation around the roll axis (z-axis). This is clear evidence on that the stiffness of the single crystal affected by the crystal orientation. In addition, the orientation has bigger impact on single crystal made from Ti64- β material than Ti64- α , which could be related to the crystal structure of the material and the differing symmetry the two-unit cells present.

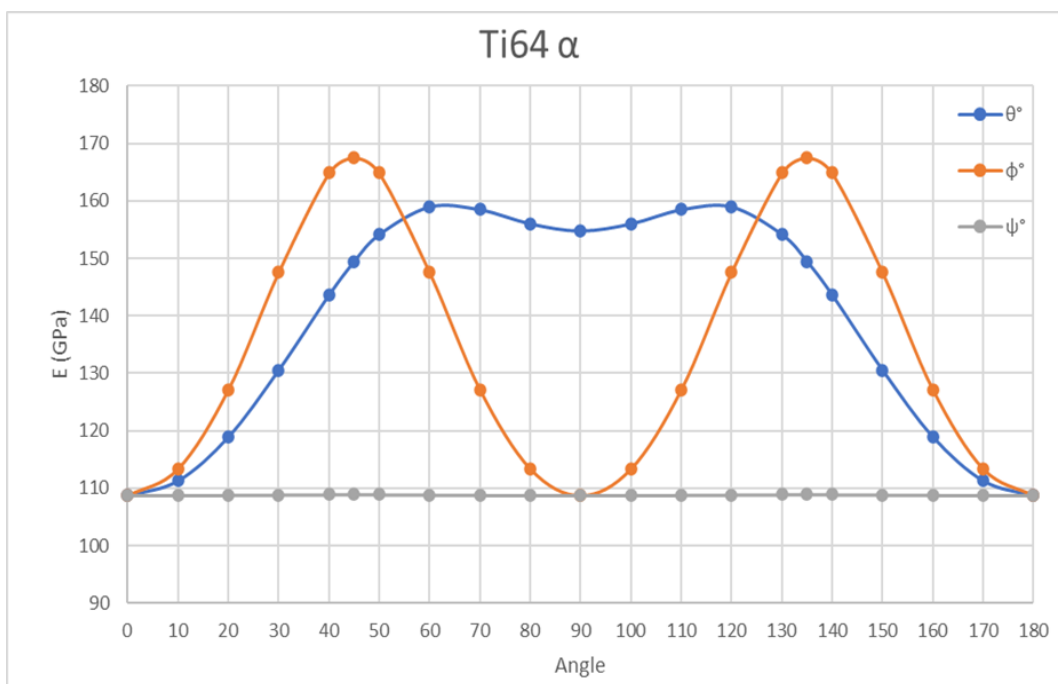


Figure 5.5 showed three different relationships of the structure's stiffness (E) of Ti6Al4V α , with angle of different axes, the orange line represents E while the crystal structure of the material is rotated around roll axis. the blue line represents E while the crystal structure of the material is rotated around pitch axis. the grey line represents E while the crystal structure of the material is rotated around yaw axis.

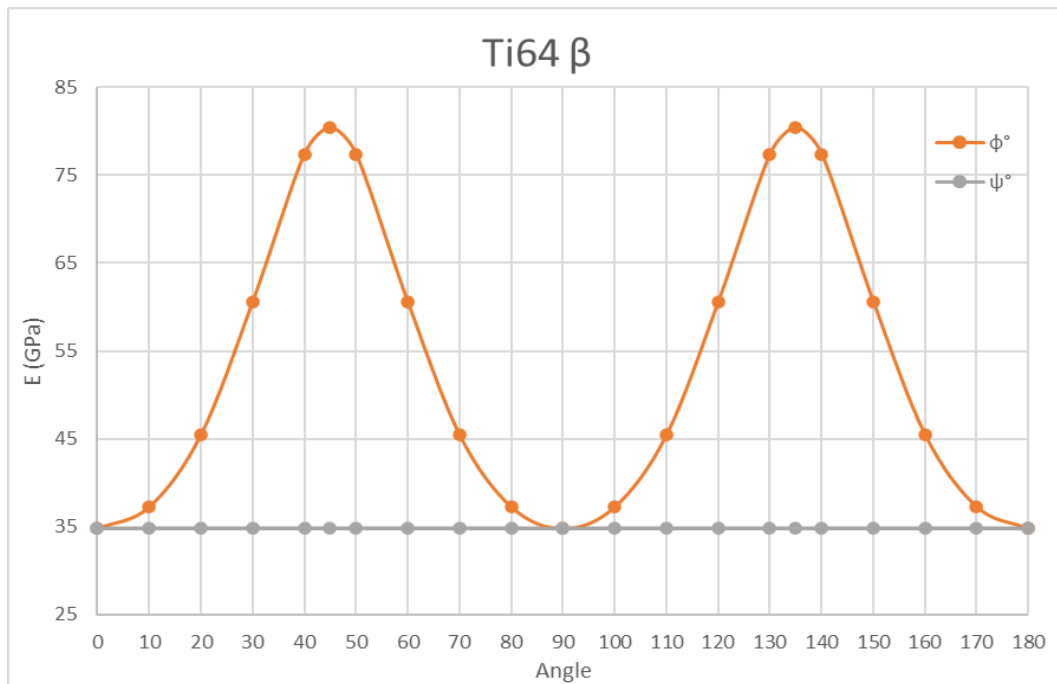


Figure 5.6 showed three different relationships of the structure's stiffness (E) of Ti6Al4V β , with angle of different axes, the orange line represents E while the crystal structure of the material is rotated around roll axis. the grey line represents E while the crystal structure of the material is rotated around yaw axis.

5.3. Simulation of Ti6Al4V with α and β Phases together

In the most commonly used condition, Ti6Al4V is an α - β alloy, having two phases present. Therefore, to properly capture the material behaviour, it is necessary to model both phases together in the structure at the same time. In this test, the anisotropic behaviour of Ti6Al4V with both α -phase and β -phase regions was investigated to determine the effect of the crystal orientation in each phase on the properties. In the previous test, one cube was used to represent the entire structure, and this worked because only one set of properties was required. However, the one cube approach cannot be applied in this test, due to the difference between α and β in the real composition of Ti-6Al-4V. A new model was set up, consisting of 64 cubes ($4 \times 4 \times 4$), as shown in Figure 5.7, where each cube represents a simplified single grain (the shape of grains as cubes, the single size of these and the regular arrangement is of course non-physical, but the model

is here investigated for its capacity to capture basic behaviour). In order to set the materials' limits, a series of tests was done from 0% to 100% α -phase concentration, while β -phase concentration was correspondingly decreased from 100% to 0%, with the results for the overall stiffness shown in Figure 5.8. The orientation of the cubes in this particular test was toward the global coordinate system.

Firstly, an ordered configuration corresponding to the rule of mixtures was used in this simulation to set the upper bound for the stiffness of the different proportions of the two phases, and one corresponding to the inverse rule of mixtures for lower bounds. The upper level (the axial loading, yellow line in Figure 5.8), was produced by modelling a columnar structure as shown in Figure 5.9a. The model material properties were those of the Ti-6Al-4V β -phase, initially at 100%, then substituted gradually with material with α -phase properties. For the lower stiffness limit (the transverse loading, blue line in Figure 5.8), was produced by modelling a row-by-row structure, as shown in Figure 5.9b. The model material properties were once again those of the Ti-6Al-4V β -phase, initially at 100% then substituted gradually with material with α -phase properties. When these limits were determined, three different trials were performed to validate the model for further experiments; the goal is to model more realistic (random) configurations of the two phases, and ensure the results are within the bounds. Three trials were performed by allocating α -phase properties to cubes at random, along with different proportions of β -phase. The results are shown in Figure 5.8 (the blue, orange, and grey dots), and show the model is broadly consistent, with some level of variation in repeated structures with the same proportion of the two phases, but in different configurations. The maximum variation between repeats of the same structures was found at intermediate proportions (which is understandable as in this range the number of possible different configurations of α -phase and β -phase cubes – and therefore different properties - is higher) and is of 3MPa (5%) or less. The next point of validation was to compare the simulation results with results from the simple rule of mixtures estimates.

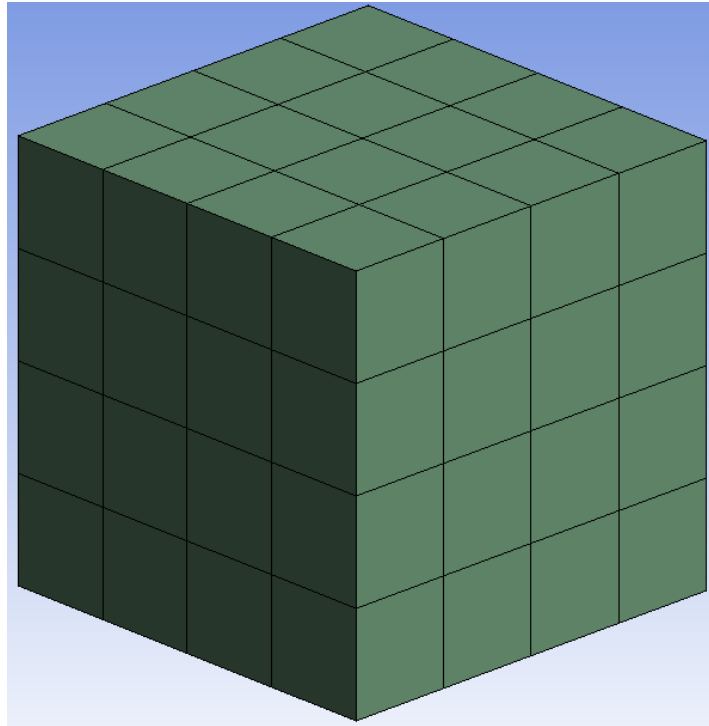


Figure 5.7 A finite element model of 64 cubes (4×4×4) and each cube will represent a single grain.

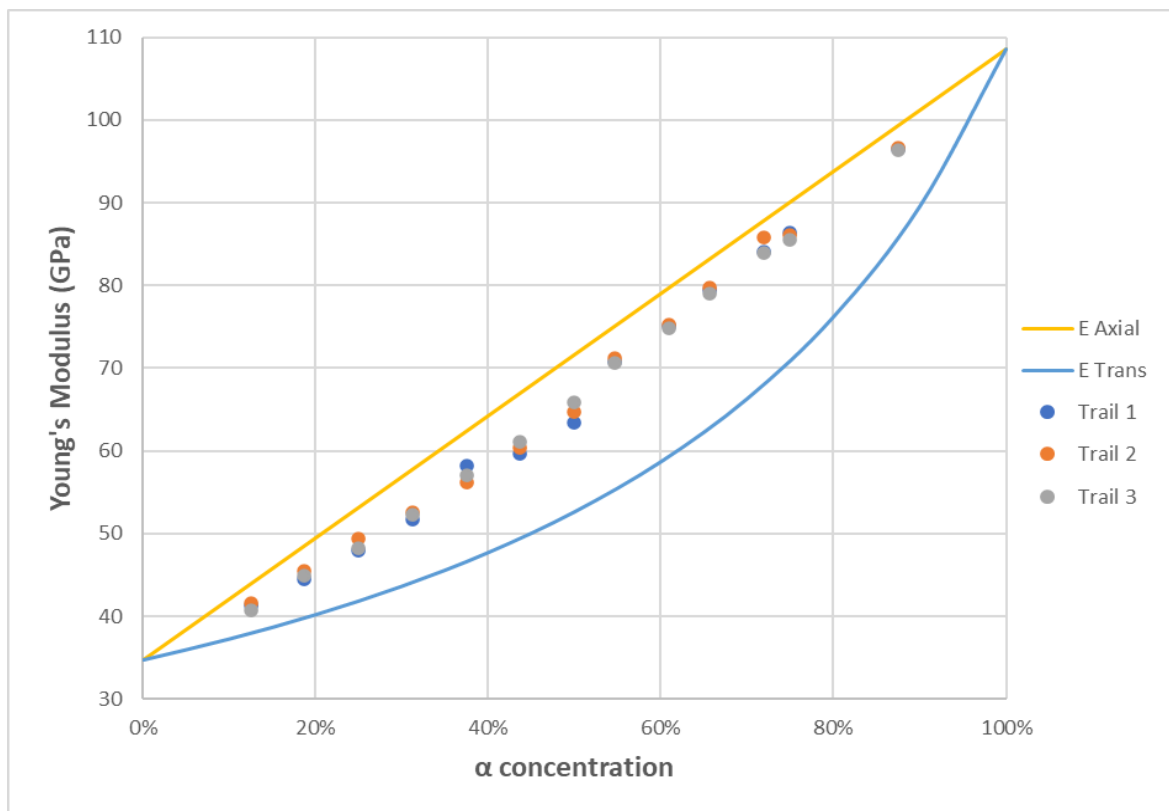


Figure 5.8 Illustrates the relationship between Young's Modulus (E) and α phase concentration in α and β structure. The yellow line represents the columnar structure (axial loading), the blue line represents the row-by-row structure (transverse loading).

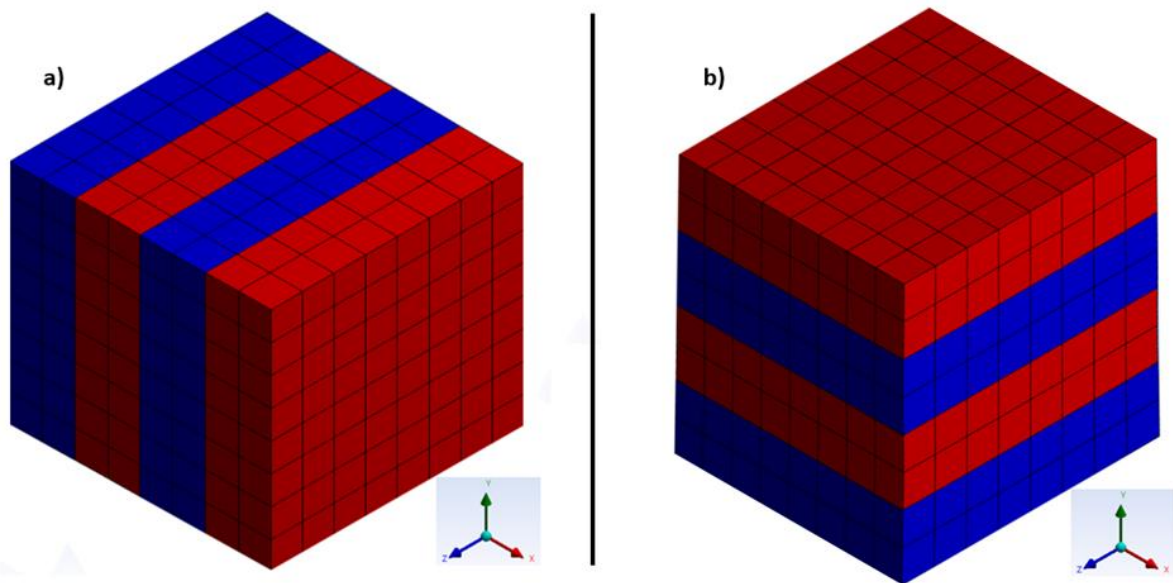


Figure 5.9 Two ANSYS models of Ti6Al4V α (blue) and β (red) phases together, a) columnar structure, b) row-by-row structure.

The following step in the simulation section was comparing modelling results and theoretical results, from the rule of mixtures approach, to validate the model, and gain confidence it would be comparable with the physical (real) samples. In the previous test, structures corresponding to the rule and inverse rule of mixtures were used to determine the upper and lower bounds respectively. In this stage the equations used for these estimates were used to compare to the modelling results for different proportions of the two phases. Firstly, the model material properties were divided 50:50 between α - phase and β -phase, arranged in structures corresponding to the two versions of the rule of mixtures, as shown in Figure 5.9, to eliminate any phase dominance in the model which could affect the comparison. Secondly, as shown in the Table 5.1 below, different strains were applied in the model to verify the elastic behaviour of the structures and determine the Young's modulus of the material. Finally, calculations of rule and inverse rule of mixtures were performed for the quoted values of the Young's modulus of the phases individually, and the results compared with the modelling results.

Table 5.1 The stresses results of axial loading and transverse loading on different strains to determine the elastic modulus E

Alignment type	Axial (↑↓)	Transverse (≡ α first)	Transverse (≡ β first)
Strain	Stress (MPa)	Stress (MPa)	Stress (MPa)
0.0005	36	31	31
0.001	72	62	62
0.0015	109	93	93
0.002	145	124	124
0.0025	181	156	156
0.003	217	187	187
0.0035	254	218	218
0.004	290	249	249
E (GPa)	72 GPa	62 GPa	62 GPa

• **Calculation of the rule and inverse rule of mixtures**

- **Axial loading**
$$E = fE_{\beta} + (1 - f)E_{\alpha} \quad (5.1)$$

where E_{β} is the young's modulus of Ti6Al4V β phase,

E_{α} is the young's modulus of Ti6Al4V α phase,

f is the volume fraction of β which is 0.5,

$$E = 0.5 (34.8) + 0.5 (108.62) = 71.8 \text{ GPa}$$

- **Transverse loading**
$$E = \left(\frac{f}{E_{\beta}} + \frac{1-f}{E_{\alpha}} \right)^{-1} \quad (5.2)$$

$$E = \left(\frac{0.5}{34.8} + \frac{0.5}{108.62} \right)^{-1} = 52.75 \text{ GPa}$$

Table 5.2 A comparison between FEM results and Theory calculations of Axial and Transverse loading.

	Axial ↑↓	Transverse ≡
FEM (Ansys)	72 GPa	62 GPa
Theory (Calculation)	71.8 GPa	52.75 GPa

From Table 5.2, the results of FEM and theory were found to be nearly matching in the axial loading comparison (the upper limit rule of mixtures configuration), but they were different in transverse loading (the inverse rule of mixtures structure). The difference between axial load and transverse load can be seen also in Table 5.1. The differences between the equations and the model could be due to the details captured by the FEM in aspects such as the effect of the lateral constraint of the expansion of the more compliant layers by the stiffer material; in the Rule of Mixtures equations, the blocks of material do not have any complex interaction, but the requirement that the cubes remain in contact at their connecting faces means that the deformation of the more easily deformed phase will be reduced, potentially leading to a higher overall stiffness. In the axial loading case, such constraint is less of an issue, as the deformation is limited directly by the load being carried by the stiffer phase, so the agreement is better. The reasonable match of the results between modelling and calculation (especially given that the rule of mixtures calculation is clearly simplistic, and the FEM may be more accurate to reality) in axial loading provided another proof of the model's validation and gave confidence to use this approach in further tests to simulate the real structure more precisely (in the form of a cube with cylindrical hole) and have insight to its mechanical properties.

5.4. Simulation of Block with Cylindrical Hole (Shape-C1)

In this section of FEM tests, the main aim was to simulate the real shapes that were experimentally fabricated and assessed in this project (see section 3.1 Figure 3.2) to have an insight to the mechanical behaviour of these shapes, and more particularly to gauge the effect of the microstructure on the mechanical properties. If basic microstructural changes of similar nature to those in the previous chapter in such parts could produce a perceptible change in the elastic behaviour, then it is likely that changes could be induced in lattices assembled from such elements were microstructural control to be exercised, but if no such changes could occur theoretically, then it would be less likely to be able to achieve these in practice.

Firstly, due the importance and known difference in the structure of the near edge area (as discussed in section 4.1) it was attempted to capture the effect of this phenomenon in this test by designing two different shapes, as shown in Figure 5.10 b&c. The shapes' sizes were redesigned to simulate the real structure (Figure 5.10a). In the real structure, the ratio between the diameter of the cylindrical hole and the side length of the overall cube was = 0.666 and this ratio was kept the same in the modelled structures. This aimed to create the same relative effect of the cylindrical structure on the cube and at the same time to allow comparison of the results of this test with the previous modelling of the solid cubic structure of 10×10×10 mm.

Secondly, in order to investigate the impact of microstructural differences, and possible preferred orientation in the near edge area only, the structure was modified to have cylindrical sleeve inside the hole, as shown in Figure 5.10b&c, which can be altered in thickness, stiffness matrix or orientation, to represent the near edge area (the green area in Figure 5.10) and also to change the orientation of this area easily without changing that of the entire structure. Two different thicknesses were used in this test to make a comparison and see the effect if one is present. The first structure had a cylinder with 0.67 mm wall thickness, as shown in Figure 5.10b, the second structure had a cylinder with 0.92 mm wall thickness, as shown in Figure 5.10c.

Finally, Ti6Al4V α phase only was the chosen material for modelling both structures (the cube with the hole and the cylindrical sleeve) because the results of EBSD mapping (4.1.1) showed that approx. 95% of the near edge area of the cylindrical structure was α phase (Figure 4.1), and this would capture the dominant effects that would occur in the real material.

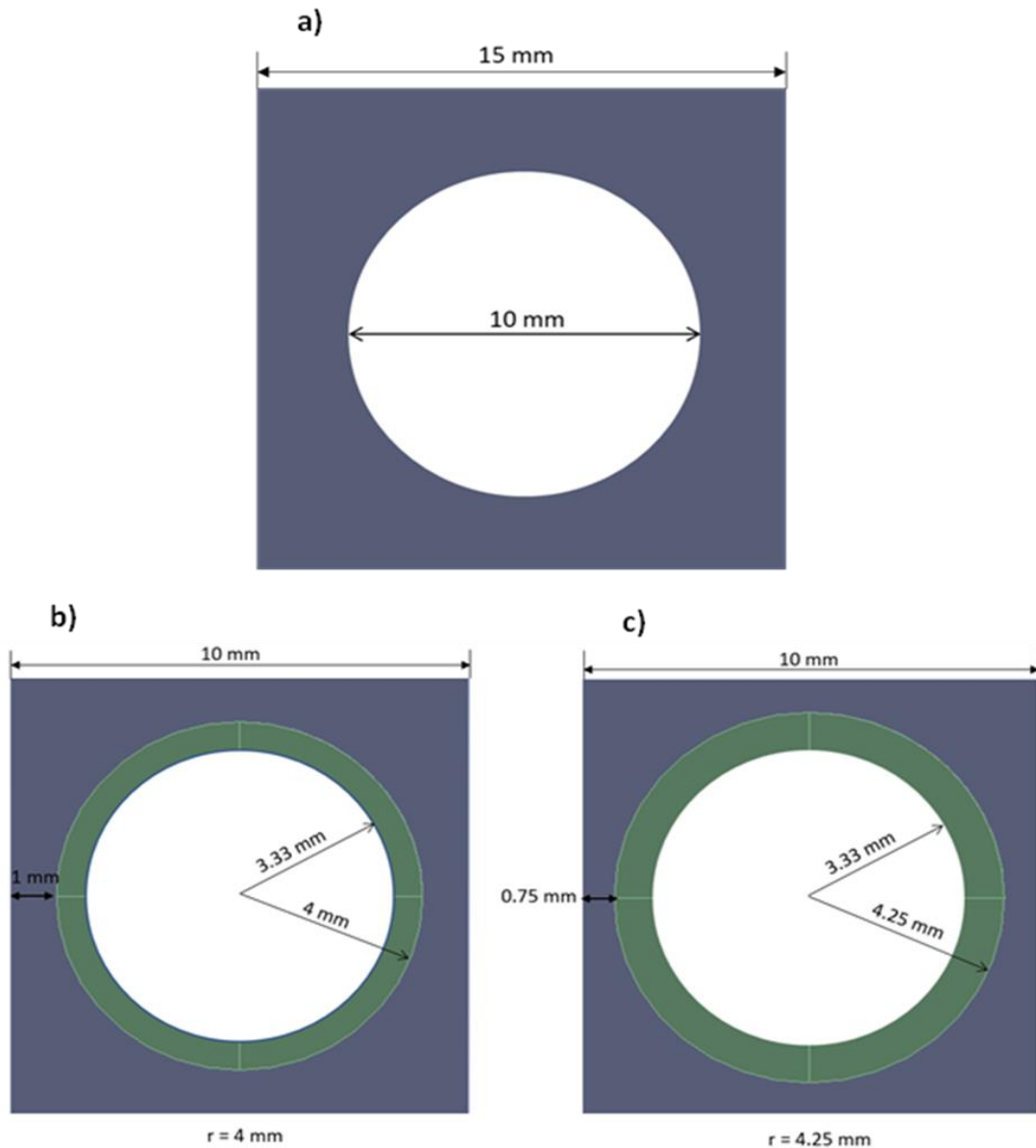


Figure 5.10 2D diagrams of solid cubes with cylinder hole, a) sketch with dimensions of the real sample produced by SLM, b and c) sketches with dimensions of FEM models showing the sleeve inside the cylinder hole (green circle).

Figure 5.11 and Figure 5.12 show the effect of grain orientation and near edge area size on the stiffness of the structures. The comparison shows the effect for both thicknesses, while the orientation of the crystal structure of the α phase within them is rotated on different axes (pitch and roll). In Figure 5.11, the two targeted areas (Green areas in Figure 5.10) are rotated on the pitch axis only, while the orientation of the rest of the structure remains with the c axis pointed towards up to represent the build direction of the real sample. The results showed the same stiffness behaviour in both thicknesses with only a small difference (≈ 1.5 GPa), being slightly higher stiffness for the larger near edge affected area. Similarly, Figure 5.12 shows the effect of the targeted areas being rotated on the roll axis only, while the rest of the structure has the crystal orientation with the c axis pointed towards up to represent the build direction of the real sample. The results also showed the same stiffness behaviour in both structures with little difference (≈ 0.75 GPa) with the larger near edge affected area being higher. In both cases, for both thicknesses, there can be a significant change in the modulus, with the variation from the highest to lowest stiffness orientation being about 10% for rotation around the pitch axis, and around 5% for rotation around roll. This is clear evidence that the orientation of the near edge area has the capacity to cause a direct influence on the stiffness of a structure containing free volume.

Additionally, by comparing the results of this test with the results of the solid cube made of Ti-6Al-4V α phase only, discussed in 5.2 (Figure 5.5 and Figure 5.6), the effect of this specific shape modification on the stiffness can be seen. The stiffness of shape-C1 at 0° was 44.3 GPa, while the stiffness of the solid cube at 0° was 108.75 GPa. The reduction of strength is obviously related to the presence of the hole in the middle, which supports no load and leads to concentration of the stress on the edges, as shown in Figure 5.13. The red colours represent the most highly stressed areas in the structure and give indication of the areas that would deform more, and would also be expected to fail earlier or start buckling. Were it to be intended to fabricate an actual porous material from a unit cell of this type, these areas would need to be reinforced with supports or have controlled texture to have maximum strength from the material.

Furthermore, the stiffness behaviour of Ti-6Al-4V α phase with rotation around the pitch axis is different between the solid cube and shape-C1, as shown in Figure 5.14. The difference occurs between angles of 60° and 120°; for the solid cube, the stiffness decreases from the maximum at 60° to 90° then increases to the maximum again at 120° (giving an “m” shape to the plot). On the other hand, in the case shape-C1, the stiffness increases to a maximum at 90° then decreases (giving a pyramidal shape). This difference is likely to arise as, in the case of the material with a hole, the rotation is only applied to the thin sleeve of material around the surface of the hole. It probably indicates that the effect of this layer is not in directly supporting the applied load, but rather in resisting the deformation of the surrounding material, which may not happen simply in the axial direction. In the case of the solid cube the resistance to elastic deformation is greatest when the high stiffness direction is directly opposed to the applied force, but in the presence of a hole it seems rather to be better when it is at about 45° to this, suggesting that this is an angle at which the sleeve of material resists the deformation of the structure (seen in exaggerated form in Figure 5.13) more effectively.

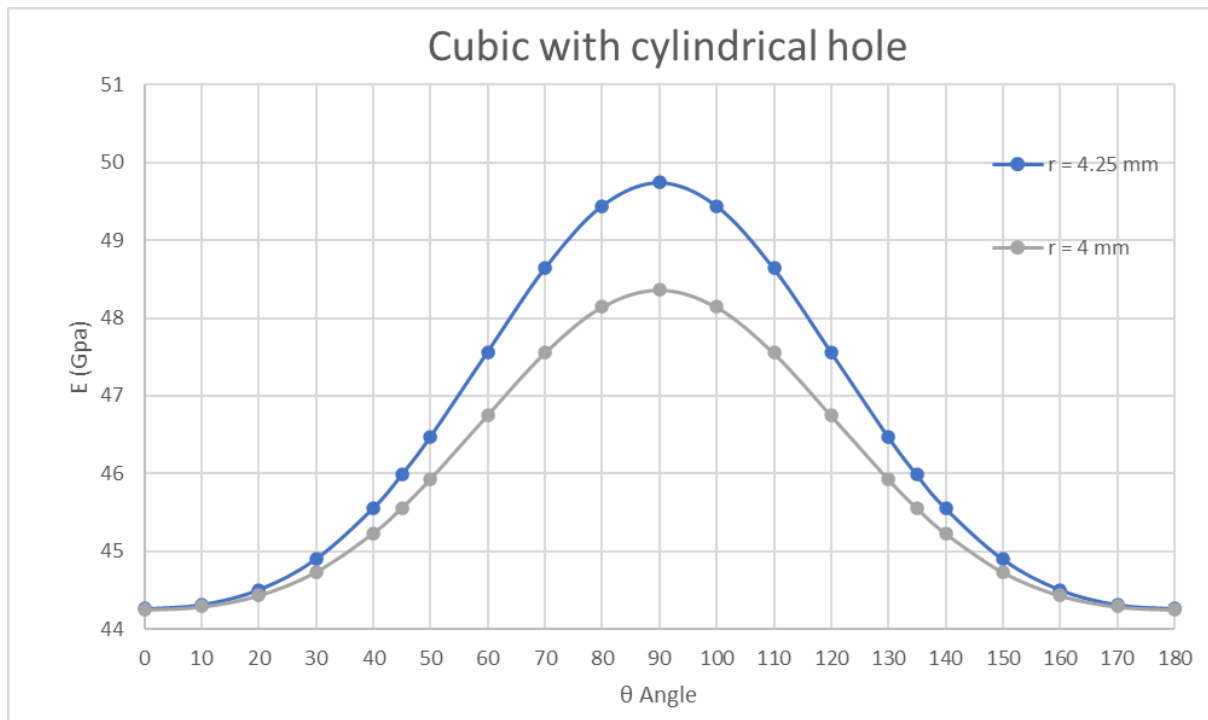


Figure 5.11 showed the results of stiffness (E) of Ti6Al4V for the two different cubes while the cylindrical rotates around Pitch axis. The blue line represents E of the structure of $r = 4.25\text{mm}$ cylindrical hole, the grey line represents E of the structure of $r = 4\text{mm}$ cylindrical hole.

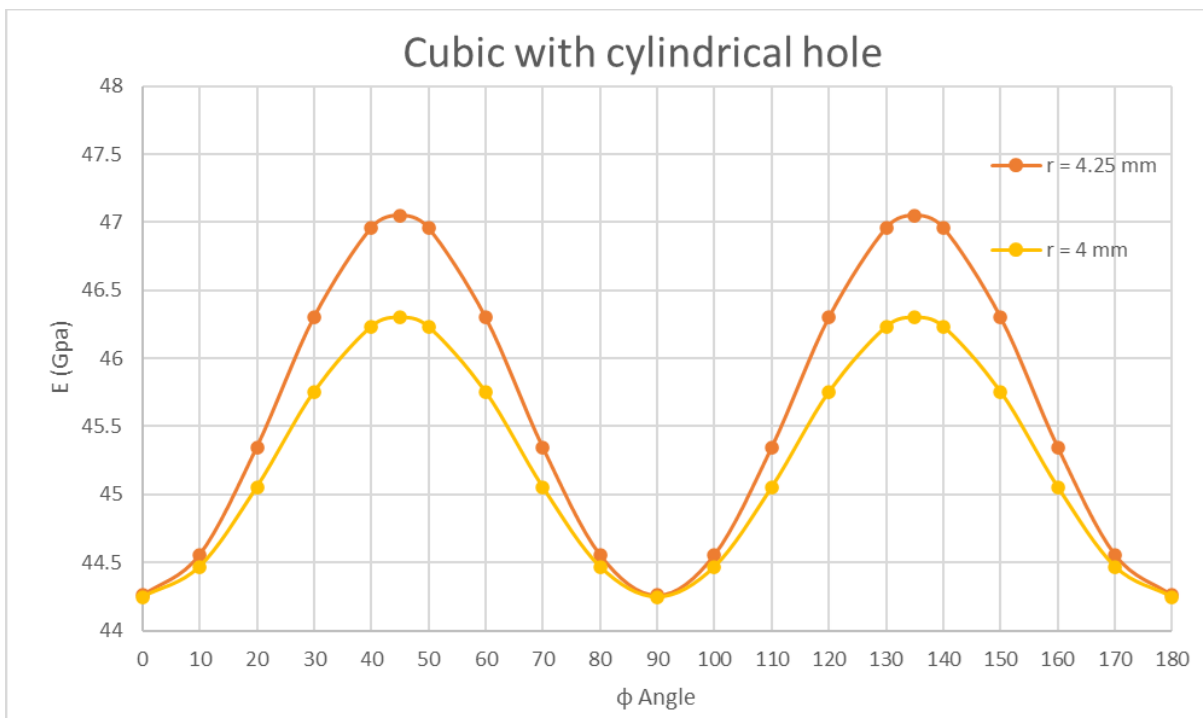


Figure 5.12 showed the results of stiffness (E) of Ti6Al4V for the two different cubes while the cylindrical rotates around Roll axis. The orange line represents E of the structure of $r = 4.25\text{mm}$ cylindrical hole, the yellow line represents E of the structure of $r = 4\text{mm}$ cylindrical hole.

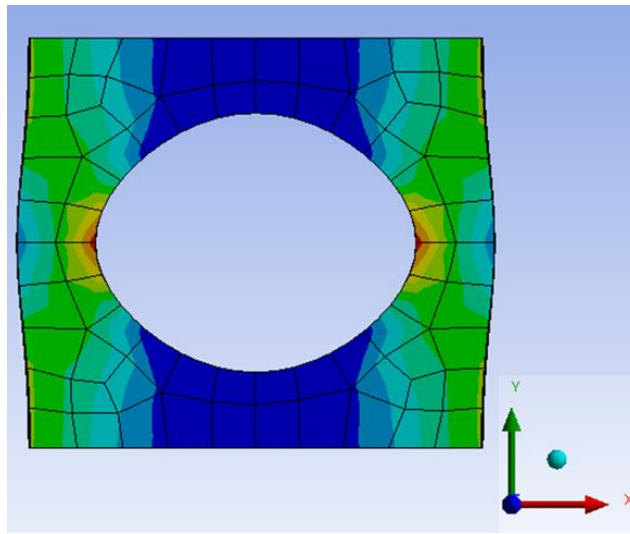


Figure 5.13 A front view of the model shows the stress areas in the structure. The colours indicates the levels of the stresses.

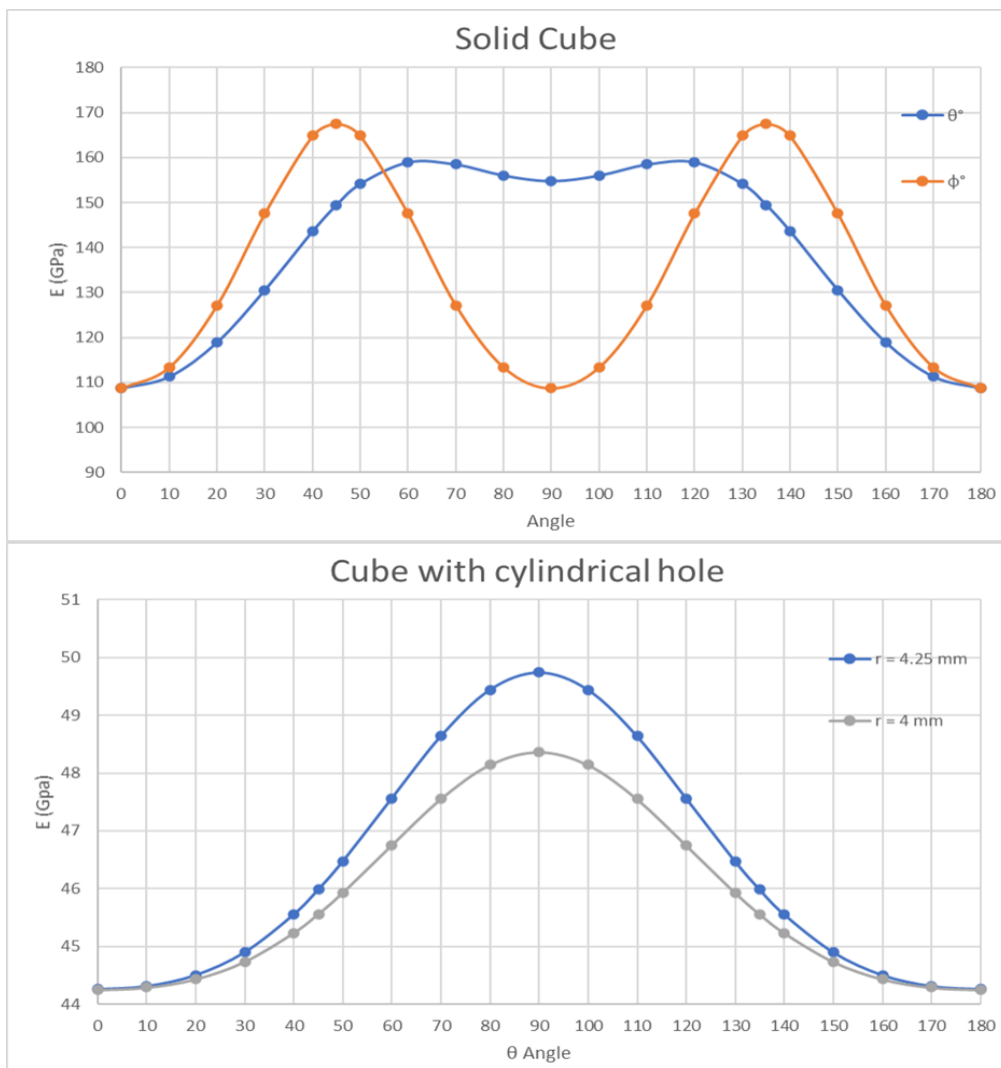


Figure 5.14 The stiffness behaviour comparison of Ti-6Al-4V of solid cube (above) and the cubes with a cylindrical hole (below) with rotation around the pitch axis.

5.5. Chapter Summary

The effect of degree of microstructural order on the elastic behaviour of Ti6Al4V has been studied in this chapter via the Finite Element Method (FEM). The objective was to build and validate a model to simulate and investigate the effect of microstructure orientation within real shapes containing free volume, corresponding to some of the structures produced in this project. The results presented in this chapter conclude to:

- 1- Changing the orientation of the crystal has an effect on the structure's stiffness. This effect is varied between the two phases α and β of Ti6Al4V. Changing orientation increased the stiffness of Ti6Al4V- α by 54% and 46% depending on axis rotation, while the improvement of Ti6Al4V- β stiffness was 131%. This could be due the difference between the hcp and the bcc structures of α and β .
- 2- The simulation results of shape-C1, which is a replication of one of the experimental samples, showed that the inner near edge area orientation is predicted to have an observable effect on the structure's stiffness. Furthermore, controlling the orientation to particular direction could increase the stiffness depending on the size of this area (large area = higher stiffness).

Chapter 6 : Mechanical Properties of Lattices

This chapter provides and discusses the results of the compressive response of the designed lattices. It begins with the structure selection process and the production issues encountered with the experimental manufacturing. Following this, investigation is reported of the effect of build orientation and post processing applied to a stretched diamond lattice, through mechanical properties acquired from compression testing. After this, the stiffness of the stretched diamond lattices developed and made here is used as the comparison factor between different build orientations (vertical and horizontal) or between as built and heat-treated specimens. Finally, a discussion is given of possible interpretation of the results.

6.1. Structure Definition

In the previous chapter it was demonstrated in a Finite Element simulation of a very much simplified structure that preferred orientations of the kind seen in additively manufactured Ti-6Al-4V could have an appreciable effect on the elastic properties of a structure. The purpose of this chapter is to develop a lattice structure that allows this effect to be tested in practice, as a basis for understanding the complementary influence of the mesostructure (lattice level) and the microstructure (material grain level) on the elastic properties. The first stage was to select a manufacturable structure that had a good chance of presenting the effect.

The selection process of a suitable structure aimed to design a structure with small struts and small thickness (maximising the amount of material that would be in the “near-surface” condition, and producing an overall low stiffness structure that would be easier to test) to capture the highlighted features from the microstructure results (see section 4.4). For example, if these struts could be oriented at a suitable angle to encourage β grains to grow up in the strut direction, instead of in the build direction and thus demonstrate control of texture could be used to influence properties.

Following the failed build attempts, which will discuss later, the design was changed to increase the confidence that it would be capable of completing the building process without any damage or failure. The new lattice design was a stretched diamond structure (i.e. the conventional diamond lattice structure as shown in Figure 6.1, but with the normally cubic unit cell distorted to be non uniform in 1 direction). The C axis of the unit cell was stretched (c/a ratio = 1.727) to change the strut angles to be two acute angles of 45° and two obtuse angles of 135° . The unit cell was repeated to build a specimen that was covered by two plates on the top and bottom, to provide an even surface for testing: these were of 1 and 2 mm on the top and bottom sides respectively. Two different sets were built: 1) vertical and 2) horizontal compared to the build direction, as shown in Fig 6.3 a & b. Similar to the previous design, this difference in orientation aimed to introduce two different angles based on build direction: 1) low angle “vertical shapes” and 2) high angle “horizontal shapes”, as shown in Figure 6.2 a & b. The build process for these lattice samples was successful, and a full set of samples was made (6 vertical and 6 horizontal). Half of each group (3) was heat treated to add another factor for examination. The heat treatment process was carried out under a high vacuum atmosphere with heating rate of $10^\circ\text{C}/\text{min}$ to 1050°C for 2 hours followed by furnace cooling [125]. A compression test was performed on each of the 12 samples and the results will be discussed in the next sections separately.

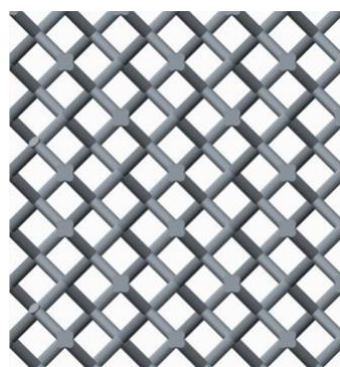


Figure 6.1 A conventional diamond lattice structure [126].

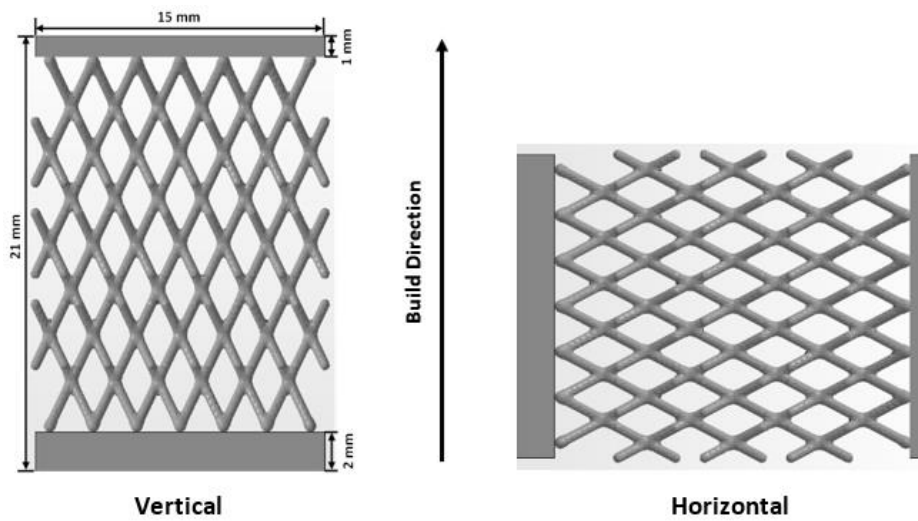


Figure 6.2 shows two different orientations of the stretched diamond lattices, vertical (left) and horizontal (right).

6.2. Compression Tests Results

Firstly, the lattices were divided depending on the build orientation and post process treatment into four groups with three samples in each: 1) As built vertical (AB-VER) lattices, 2) As built horizontal (AB-HOR) lattices, 3) Heat treated vertical (HT-VER) lattices, and 4) Heat treated horizontal (HT-HOR) lattices. All the samples were tested in the same direction along “the tall axis” of the samples to ensure the conditions are equal for all lattices and the results are comparable to each other, with the only variation being the difference in the microstructure caused by the build or heat treatment.

6.2.1. Compressive Response

Following the compression tests, an appropriate machine compliance and data correction were done (as the testing was performed on equipment not fitted with extensometry) and the stress-strain curves for all the samples were obtained. In all specimens, the stress-strain curves demonstrated a linear elastic region in the beginning, followed by a plastic region where eventually a reduction in stress occurred due to strut failure. Figure 6.3, Figure 6.4, Figure 6.5 and Figure 6.6 are examples of one curve from each of the four groups, indicating the 0.2% yield strength ($\sigma_{0.2}$) and ultimate compression

strength (UCS) for each case. Note that here the Ultimate Compression Strength is defined as an analogous property to the Ultimate Tensile Strength, as all samples showed an increase in supported load up to a maximum (the UCS) before fracture events led to collapse and failure of the sample. After that, a list of the yield strength and ultimate compression strength values for all the samples can be found in Figure 6.7.

The selection of specimens to present as examples of stress-strain curves was random, and demonstrates the process of determining values of yield strength and ultimate compressive strength for each group. The build orientation and heat treatment does not have a large influence on the yield strength and ultimate compressive strength of the presented samples. The as-built vertical (AB-VER) sample, as shown in Figure 6.3, has the highest yield strength and ultimate compressive strength (85.0 MPa and 99.5 MPa respectively), while the heat treated vertical (HT-VER) sample, as shown in fig 6.6, has the lowest values (80.0 MPa and 82.0 MPa respectively). All the as-built samples had higher ultimate compressive strength of at least 10% compared to heat treated versions. This could relate to the oxidation level of the heat-treated samples, which also affects the ductility and leads this to be slightly lower.

The average yield strength ($\sigma_{0.2}$) and ultimate compression strength (UCS) for each category are presented in Figure 6.7. There are two factors for comparing these results: 1) the build orientation (VER vs. HOR), and 2) As-built and post heat treatment (AB vs. HT). From figure 6.8, the build orientation does not seem have a significant influence on the yield strength and ultimate compression strength, neither where comparing in the as-built condition (AB-VER vs. AB-HOR) or after heat treatment (HT-VER vs. HT-HOR). On the other hand, the heat treatment does have a significant influence on the yield strength and ultimate compression strength where comparing the same build orientation. The ultimate strength decreased by 10% to 20% after heat treatment between (AB-VER vs. HT-VER) and (AB- HOR vs. HT-HOR) respectively, and the yield strength also decreased by 9% after heat treatment in the horizontal builds.

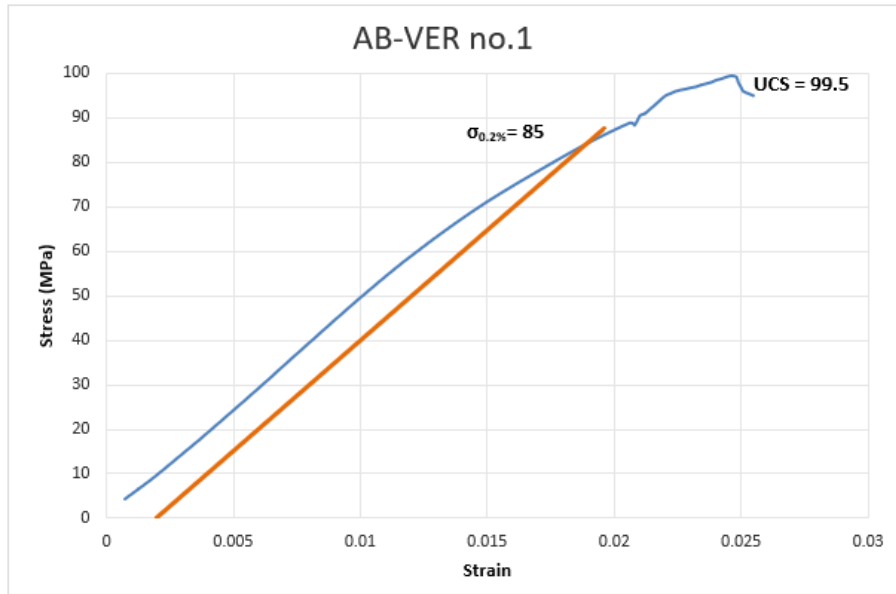


Figure 6.3 Illustrates stress/strain curve, showing ultimate compression strength (UCS) and 0.2% yield strength ($\sigma_{0.2}$) of the as-built vertical (AB-VER) sample no.1.

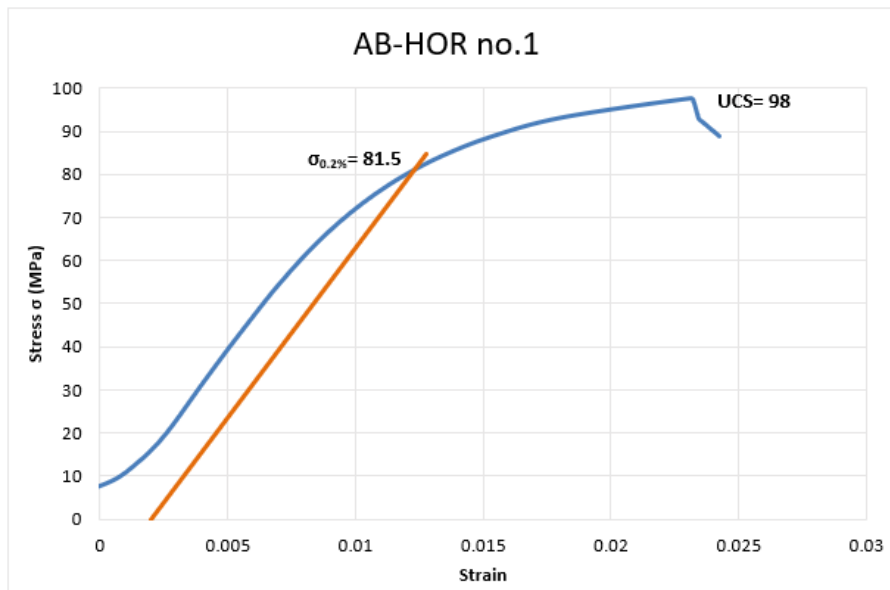


Figure 6.4 Illustrates stress/strain curve, showing ultimate compression strength (UCS) and 0.2% yield strength ($\sigma_{0.2}$) of the as-built horizontal (AB-HOR) sample no.1.

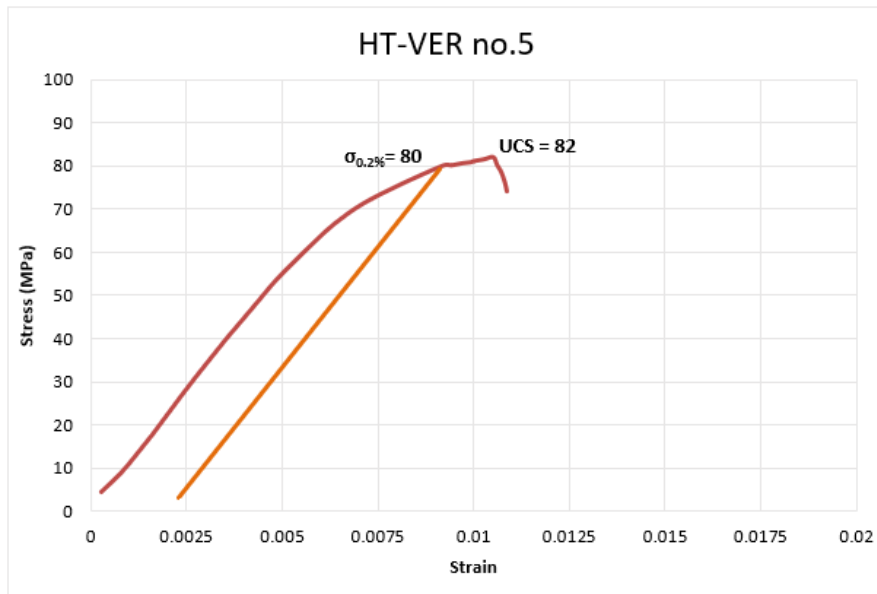


Figure 6.5 Illustrates stress/strain curve, showing ultimate compression strength (UCS) and 0.2% yield strength ($\sigma_{0.2}$) of the heat-treated vertical (HT-VER) sample no.5.

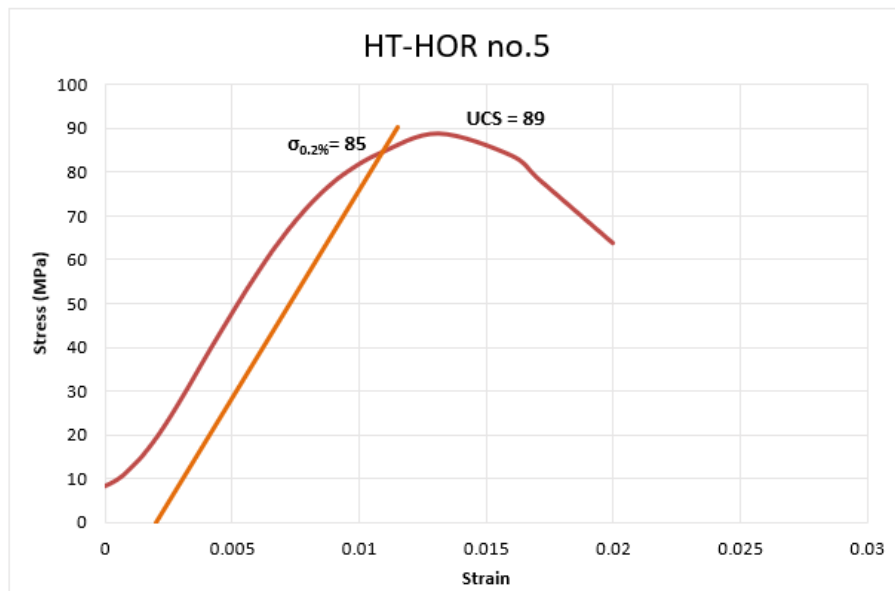


Figure 6.6 illustrates stress/strain curve, showing ultimate compression strength (UCS) and 0.2% yield strength ($\sigma_{0.2}$) of the heat-treated horizontal (HT-HOR) sample no.5.

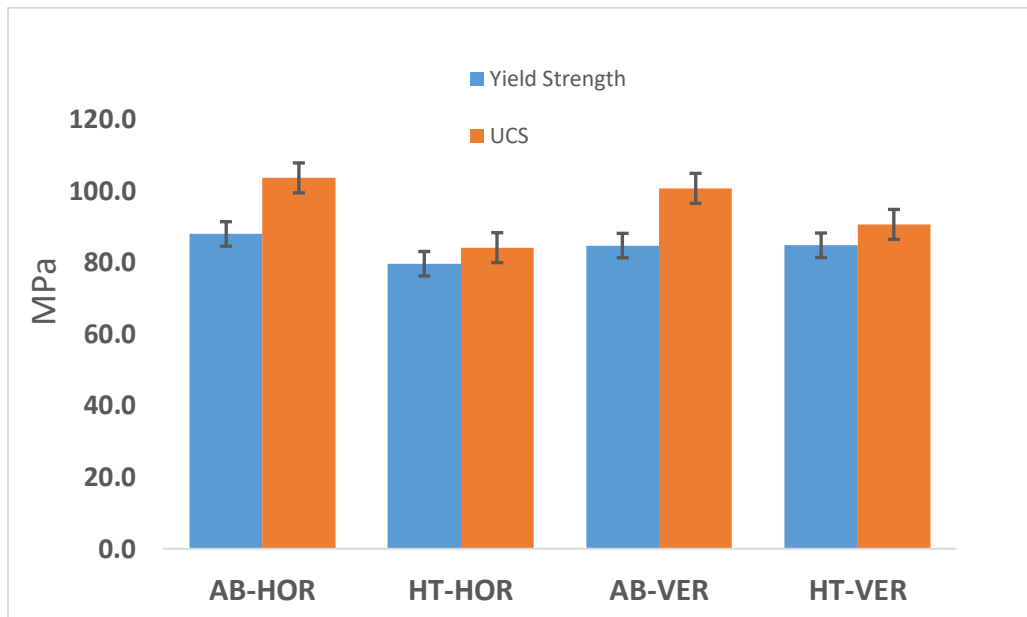


Figure 6.7 Illustrates average of ultimate compression strength (UCS) and 0.2% yield strength ($\sigma_{0.2}$) of the as-built horizontal (AB-HOR), heat-treated horizontal (HT-HOR), as-built vertical (AB-VER) and heat-treated vertical (HT-VER).

In Table 6.1, a comparison of yield strength ($\sigma_{0.2}$) values with different designed lattice structures manufactured by EBM and SLM from literature [127-132]. In general, the strength values increased when the relative density (ρ^*/ρ_s) of the lattices increased, as shown in Figure 6.8. This increase could be justified by Gibson and Ashby's model [133], which leads to the general result that the mechanical properties of cellular structures scale with the relative density to a certain power, at least for the case where the structural elements deform by bending. The yield strength and relative density relationship is $\sigma_y \propto \bar{\rho}^{3/2} \sigma_{YS}$, where σ_{YS} is the yield strength of the solid parent, which is 1070 MPa [5] and $\bar{\rho}$ is the relative density of the structure.

The range of yield strength ($\sigma_{0.2}$) values of "stretched" diamond structure was from 84.80 to 88.00 MPa for both heat treatments (as-built and heat-treated) and it was in agreement with the prediction of Gibson and Ashby's model. It is slightly higher than other diamond lattices except for the heat-treated diamond lattice reported by Wauthle et al. [132], which is a higher strength due to having a higher relative density (30%). Overall, the results of the different samples explored in this study were very similar to each other regardless of the heat treatment or the build orientation, and were also similar to other lattices from the literature, despite significant differences in the structural form of those

lattices. As the goal of this project was not to explore the stretched diamond lattice in its own right, variations in density were not explored.

Table 6.1 Comparison of the Yield Strength ($\sigma_{0.2}$) of Ti6Al4V lattices manufactured by AM processes.

Lattice design	Relative density (%)	AM process	$\sigma_{0.2y}$ (MPa)	Ref.
Hexagonal	11.00	EBM	8.78	[128]
FCC*	12.40	SLM	47.00	[129]
Cubic	13.29	SLM	14.06	[127]
Diamond	18.90	EBM	29.30	[130]
Diamond	21.00	SLM	43.00	[131]
Hexagonal	25.81	SLM	39.39	[127]
Diamond (As-Built)	30.00	SLM	75.00	[132]
Diamond (Heat-Treated)	30.00	SLM	90.00	[132]
Diamond (AB-HOR)	26.15	SLM	88.00	This work
Diamond (AB-VER)	25.92	SLM	84.80	This work
Diamond (HT-HOR)	26.19	SLM	79.70	This work
Diamond (HT-VER)	25.84	SLM	84.80	This work

* Quasi-static compression test

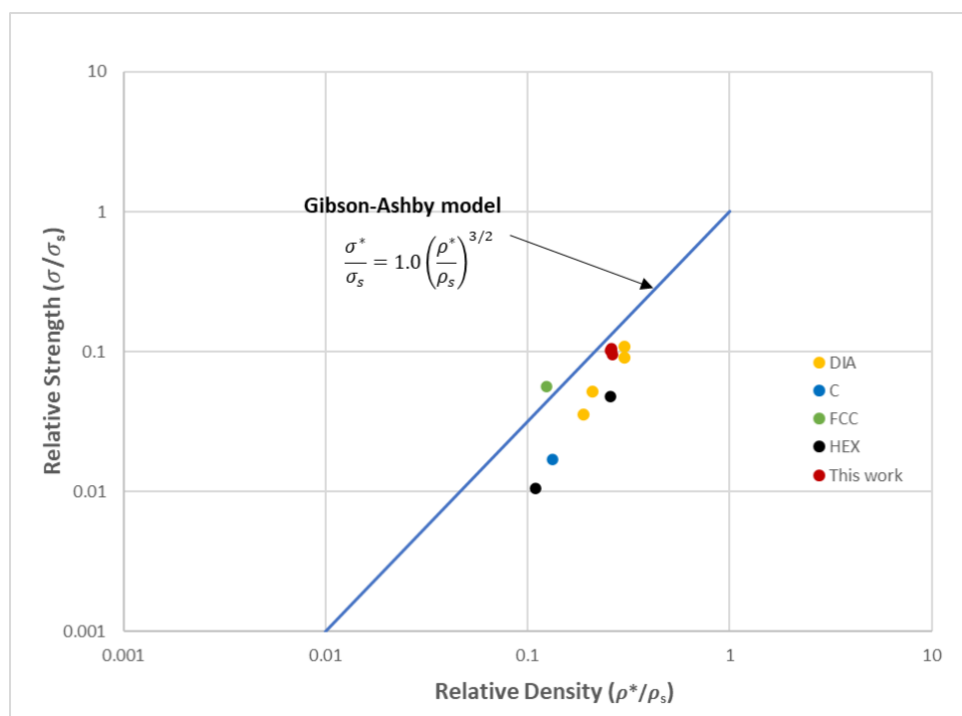


Figure 6.8 Comparison of reported data in Table 6.1 with predictions of the Gibson-Ashby model.

6.2.2. Elastic Properties

To complete the comparison of the mechanical properties between build orientations and post heat treatments, the stiffness, which is represented by the Young's modulus (E), has been calculated as an average of the three specimens in each category (AB-VER, AB-HOR, HT-VER, HT-HOR). It is clear from the results displayed in Figure 6.9 that the heat treatment process increases the stiffness of both build orientations (HT-VER and HT-HOR) and the values of both orientations in the heat treated condition are nearly equal (10.27 ± 0.66 GPa and 10.13 ± 0.49 GPa, respectively). In contrast, there is a significant difference in stiffness values between as-built samples in different orientations (AB-VER and AB-HOR). The stiffness of vertical build orientation samples (AB-VER) (4.42 ± 0.58 GPa) is slightly more than half (52%) the stiffness of horizontal build orientation samples (AB-HOR) (8.37 ± 0.56 GPa).

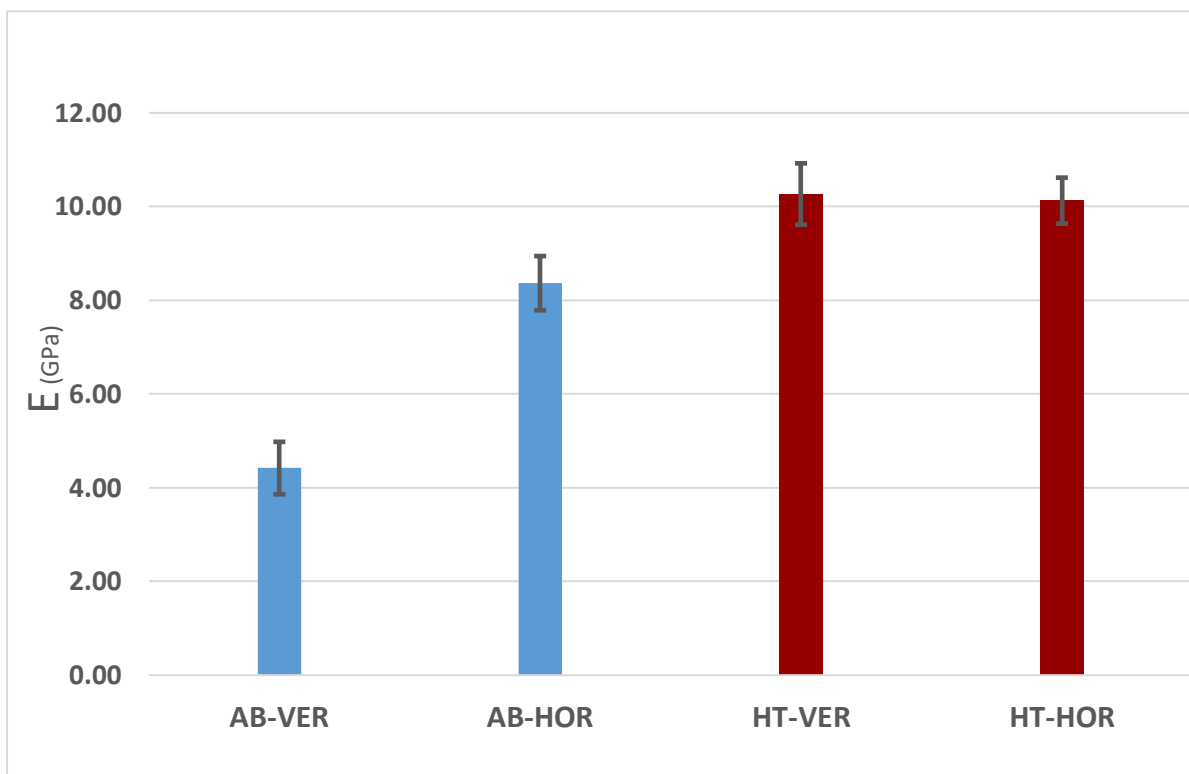


Figure 6.9 Illustrates average of Elastic modulus (E) of the as-built horizontal (AB-HOR), heat-treated horizontal (HT-HOR), as-built vertical (AB-VER) and heat-treated vertical (HT-VER).

In Table 6.2, another comparison of the stiffness (E) values with different designed lattice structures from literature [75, 130-132]. As expected, as the strength results, the stiffness values also increased when the relative density (ρ^*/ρ_s) of the lattices increased, as shown in Figure 6.10. The elastic modulus and relative density relationship follows the Gibson and Ashby model [133] for cellular structures, $E^* \propto \bar{\rho}^2 E_s$, where E_s is the elastic modulus of the solid parent, which is 114 GPa [5] and $\bar{\rho}$ is the relative density of the structure.

The stiffness values of “stretched” diamond structure were in agreement with the prediction of Gibson and Ashby’s model. It is notable that the heat-treated results were slightly above the expectations, which related to the anisotropy of $\alpha+\beta$ mixture after the heat treatment. The as-built results affected by the build orientations (horizontal or vertical). This difference between as-built results is highly likely connected to the microstructure’ orientation, which is in this case “build orientation”.

Table 6.2 Comparison of the elastic modulus of Ti6Al4V lattices manufactured by AM processes.

Lattice design	Relative density (%)	AM process	E (GPa)	Ref.
Cubic	23.40	SLM	5.50	[75]
Diamond (//)	18.90	EBM	1.60	[130]
Diamond (⊥)	19.20	EBM	0.90	[130]
Diamond	22.00	SLM	1.48	[131]
Diamond (As-Built)	30.00	SLM	2.68	[132]
Diamond (Heat-Treated)	30.00	SLM	3.22	[132]
Diamond (AB-HOR)	26.15	SLM	8.37	This work
Diamond (AB-VER)	25.92	SLM	4.42	This work
Diamond (HT-HOR)	26.19	SLM	10.13	This work
Diamond (HT-VER)	25.84	SLM	10.27	This work

(//) the sample tested parallel to the build direction.

(⊥) the sample tested perpendicular to the build direction.

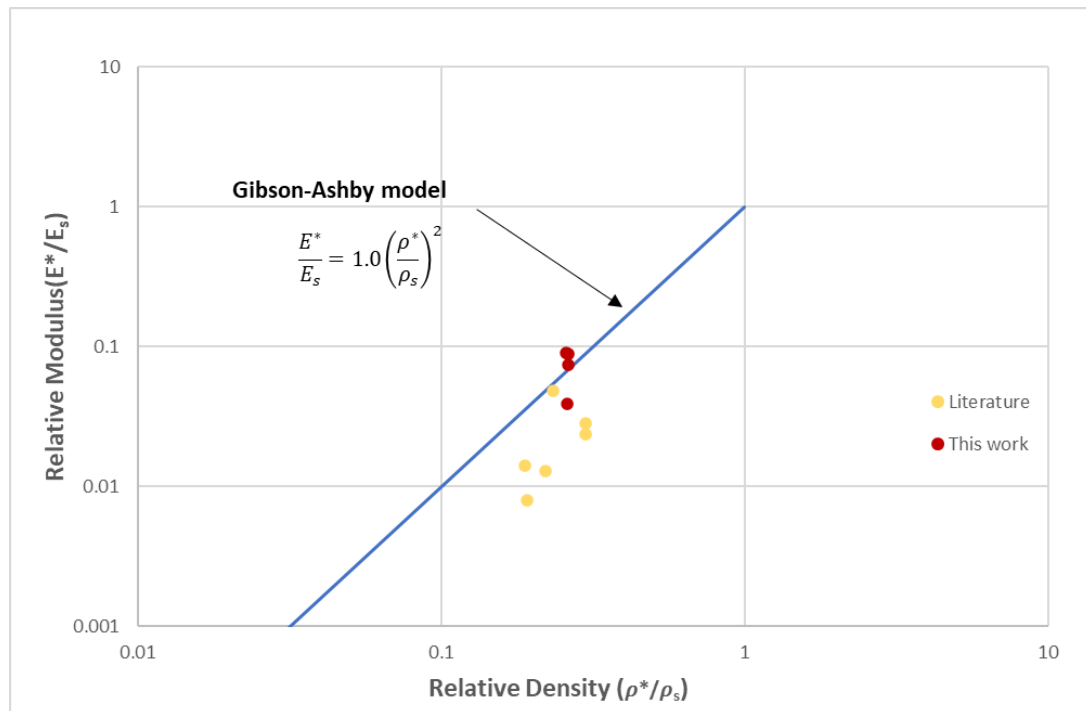


Figure 6.10 Comparison of reported data in table 6.2 with predictions of the Gibson-Ashby model.

6.3. Discussion

A triple helix structure was first chosen to maximise the investigation area (the amount of angled strut), as shown in Figure 6.11. The helix angle was 40° and the thickness was 0.6 mm to allow the microstructure and the texture to nucleate and to propagate through the layers as additional ones are built up (through the selection of angle) and to ensure that the bulk texture did not develop (through the selection of thickness). The helices were covered by two plates: 1 and 2 mm from the top and bottom sides respectively to facilitate testing by providing a clear and flat top and bottom surface where forces could be applied. A triple helix was chosen in order that the overall structure was more balanced (i.e. was less likely to bend to one side on compression), and mechanically stronger than a single or double helix would be, while still allowing enough space between the helices so they could deform elastically without impinging on each other. Two different sets were built: 1) vertical and 2) horizontal, as shown in Figure 6.11 a & b; this change aimed to add another factor to the investigation by creating two different angles of growth: a low angle to the build

direction (vertical) and a high angle to the build direction (horizontal). All structures were supported with additional solid elements in the build file to try to prevent collapse during the building process. Unfortunately, after production all the samples were found to be damaged, and the building process was unsuccessful because the helix thickness (0.6 mm) was too small to hold the upper plate, even with the support structures. Also, due to the complex design, some of the support parts melted and fused to the interior parts, as shown in Figure 6.12.

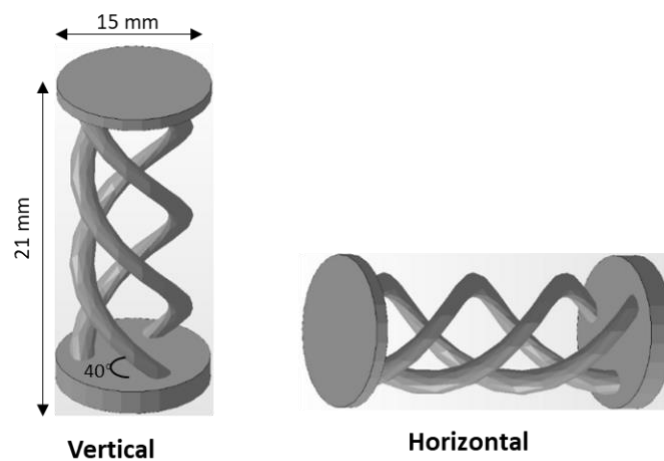


Figure 6.11 Two different orientations of the helix structure design, vertical (left) and horizontal (right).



Figure 6.12 A failed sample of the vertical helix design.

The chosen lattice structure of a “stretched diamond cell” has been used in two different build orientations (vertical and horizontal) and two different heat treatments (as-built and heat-treated) resulting in four different combinations to test and evaluate. The structure’s

dimensions and the build parameters are unchanged, to eliminate any other effect on the results, such as the relative density or layer thickness, and maintain the focus on the effect of microstructure. Firstly, changing the build orientation of the samples from vertical to horizontal does not have a significant influence on the mechanical properties in terms of yield strength and ultimate compression strength, as shown in Figure 6.7. While the heat-treated samples show a slight decrease in the yield strength and ultimate compression strength of both build orientations (HT-HOR and HT-VER) compared with as-built samples (AB-VER, AB-HOR), as shown in Figure 6.7. The plastic properties may need to involve multiple slip systems to operate and therefore be less susceptible to oriented microstructures in the lattice. The heat-treated samples, as shown in Figure 6.13, were partially oxidized during the heat treatment process and this oxidization is believed to increase the brittleness of the structure, which led to cracking occurring more easily and this lowered the measured ultimate compression strength (as the material fails earlier, after less plastic deformation and so less load increase), with relatively little effect on the yield strength. Secondly, the effect of heat treatment on the stiffness was clear from Figure 6.9, the heat-treated samples were substantially stiffer than the as-built samples in both build orientations (vertical and horizontal). This must be related to the change in the microstructure during the heat treatment process. While the pickup of oxygen can affect the strength, it should not affect the stiffness significantly. The temperature during the heat treatment (1000 °C) was sufficient to transform α' into a mixture of $\alpha+\beta$. After changing the microstructure of the samples, the effect of build orientation was insignificant, as shown in fig 6.9 (HT-VER and HT-HOR). On the other hand, there was a clear difference (almost double) between the vertical and horizontal orientations of as-built samples. This difference is highly likely to be related to the microstructure alignment in the samples, because all the other variable factors had been eliminated by the design, production, or heat treatment. The alignment of prior β grains is likely to be along the build direction, which causes the noticeable difference between the vertical and horizontal as-built samples, as the differing angle the struts present to the build direction will affect how easily the grains can grow along the struts, and how much the columnar structure is interrupted by the nucleation of new grains. As shown in Figure 6.2, the vertical strut is at an angle of 45° away from the build

direction, while the horizontal strut is at an angle 135° away from the build direction and this creates the difference in the microstructure. It is evident that when the alignment produced in the as-built samples is present in this particular structure, the effect of the crystallographic anisotropy in elastic properties is that the stiffness properties of the lattice are lower. The randomised orientation that forms on heat treatment is superior from a stiffness point of view, as the preference for a more compliant orientation is lost. While the as-built version of the structure is in this case less likely to be desirable for applications, this is a clear demonstration that the orientation of the built microstructure can have an effect on properties measured at the mesoscopic lattice level.

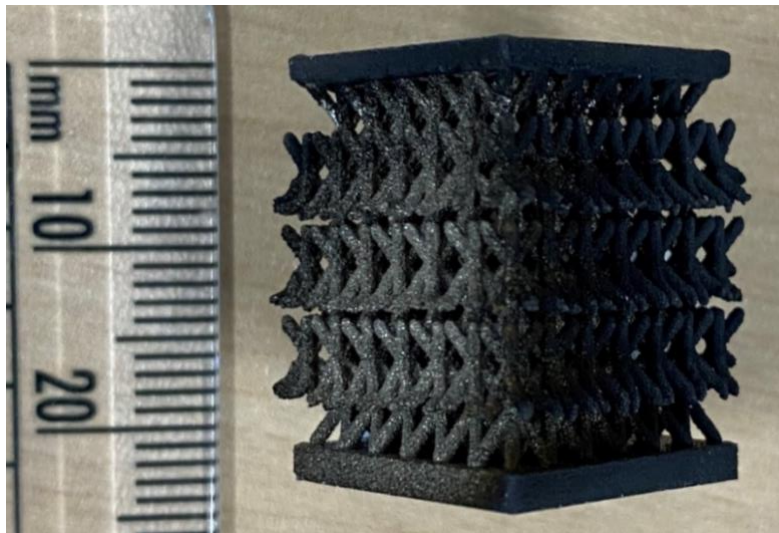


Figure 6.13 A picture of one the heat-treated samples show the oxidation (black on the right)

6.4. Chapter Summary

The compressive response of stretched diamond lattices has been examined in this chapter. The objective was to investigate the effect of the microstructure of particular designed lattices on the mechanical properties. The build orientation and post processing treatment were factors that used to change the microstructure. The results presented in this chapter find the following:

- 1- The yield strength and ultimate compression strength are not affected by the build orientation or heat treatment significantly.
- 2- The stiffness of the structure was clearly influenced by both the heat treatment and build orientation. The heat treatment enhanced the stiffness of the lattices along the tested direction for both orientations (VER and HOR). This is likely to have come about as the crystallographic impact was eliminated by changing the microstructure of the lattices.
- 3- The stiffness of the as-built lattices was lower because it is affected by the preferred orientation of the microstructure.
- 4- The build orientation of the as-built lattices has a clear influence on the stiffness, this could be caused by the directed microstructure of the structure.

Chapter 7 : Conclusions and Future Work

7.1. Conclusions

In this thesis, the effect of mesostructure on the microstructure of Ti-6Al-4V lattice structures manufactured by Selective Laser Melting (SLM), and the effect of both of these on the mechanical properties, are assessed. A number of different features such as change in thickness, curvature, and build angle have been recreated in sample structures to allow investigation of the relationship between the structure and the microstructure. The knowledge from this was used to select and build a test structure, and the mechanical properties (in particular the elastic behaviour) of the new structures were examined under compressive loading to have better understanding of the link between the structure, microstructure and the mechanical properties. Finally, a numerical model was developed and validated to understand and evaluate the role of the microstructure on the mechanical properties. This work concluded with the following remarks:

7.1.1. The effect of component shape on the microstructure

- The microstructure of most investigated areas is α' martensitic laths within prior columnar β grains as expected, the columnar β grains grow in the build direction \uparrow , and most these areas suffer from significant surface roughness.
- In the overhang areas, especially near the inner surface, the microstructure was slightly different, being equiaxed $\alpha + \beta$ rather than columnar. This could be related to the thermal gradient at the melt pool and how new layers deposit over cold powder.
- The curved surface forced the columnar β grains at lower angle to grow inclined into the structure direction instead of the build direction \uparrow .

- The inclined structures did not show any effect on the microstructure regardless of the inclination degree or the wall thickness.

7.1.2. The mechanical properties of lattices

- Neither the build orientation nor the heat treatment has a significant impact on the strength properties of designed structure. However, the stiffness of these structures influenced by both build orientation and heat treatment.
- The stiffness of the structures was clearly influenced by both the heat treatment and build orientation. The heat treatment enhanced the stiffness of the lattices for both orientations vertically and horizontally, and this is likely to the crystallographic impact was eliminated by changing the microstructure of the lattices.
- The build orientation has a clear influence on the stiffness of as-built lattices, this is highly likely to related to the microstructure alignment because all the other factors are eliminated (shape, production, and heat treatment).
- The crystallographic anisotropy has a direct link to enhance the stiffness of these such structures.

7.1.3. The effect of degree of microstructural order on the elastic behaviour.

- Using Finite Element Model (FEM) revealed that simulation has the capability to capture some important features seen due to the complexity of real structures on simple and small scale.
- Changing orientation of the crystal has an impact on the structure's stiffness. This was clear by simulating the inner near surface area, allocating a random orientation, resulting in stiffness increase.

Finally, this work demonstrates the relationship between the mesostructure and the microstructure, and their influence on the mechanical properties through directing the crystallography to specific orientation which lead to improvement in the stiffness which is comparable to post treatment results.

7.2. Future Work

The effect of mesostructure on the microstructure and the mechanical properties has successfully been investigated in this work. However, there are a few areas that need to be further developed and some questions raised during this project which need to be answered in the future. The main points are:

- It was clear in this work that controlling the alignment of prior β grains through certain structural designs can lead to enhancement of the stiffness of the structure. However, there are many different possible lattice designs, unit cell sizes and strut thicknesses, which could not be widely explored in this work. different structures and shapes with different strut dimensions need to be designed and explored either computationally or experimentally.
- Using the Finite Element Model (FEM) in this project was successful to capture and simulate the real features of interest from the original samples. Furthermore, these simulations can be taken to another level as prediction tool for complicated structures (for example to assist in the study above), and thereby maximise the benefits by selecting the suitable lattice types for particular application requirements before the production.

REFERENCES

1. Leyens, C. and M. Peters, *Titanium and titanium alloys: fundamentals and applications*. 2003: John Wiley & Sons.
2. Donachie, M.J., *Titanium: a technical guide*. 2000: ASM international.
3. Breme, J., E. Eisenbarth, and V. Biehl, *Titanium and its alloys for medical applications*. *Titanium and Titanium Alloys: Fundamentals and Applications*, 2003: p. 423-451.
4. Lütjering, G. and J.C. Williams, *Beta Alloys*. 2007: Springer.
5. ASTM. *Standard Specification for Titanium and Titanium Alloy Strip, Sheet, and Plate*. 2011. American Society for Testing Materials.
6. Joshi, V.A., *Titanium alloys: an atlas of structures and fracture features*. 2006: Crc Press.
7. Ahmed, T. and H. Rack, *Phase transformations during cooling in α + β titanium alloys*. *Materials Science and Engineering: A*, 1998. **243**(1-2): p. 206-211.
8. Banerjee, S. and P. Mukhopadhyay, *Phase transformations: examples from titanium and zirconium alloys*. Vol. 12. 2010: Elsevier.
9. Semiatin, S. and T. Bieler, *The effect of alpha platelet thickness on plastic flow during hot working of Ti-6Al-4V with a transformed microstructure*. *Acta materialia*, 2001. **49**(17): p. 3565-3573.
10. Welsch, G., R. Boyer, and E. Collings, *Materials properties handbook: titanium alloys*. 1993: ASM international.
11. Markaki, A. and A. Justin, *A magneto-active scaffold for stimulation of bone growth*. *Materials Science and Technology*, 2014. **30**(13): p. 1590-1598.
12. Wu, G., C. Shi, W. Sha, A. Sha, and H. Jiang, *Effect of microstructure on the fatigue properties of Ti-6Al-4V titanium alloys*. *Materials & Design*, 2013. **46**: p. 668-674.
13. Wanjara, P. and M. Jahazi, *Linear friction welding of Ti-6Al-4V: processing, microstructure, and mechanical-property inter-relationships*. *Metallurgical and Materials Transactions A*, 2005. **36**(8): p. 2149-2164.
14. Wanying, L., L. Yuanhua, C. Yuhai, S. Taihe, and A. Singh, *Effect of Different Heat Treatments on Microstructure and Mechanical Properties of Ti6Al4V Titanium Alloy*. *Rare Metal Materials and Engineering*, 2017. **46**(3): p. 634-639.
15. Sieniawski, J., W. Ziąja, K. Kubiak, and M. Motyka, *Microstructure and mechanical properties of high strength two-phase titanium alloys*, in *Titanium alloys-advances in properties control*. 2013, InTech.
16. Seshacharyulu, T., S. Medeiros, W. Frazier, and Y. Prasad, *Hot working of commercial Ti-6Al-4V with an equiaxed α - β microstructure: materials modeling considerations*. *Materials Science and Engineering: A*, 2000. **284**(1-2): p. 184-194.
17. Nalla, R., R. Ritchie, B. Boyce, J. Campbell, and J. Peters, *Influence of microstructure on high-cycle fatigue of Ti-6Al-4V: bimodal vs. lamellar structures*. *Metallurgical and materials transactions A*, 2002. **33**(3): p. 899-918.
18. Bache, M. and W. Evans, *Impact of texture on mechanical properties in an advanced titanium alloy*. *Materials Science and Engineering: A*, 2001. **319**: p. 409-414.

19. Weaver, M. and H. Garmestani, *Microstructures and mechanical properties of commercial titanium foils processed via the melt overflow process*. Materials Science and Engineering: A, 1998. **247**(1-2): p. 229-238.
20. Verlinden, B., J. Driver, I. Samajdar, and R.D. Doherty, *Thermo-mechanical processing of metallic materials*. Vol. 11. 2007: Elsevier.
21. Kalinyuk, A., N. Trigub, V. Zamkov, O. Ivasishin, P. Markovsky, R. Teliovich, and S. Semiatin, *Microstructure, texture, and mechanical properties of electron-beam melted Ti-6Al-4V*. Materials Science and Engineering: A, 2003. **346**(1-2): p. 178-188.
22. Hull, C.W., *Apparatus for production of three-dimensional objects by stereolithography*. 1986, Google Patents.
23. Murr, L., S. Quinones, S. Gaytan, M. Lopez, A. Rodela, E. Martinez, D. Hernandez, E. Martinez, F. Medina, and R. Wicker, *Microstructure and mechanical behavior of Ti-6Al-4V produced by rapid-layer manufacturing, for biomedical applications*. Journal of the mechanical behavior of biomedical materials, 2009. **2**(1): p. 20-32.
24. Lancaster, R., G. Davies, H. Illsley, S. Jeffs, and G. Baxter, *Structural integrity of an electron beam melted titanium alloy*. Materials, 2016. **9**(6): p. 470.
25. Kruth, J.-P., *Comparison of CO₂ and Nd-YAG lasers for user with Selective Laser Sintering of Steel-Copper powders*, *International Journal of CAD/CAM and Computer Graphics*, 1998. **13**(4): p. 95-110.
26. Kruth, J.-P., *Material in-process manufacturing by rapid prototyping techniques*. CIRP Annals-Manufacturing Technology, 1991. **40**(2): p. 603-614.
27. ASTM, *Standard terminology for additive manufacturing technologies*. 2012: ASTM International.
28. Gibson, I., D. Rosen, and B. Stucker, *Development of Additive Manufacturing Technology*, in *Additive Manufacturing Technologies: 3D Printing, Rapid Prototyping, and Direct Digital Manufacturing*. 2015, Springer New York: New York, NY. p. 19-42.
29. Karunakaran, K., S. Suryakumar, V. Pushpa, and S. Akula, *Low cost integration of additive and subtractive processes for hybrid layered manufacturing*. Robotics and Computer-Integrated Manufacturing, 2010. **26**(5): p. 490-499.
30. Moylan, S., J. Slotwinski, A. Cooke, K. Jurrens, and M.A. Donmez, *An additive manufacturing test artifact*. Journal of research of the National Institute of Standards and Technology, 2014. **119**: p. 429.
31. Deckard, C.R., *Method and apparatus for producing parts by selective sintering*. 1989, Google Patents.
32. Van Bael, S., B. Vandenbroucke, G. Kerckhofs, J. Schrooten, and J.-P. Kruth. *Design and production of bone scaffolds with selective laser melting*. in *TMS 2009*. 2009.
33. Thijs, L., F. Verhaeghe, T. Craeghs, J. Van Humbeeck, and J.-P. Kruth, *A study of the microstructural evolution during selective laser melting of Ti-6Al-4V*. Acta materialia, 2010. **58**(9): p. 3303-3312.
34. Zhang, D., S. Sun, D. Qiu, M.A. Gibson, M.S. Dargusch, M. Brandt, M. Qian, and M. Easton, *Metal Alloys for Fusion -Based Additive Manufacturing*. Advanced Engineering Materials, 2018: p. 1700952.

35. Wycisk, E., S. Siddique, D. Herzog, F. Walther, and C. Emmelmann, *Fatigue performance of laser additive manufactured Ti–6Al–4V in very high cycle fatigue regime up to 10⁹ cycles*. *Frontiers in Materials*, 2015. **2**: p. 72.
36. Kempen, K., B. Vrancken, S. Bols, L. Thijs, J. Van Humbeeck, and J.-P. Kruth, *Selective laser melting of crack-free high density M2 high speed steel parts by baseplate preheating*. *Journal of Manufacturing Science and Engineering*, 2014. **136**(6): p. 061026.
37. Zhang, B., L. Dembinski, and C. Coddet, *The study of the laser parameters and environment variables effect on mechanical properties of high compact parts elaborated by selective laser melting 316L powder*. *Materials Science and Engineering: A*, 2013. **584**: p. 21-31.
38. Kempen, K., F. Welkenhuyzen, J. Qian, and J.-P. Kruth. *Dimensional accuracy of internal channels in SLM produced parts*. in *2014 ASPE Spring Topical Meeting: Dimensional Accuracy and Surface Finish in Additive Manufacturing, Berkeley, CA, Apr. 2014*.
39. Körner, C., E. Attar, and P. Heintz, *Mesoscopic simulation of selective beam melting processes*. *Journal of Materials Processing Technology*, 2011. **211**(6): p. 978-987.
40. Kruth, J.-P., G. Levy, F. Klocke, and T. Childs, *Consolidation phenomena in laser and powder-bed based layered manufacturing*. *CIRP annals*, 2007. **56**(2): p. 730-759.
41. Li, R., J. Liu, Y. Shi, L. Wang, and W. Jiang, *Balling behavior of stainless steel and nickel powder during selective laser melting process*. *The International Journal of Advanced Manufacturing Technology*, 2012. **59**(9-12): p. 1025-1035.
42. Boley, C., S.A. Khairallah, and A.M. Rubenchik, *Calculation of laser absorption by metal powders in additive manufacturing*. *Applied optics*, 2015. **54**(9): p. 2477-2482.
43. Strano, G., L. Hao, R.M. Everson, and K.E. Evans, *Surface roughness analysis, modelling and prediction in selective laser melting*. *Journal of Materials Processing Technology*, 2013. **213**(4): p. 589-597.
44. Li, P., D. Warner, A. Fatemi, and N. Phan, *Critical assessment of the fatigue performance of additively manufactured Ti–6Al–4V and perspective for future research*. *International Journal of Fatigue*, 2016. **85**: p. 130-143.
45. Resch, M., A.F. Kaplan, and D. Schuoecker. *Laser-assisted generating of three-dimensional parts by the blown powder process*. in *XIII International Symposium on Gas Flow and Chemical Lasers and High-Power Laser Conference*. 2001. SPIE.
46. Charles, A., A. Elkaseer, T. Müller, L. Thijs, M. Torge, V. Hagemeyer, and S. Scholz. *A Study of the Factors Influencing Generated Surface Roughness of Downfacing Surfaces in Selective Laser Melting*. in *Proceedings of the World Congress on Micro and Nano Manufacturing (WCMNM), Portorož, Slovenia*. 2018.
47. de Formanoir, C., S. Michotte, O. Rigo, L. Germain, and S. Godet, *Electron beam melted Ti–6Al–4V: Microstructure, texture and mechanical behavior of the as-built and heat-treated material*. *Materials Science and Engineering: A*, 2016. **652**: p. 105-119.
48. Shapiro, A.A., J. Borgonia, Q. Chen, R. Dillon, B. McEnerney, R. Polit-Casillas, and L. Soloway, *Additive manufacturing for aerospace flight applications*. *Journal of Spacecraft and Rockets*, 2016: p. 952-959.

49. Shaikh, J., N.K. Jain, and V. Venkatesh, *Precision finishing of bevel gears by electrochemical honing*. *Materials and manufacturing processes*, 2013. **28**(10): p. 1117-1123.
50. Gusarov, A. and E. Kovalev, *Model of thermal conductivity in powder beds*. *Physical Review B*, 2009. **80**(2): p. 024202.
51. Rombouts, M., L. Froyen, A. Gusarov, E.H. Bentefour, and C. Glorieux, *Photopyroelectric measurement of thermal conductivity of metallic powders*. *Journal of applied physics*, 2005. **97**(2).
52. Kruth, J.-P., P. Mercelis, J. Van Vaerenbergh, and T. Craeghs. *Feedback control of selective laser melting*. in *Proceedings of the 3rd international conference on advanced research in virtual and rapid prototyping*. 2007. Taylor & Francis Ltd.
53. Wang, D., Y. Yang, Z. Yi, and X. Su, *Research on the fabricating quality optimization of the overhanging surface in SLM process*. *The International Journal of Advanced Manufacturing Technology*, 2013. **65**: p. 1471-1484.
54. Ilin, A., R. Logvinov, A. Kulikov, A. Prihodovsky, H. Xu, V. Ploshikhin, B. Günther, and F. Bechmann, *Computer aided optimisation of the thermal management during laser beam melting process*. *Physics Procedia*, 2014. **56**: p. 390-399.
55. Mertens, R., S. Clijsters, K. Kempen, and J.-P. Kruth, *Optimization of scan strategies in selective laser melting of aluminum parts with downfacing areas*. *Journal of Manufacturing Science and Engineering*, 2014. **136**(6): p. 061012.
56. Sames, W.J., F. List, S. Pannala, R.R. Dehoff, and S.S. Babu, *The metallurgy and processing science of metal additive manufacturing*. *International Materials Reviews*, 2016. **61**(5): p. 315-360.
57. Xu, W., M. Brandt, S. Sun, J. Elambasseril, Q. Liu, K. Latham, K. Xia, and M. Qian, *Additive manufacturing of strong and ductile Ti-6Al-4V by selective laser melting via in situ martensite decomposition*. *Acta Materialia*, 2015. **85**: p. 74-84.
58. Zhao, X., S. Li, M. Zhang, Y. Liu, T.B. Sercombe, S. Wang, Y. Hao, R. Yang, and L.E. Murr, *Comparison of the microstructures and mechanical properties of Ti-6Al-4V fabricated by selective laser melting and electron beam melting*. *Materials & Design*, 2016. **95**: p. 21-31.
59. Xu, W., E. Lui, A. Pateras, M. Qian, and M. Brandt, *In situ tailoring microstructure in additively manufactured Ti-6Al-4V for superior mechanical performance*. *Acta Materialia*, 2017. **125**: p. 390-400.
60. Rafi, H., N. Karthik, H. Gong, T.L. Starr, and B.E. Stucker, *Microstructures and mechanical properties of Ti6Al4V parts fabricated by selective laser melting and electron beam melting*. *Journal of materials engineering and performance*, 2013. **22**(12): p. 3872-3883.
61. Qiu, C., N.J. Adkins, and M.M. Attallah, *Microstructure and tensile properties of selectively laser-melted and of HIPed laser-melted Ti-6Al-4V*. *Materials Science and Engineering: A*, 2013. **578**: p. 230-239.
62. Gong, H., K. Rafi, H. Gu, G.J. Ram, T. Starr, and B. Stucker, *Influence of defects on mechanical properties of Ti-6Al-4 V components produced by selective laser melting and electron beam melting*. *Materials & Design*, 2015. **86**: p. 545-554.

63. Ajdari, A., H. Nayeb-Hashemi, and A. Vaziri, *Dynamic crushing and energy absorption of regular, irregular and functionally graded cellular structures*. International Journal of Solids and Structures, 2011. **48**(3-4): p. 506-516.
64. Ashby, M., *The properties of foams and lattices*. Philosophical Transactions of the Royal Society A: Mathematical, Physical and Engineering Sciences, 2005. **364**(1838): p. 15-30.
65. Banhart, J., *Light-Metal Foams—History of Innovation and Technological Challenges*. Advanced Engineering Materials, 2013. **15**(3): p. 82-111.
66. Deshpande, V., M. Ashby, and N. Fleck, *Foam topology: bending versus stretching dominated architectures*. Acta materialia, 2001. **49**(6): p. 1035-1040.
67. Gibson, L.J. and M.F. Ashby, *Cellular solids: structure and properties*. 1999: Cambridge university press.
68. Kaur, M., T.G. Yun, S.M. Han, E.L. Thomas, and W.S. Kim, *3D printed stretching-dominated micro-trusses*. Materials & Design, 2017. **134**: p. 272-280.
69. Pham, M.-S., C. Liu, I. Todd, and J. Lertthanasarn, *Damage-tolerant architected materials inspired by crystal microstructure*. Nature, 2019. **565**(7739): p. 305-311.
70. Ashby, M., A. Evans, N. Fleck, L. Gibson, J. Hutchinson, H. Wadley, and F. Delale, *Metal foams: a design guide*. Applied Mechanics Reviews, 2001. **54**: p. B105.
71. Parthasarathy, J., B. Starly, and S. Raman, *A design for the additive manufacture of functionally graded porous structures with tailored mechanical properties for biomedical applications*. Journal of Manufacturing Processes, 2011. **13**(2): p. 160-170.
72. Horn, T.J., O.L. Harrysson, D.J. Marcellin-Little, H.A. West, B.D.X. Lascelles, and R. Aman, *Flexural properties of Ti6Al4V rhombic dodecahedron open cellular structures fabricated with electron beam melting*. Additive Manufacturing, 2014. **1**: p. 2-11.
73. Bonatti, C. and D. Mohr, *Large deformation response of additively-manufactured FCC metamaterials: From octet truss lattices towards continuous shell mesostructures*. International Journal of Plasticity, 2017. **92**: p. 122-147.
74. Jamshidinia, M., L. Wang, W. Tong, and R. Kovacevic, *The bio-compatible dental implant designed by using non-stochastic porosity produced by Electron Beam Melting®(EBM)*. Journal of Materials Processing Technology, 2014. **214**(8): p. 1728-1739.
75. Sallica-Leva, E., A. Jardini, and J. Fogagnolo, *Microstructure and mechanical behavior of porous Ti-6Al-4V parts obtained by selective laser melting*. Journal of the mechanical behavior of biomedical materials, 2013. **26**: p. 98-108.
76. Rashid, R.R., J. Mallavarapu, S. Palanisamy, and S. Masood, *A comparative study of flexural properties of additively manufactured aluminium lattice structures*. Materials Today: Proceedings, 2017. **4**(8): p. 8597-8604.
77. Koizumi, Y., A. Okazaki, A. Chiba, T. Kato, and A. Takezawa, *Cellular lattices of biomedical Co-Cr-Mo-alloy fabricated by electron beam melting with the aid of shape optimization*. Additive Manufacturing, 2016. **12**: p. 305-313.
78. Li, K., X.-L. Gao, and J. Wang, *Dynamic crushing behavior of honeycomb structures with irregular cell shapes and non-uniform cell wall thickness*. International Journal of Solids and Structures, 2007. **44**(14-15): p. 5003-5026.

79. Ozdemir, Z., A. Tyas, R. Goodall, and H. Askes, *Energy absorption in lattice structures in dynamics: Nonlinear FE simulations*. International Journal of Impact Engineering, 2017. **102**: p. 1-15.
80. Ozdemir, Z., E. Hernandez-Nava, A. Tyas, J.A. Warren, S.D. Fay, R. Goodall, I. Todd, and H. Askes, *Energy absorption in lattice structures in dynamics: Experiments*. International Journal of Impact Engineering, 2016. **89**: p. 49-61.
81. Raabe, D., *Cellular automata in materials science with particular reference to recrystallization simulation*. Annual review of materials research, 2002. **32**(1): p. 53-76.
82. Tan, W., N.S. Bailey, and Y.C. Shin, *A novel integrated model combining cellular automata and phase field methods for microstructure evolution during solidification of multi-component and multi-phase alloys*. Computational Materials Science, 2011. **50**(9): p. 2573-2585.
83. Desbiolles, J.-L., J.-J. Droux, J. Rappaz, and M. Rappaz, *Simulation of solidification of alloys by the finite element method*. Computer Physics Reports, 1987. **6**(1-6): p. 371-383.
84. McCartney, D. and V. Wills, *A finite element model of alloy solidification incorporating velocity-dependent growth temperatures*. Applied mathematical modelling, 1988. **12**(4): p. 354-361.
85. Kremeyer, K., *Cellular automata investigations of binary solidification*. Journal of Computational Physics, 1998. **142**(1): p. 243-263.
86. Zhang, L. and C.-B. Zhang, *Two-dimensional cellular automaton model for simulating structural evolution of binary alloys during solidification*. Transactions of nonferrous metals society of China, 2006. **16**(6): p. 1410-1416.
87. Zhan, X., Y. Wei, and Z. Dong, *Cellular automaton simulation of grain growth with different orientation angles during solidification process*. Journal of Materials Processing Technology, 2008. **208**(1-3): p. 1-8.
88. Tsai, D.-C. and W.-S. Hwang, *Numerical simulation of solidification morphologies of Cu-0.6 Cr casting alloy using modified cellular automaton model*. Transactions of Nonferrous Metals Society of China, 2010. **20**(6): p. 1072-1077.
89. Boettinger, W.J., J.A. Warren, C. Beckermann, and A. Karma, *Phase-field simulation of solidification*. Annual review of materials research, 2002. **32**(1): p. 163-194.
90. Chen, L.-Q., *Phase-field models for microstructure evolution*. Annual review of materials research, 2002. **32**(1): p. 113-140.
91. Fallah, V., M. Amoozraei, N. Provatas, S. Corbin, and A. Khajepour, *Phase-field simulation of solidification morphology in laser powder deposition of Ti-Nb alloys*. Acta Materialia, 2012. **60**(4): p. 1633-1646.
92. Das, A. and Z. Fan, *A Monte Carlo simulation of solidification structure formation under melt shearing*. Materials Science and Engineering: A, 2004. **365**(1-2): p. 330-335.
93. Plapp, M. and A. Karma, *Multiscale finite-difference-diffusion-Monte-Carlo method for simulating dendritic solidification*. Journal of Computational Physics, 2000. **165**(2): p. 592-619.

94. Koseki, T., H. Inoue, Y. Fukuda, and A. Nogami, *Numerical simulation of equiaxed grain formation in weld solidification*. Science and Technology of Advanced Materials, 2003. **4**(2): p. 183-195.
95. Szpunar, B. and R.W. Smith, *Monte Carlo simulation of solidification processes; porosity*. Canadian metallurgical quarterly, 1996. **35**(3): p. 299-303.
96. Semma, E., M. El Ganaoui, R. Bennacer, and A. Mohamad, *Investigation of flows in solidification by using the lattice Boltzmann method*. International Journal of Thermal Sciences, 2008. **47**(3): p. 201-208.
97. Gandin, C.-A. and M. Rappaz, *A 3D cellular automaton algorithm for the prediction of dendritic grain growth*. Acta Materialia, 1997. **45**(5): p. 2187-2195.
98. Yin, H., S. Felicelli, and L. Wang, *Simulation of a dendritic microstructure with the lattice Boltzmann and cellular automaton methods*. Acta Materialia, 2011. **59**(8): p. 3124-3136.
99. Zaeem, M.A., H. Yin, and S.D. Felicelli, *Modeling dendritic solidification of Al-3% Cu using cellular automaton and phase-field methods*. Applied Mathematical Modelling, 2013. **37**(5): p. 3495-3503.
100. Zaeem, M.A., H. Yin, and S.D. Felicelli, *Comparison of cellular automaton and phase field models to simulate dendrite growth in hexagonal crystals*. Journal of Materials Science & Technology, 2012. **28**(2): p. 137-146.
101. Eshraghi, M., S.D. Felicelli, and B. Jelinek, *Three dimensional simulation of solutal dendrite growth using lattice Boltzmann and cellular automaton methods*. Journal of Crystal Growth, 2012. **354**(1): p. 129-134.
102. Sun, D., M. Zhu, S. Pan, C. Yang, and D. Raabe, *Lattice Boltzmann modeling of dendritic growth in forced and natural convection*. Computers & Mathematics with Applications, 2011. **61**(12): p. 3585-3592.
103. Jelinek, B., M. Eshraghi, S. Felicelli, and J.F. Peters, *Large-scale parallel lattice Boltzmann-cellular automaton model of two-dimensional dendritic growth*. Computer Physics Communications, 2014. **185**(3): p. 939-947.
104. Shiomi, M., A. Yoshidome, F. Abe, and K. Osakada, *Finite element analysis of melting and solidifying processes in laser rapid prototyping of metallic powders*. International Journal of Machine Tools and Manufacture, 1999. **39**(2): p. 237-252.
105. Matsumoto, M., M. Shiomi, K. Osakada, and F. Abe, *Finite element analysis of single layer forming on metallic powder bed in rapid prototyping by selective laser processing*. International Journal of Machine Tools and Manufacture, 2002. **42**(1): p. 61-67.
106. Guo-feng, Y. and C. Guang-nan, *Numerical simulation of transient thermal field in laser melting process*. Applied Mathematics and Mechanics, 2004. **25**: p. 945-950.
107. Gusarov, A. and I. Smurov, *Two-dimensional numerical modelling of radiation transfer in powder beds at selective laser melting*. Applied Surface Science, 2009. **255**(10): p. 5595-5599.
108. Gusarov, A., I. Yadroitsev, P. Bertrand, and I. Smurov, *Heat transfer modelling and stability analysis of selective laser melting*. Applied Surface Science, 2007. **254**(4): p. 975-979.
109. Song, B., S. Dong, H. Liao, and C. Coddet, *Process parameter selection for selective laser melting of Ti6Al4V based on temperature distribution simulation and*

- experimental sintering*. The international journal of advanced manufacturing technology, 2012. **61**: p. 967-974.
110. Safdar, S., A.J. Pinkerton, R. Moat, L. Li, M.A. Sheikh, M. Preuss, and P.J. Withers. *An anisotropic enhanced thermal conductivity approach for modelling laser melt pools*. in *International Congress on Applications of Lasers & Electro-Optics*. 2007. Laser Institute of America.
 111. Roberts, I.A., C. Wang, R. Esterlein, M. Stanford, and D. Mynors, *A three-dimensional finite element analysis of the temperature field during laser melting of metal powders in additive layer manufacturing*. International Journal of Machine Tools and Manufacture, 2009. **49**(12-13): p. 916-923.
 112. Foroozmehr, A., M. Badrossamay, E. Foroozmehr, and S.i. Golabi, *Finite element simulation of selective laser melting process considering optical penetration depth of laser in powder bed*. Materials & Design, 2016. **89**: p. 255-263.
 113. Loh, L.-E., C.-K. Chua, W.-Y. Yeong, J. Song, M. Mapar, S.-L. Sing, Z.-H. Liu, and D.-Q. Zhang, *Numerical investigation and an effective modelling on the Selective Laser Melting (SLM) process with aluminium alloy 6061*. International Journal of Heat and Mass Transfer, 2015. **80**: p. 288-300.
 114. Rao, S.S., *The finite element method in engineering*. 2017: Butterworth-heinemann.
 115. Janssens, K.G.F., D. Raabe, E. Kozeschnik, M.A. Miodownik, and B. Nestler, *Computational materials engineering: an introduction to microstructure evolution*. 2010: Academic Press.
 116. Gaillard, C., J. Despois, and A. Mortensen, *Processing of NaCl powders of controlled size and shape for the microstructural tailoring of aluminium foams*. Materials Science and Engineering: A, 2004. **374**(1-2): p. 250-262.
 117. Petry, W., A. Heiming, J. Trampenau, M. Alba, C. Herzig, H. Schober, and G. Vogl, *Phonon dispersion of the bcc phase of group-IV metals. I. bcc titanium*. Physical Review B, 1991. **43**(13): p. 10933.
 118. Brandes, E.A. and G. Brook, *Smithells metals reference book*. 2013: Elsevier.
 119. Simonelli, M., Y.Y. Tse, and C. Tuck. *Further Understanding on Ti-6Al-4V Selective Laser Melting Using Texture Analysis*. in *2012 International Solid Freeform Fabrication Symposium*. 2012. University of Texas at Austin.
 120. Antonysamy, A.A., J. Meyer, and P. Prangnell, *Effect of build geometry on the β -grain structure and texture in additive manufacture of Ti6Al4V by selective electron beam melting*. Materials characterization, 2013. **84**: p. 153-168.
 121. Facchini, L., E. Magalini, P. Robotti, A. Molinari, S. Höges, and K. Wissenbach, *Ductility of a Ti-6Al-4V alloy produced by selective laser melting of prealloyed powders*. Rapid Prototyping Journal, 2010.
 122. Sercombe, T., N. Jones, R. Day, and A. Kop, *Heat treatment of Ti-6Al-7Nb components produced by selective laser melting*. Rapid Prototyping Journal, 2008.
 123. Galarraga, H., D.A. Lados, R.R. Dehoff, M.M. Kirka, and P. Nandwana, *Effects of the microstructure and porosity on properties of Ti-6Al-4V ELI alloy fabricated by electron beam melting (EBM)*. Additive Manufacturing, 2016. **10**: p. 47-57.
 124. Kobryn, P., E. Moore, and S.L. Semiatin, *The effect of laser power and traverse speed on microstructure, porosity, and build height in laser-deposited Ti-6Al-4V*. Scripta Materialia, 2000. **43**(4): p. 299-305.

125. Vrancken, B., L. Thijs, J.-P. Kruth, and J. Van Humbeeck, *Heat treatment of Ti6Al4V produced by Selective Laser Melting: Microstructure and mechanical properties*. Journal of Alloys and Compounds, 2012. **541**: p. 177-185.
126. Liu, F., D.Z. Zhang, P. Zhang, M. Zhao, and S. Jafar, *Mechanical properties of optimized diamond lattice structure for bone scaffolds fabricated via selective laser melting*. Materials, 2018. **11**(3): p. 374.
127. Choy, S.Y., C.-N. Sun, K.F. Leong, and J. Wei, *Compressive properties of Ti-6Al-4V lattice structures fabricated by selective laser melting: Design, orientation and density*. Additive Manufacturing, 2017. **16**: p. 213-224.
128. Cansizoglu, O., O. Harrysson, D. Cormier, H. West, and T. Mahale, *Properties of Ti-6Al-4V non-stochastic lattice structures fabricated via electron beam melting*. Materials Science and Engineering: A, 2008. **492**(1-2): p. 468-474.
129. Merkt, S., C. Hinke, J. Bültmann, M. Brandt, and Y. Xie, *Mechanical response of TiAl6V4 lattice structures manufactured by selective laser melting in quasistatic and dynamic compression tests*. Journal of laser applications, 2015. **27**(S1): p. S17006.
130. Heintl, P., L. Müller, C. Körner, R.F. Singer, and F.A. Müller, *Cellular Ti-6Al-4V structures with interconnected macro porosity for bone implants fabricated by selective electron beam melting*. Acta biomaterialia, 2008. **4**(5): p. 1536-1544.
131. Ahmadi, S.M., S. Amin Yavari, R. Wauthle, B. Pouran, J. Schrooten, H. Weinans, and A.A. Zadpoor, *Additively manufactured open-cell porous biomaterials made from six different space-filling unit cells: The mechanical and morphological properties*. Materials, 2015. **8**(4): p. 1871-1896.
132. Wauthle, R., B. Vrancken, B. Beynaerts, K. Jorissen, J. Schrooten, J.-P. Kruth, and J. Van Humbeeck, *Effects of build orientation and heat treatment on the microstructure and mechanical properties of selective laser melted Ti6Al4V lattice structures*. Additive Manufacturing, 2015. **5**: p. 77-84.
133. Ashby, M.F., *The properties of foams and lattices*. Philosophical Transactions of the Royal Society A: Mathematical, Physical and Engineering Sciences, 2006. **364**(1838): p. 15-30.